The Pennsylvania State University

The Graduate School

Department of Electrical Engineering

BROADBAND SUPERCONTINUUM GENERATION IN SAPPHIRE FIBERS AND APPLICATIONS

A Dissertation in

Electrical Engineering

by

Jae Hun Kim

Submitted in Partial Fulfillment

of the Requirements

for the Degree of

Doctor of Philosophy

December 2008

The dissertation of Jae Hun Kim was reviewed and approved* by the following:

Stuart (Shizhuo) Yin
Professor of Electrical Engineering
Dissertation Advisor
Chair of Committee

Zhiwen Liu
Associate Professor of Electrical Engineering

James Breakall
Professor of Electrical Engineering

Zi-Kui Liu
Professor of Materials Science and Engineering

W. Kenneth Jenkins
Professor of Electrical Engineering
Head of the Department of Electrical Engineering

*Signatures are on file in the Graduate School

ABSTRACT

In this dissertation, supercontinuum generations in sapphire fibers under various conditions are investigated, and their corresponding effects are analyzed. Main motivation to use sapphire fibers as optical media for supercontinuum generation is that they have characteristics of good transparency in mid-IR, high laser damage threshold, and high melting temperature compared to conventionally utilized fibers including silica-based fibers and infrared fibers. As an introductory step, the general theories of supercontinuum generation including derivation of Schrödinger equation and explanation of various nonlinear effects are covered. Also, laser systems including a femtosecond laser system and an optical parametric amplifier in our lab are explained since they are key equipments for most experiments performed in this dissertation. Sapphire fibers are pumped at various wavelengths to verify their ability to generate supercontinuum in wide wavelength regions since they are known to be transparent from visible to 4~5μm. Since nonlinearity, dispersion, and fiber length play important roles on nonlinear interactions in sapphire fibers, corresponding nonlinear effects are also investigated and explained. The core diameter of sapphire fibers we used for experiments is quite large that its nonlinear coefficient inversely proportional to mode area is quite small even though its nonlinear refractive index is comparable to silica fiber. To overcome small nonlinear coefficient due to large mode area, sapphire fibers are pumped by three pumping sources to have very wide spectrum ranged from UV to mid-IR region, which can be predicted by the superposition of three different spectra. As application purposes, experiments of IR spectroscopy and remote sensing are performed. Finally, several future works to solidify this dissertation are discussed.

TABLE OF CONTENTS

LIST OF FIGURES

LIST OF TABLES

ACKNOWLEDGEMENTS

First of all, I would like to express my sincere appreciation to my advisor, Dr. Stuart (Shizhuo) Yin, for his enormous advices and consideration on not only researches, but also many life circumstances I have confronted. I would also like to thank to Professor Zhiwen Liu for many advices on simulations, researches and being my dissertation committee. I would also like to show my gratitude to Professor James Breakall and Professor Zi-Kui Liu for valuable advices and suggestions as members of my dissertation committee. I would also like to thank Dr. Karl Reichard for his research advices even though he could not attend my defense presentation due to schedule conflict.

I would like to thank Meng-Ku for his help on our femtosecond laser systems and sharing many problems we tried to solve until late night. I would also like to show my gratitude to Dr. Kebin Shi for his help on simulations. I am very thankful to Jon, Nam, Chia-En, Fei, Chun, Dr. An, Dr. Zhu, Peng Li, Jimmy, Dr. Zheng, and Dr. Dong for their assistances in many experiments. I would like to thank Dr. D. H. Woo, Dr. S. Lee, Dr. S. H. Kim, Dr. Y. T. Byun, Dr. Y. M. Jhon, and other colleagues from KIST for their support.

I would like to give most appreciation to my beloved wife Hyun Kyung, son Dohyun and my newborn daughter Gyuri for being with me, sharing happiness and sadness together. Without you, I wouldn’t be able to make this far. I would also like to thank my father and my parents-in-law for their support and sacrifice. I am grateful to my brother’s family and my brother-in-law’s family for their support.

Finally, I dedicate this dissertation to my mother in memory of her infinite love and sacrifice.

Partial financial support of this work by ONR grant, N00014-05-1-0844 is greatly appreciated.

Chapter 1

Introduction

It is well known that supercontinuum generation (SCG) refers to the extreme broadening of an optical spectrum as a result of nonlinear interactions between laser pulses and the optical medium in which they are traveling. The SCG was first realized in liquids with large optical Kerr constants [1]. Later, the SCG phenomenon was also observed in standard silica optical fibers [2]. Although the nonlinear coefficient of the optical fiber is much lower than that of the Kerr liquids used in [1], this deficiency is largely overcome by taking advantage of the fiber's unique structure (i.e., (1) the light is confined within the small area of the fiber core, and (2) the fiber has a long interaction length). More recently, highly nonlinear structures including optical fibers [3-14] and high peak power compact femtosecond lasers [15-19] have made ultra-broadband supercontinuum (broadened by more than 1000 nm) sources feasible. These new supercontinuum sources can be very useful for a variety of applications, including optical coherence tomography [20, 21], optical metrology [22, 23], medical imaging [15], terahertz generation [24-26], and telecommunications [27-29].

Recently, the interest in broadband mid-IR light sources has greatly increased due to the critical need by a variety of applications such as IR spectroscopy [30], remote sensing and combustion monitoring [31, 32]. Conventional sources such as optical parametric amplifiers (OPOs), tunable solid-state lasers, Fourier transform infrared (FTIR) spectroscopic instruments, and quantum cascaded lasers (QCLs) are currently utilized for these applications [33]. However, wavelengths of these sources need to be continuously tuned to cover the entire spectral range needed. Compared to these

conventional sources, supercontinuum source has the advantage of covering a wide range of spectrum without the time delay caused by the wavelength tuning of conventional sources.

Even though some papers have shown SCG in silica-based fibers that extend into mid-IR region, SCG in silica materials are typically limited by heavy material absorption in the mid-IR region [32]. To realize SCG in the mid-IR region, IR glass fibers are commonly employed [31, 34-36]. Although mid-IR SCG have been successfully generated in these IR glass fibers, it is difficult to achieve very high power supercontinuum sources because of the lower softening temperature of these IR glass fibers [e.g., around 455 ^{o}C for ZBLAN Fluoride fiber [37], 600 ^{o}C to 900 ^{o}C for Chalcogenide fiber [36], and 538 ^{o}C for SF-6 fiber [38], which are lower than that of silica fibers (~ 1175 ^{o}C) [39]].

To overcome the limitations of conventional silica-based fibers with high absorption in mid-IR and IR glass fibers with low softening temperature, in this dissertation, single crystal sapphire fibers are utilized to realize SCG. Single crystal sapphire fiber has intrinsic advantages over their glass counterparts because of the following reasons:

- High transparency in the mid-IR. Single crystal sapphire fiber is highly transparent in the mid-IR region (up to 5 microns) [40].
- High melting temperature. Single crystal sapphire fiber has very high melting temperature (>2,000 ^{o}C for Sapphire) [40].

- High damage threshold. Single crystal sapphire fiber exhibits very high damage threshold around 1.3kJ/cm^2, which is about 500 times higher than a silica fiber (2.5J/cm^2) [41].
- Good nonlinearity. The nonlinearity of single crystal sapphire fibers is comparable to the nonlinearity of a silica-based fiber (e.g., the nonlinear refractive index coefficient of sapphire is $n_2 \approx 3x10^{-20} m^2/W$) [42].

Based on many advantages shown above, single crystal sapphire fiber can be considered as a good candidate for the generation of high-power and broadband supercontinuum source.

Sapphire fibers have been vividly used for various applications such as medical laser power delivery [43], high-temperature thermometers [44], and harsh environment sensors [45-48] due to their high melting temperature, high damage threshold, and good transmission in wide wavelength range including mid-IR region. However, it has not been very long since sapphire material has been considered as an optical medium to generate supercontinuum. Even though single crystal sapphire fiber satisfies many conditions as an optical medium to generate supercontinuum (good transparency in wide wavelength region, similar nonlinearity compared to a silica-based fiber, high damage threshold, and high melting temperature), only several papers report supercontinuum generation in the form of sapphire bulks, not sapphire fibers [49, 50]. To the best of our knowledge, we are the first group to demonstrate supercontinuum generation in sapphire fibers [51-53]. We assume that reasons for this late discovery are as follows:

- Availability of powerful laser source: Most single crystal sapphire fibers have large core diameters of more than 60μm. To generate supercontinuum in large mode area,

high peak-power pulse laser sources such as femtosecond pulse lasers are required. However, it has not been very long since ultrafast laser systems were available to user level, not just laser research level [17, 54].

- Availability of sapphire fiber: Sapphire fibers were developed by several universities including Stanford University, University of South Florida, and Rutgers University at research level [41, 55-59]. However, the first commercial sapphire fibers has not been produced until late 1990's (Saphikon, Inc. [60]). Also, based on the best of our knowledge, only couple companies (Photran, LLC and MicroMaterials, Inc.) sell commercial sapphire fibers.
- Different application areas: As told before, sapphire fibers are mostly used for specific applications such as medical laser power delivery [43], high-temperature thermometers [44], and harsh environment sensors [45-48]. These specific research areas are deviated from nonlinear optics area. Therefore, researchers in nonlinear optics area may not know about the availability of sapphire fibers. However, our lab is currently working on both harsh environment sensors and supercontinuum generation using optical fibers. Therefore, we successfully discovered that sapphire fibers could be perfect optical media to generate high power and mid-IR supercontinuum since they have high damage threshold, high melting temperature, similar nonlinearity to silica fiber, and good transmission in wide wavelength range.

To explain various effects caused inside single crystal sapphire fiber, this dissertation is composed of 9 chapters.

Chapter 2 in this dissertation is to establish thorough backgrounds in nonlinear fiber optics, which describes pulse propagation in optical fibers. Theoretical derivations

of pulse propagation in optical fibers from Maxwell to Schrödinger equations are performed based on [20]. Since most SCG experiments are performed using a high-intensity and short-width pulse laser, generalized Schrödinger equation including high-order nonlinear effect is derived. To understand various interactions caused by pulse propagation in an optical fiber, the nonlinear effects including self phase modulation (SPM), four wave mixing (FWM), cross phase modulation (XPM), and stimulated Raman scattering (SRS) are individually investigated. Our own simulation and experimental results are included to explain these nonlinear effects.

Chapter 3 describes femtosecond laser systems, which are fundamental equipments for most experiments performed in this dissertation. Even though many ultrafast lasers are now commercially available in single compact packaging with easily operational on-off switches, those single-packaged lasers are unable to provide very high-peak-power pulses, which are required to generate high power and broadband supercontinuum. To fulfill high-intensity requirements, the weak pulses need to be amplified. Our femtosecond laser system employs chirped-pulse amplification technique to amplify weak pulses generated from our seed laser [16, 54]. Also, to extend supercontinuum into mid-IR region, we utilize an optical parametric amplifer (OPA), which is based on differential frequency generation (DFG), the most common way to realize the wavelength shift into mid- and far-IR regions.

Chapter 4 describes the basic characteristics of single crystal sapphire fiber, and investigates its feasibility as possible optical medium to generate high-power and broadband supercontinuum source. Single crystal sapphire fiber is pumped at the wavelength of 784nm to demonstrate that it is indeed an optical medium to offer high-

intensity and broadband supercontinuum source. Also, various researches including comparison between sapphire fibers and bulk material, and spectra dependence according to fiber lengths are performed in this chapter.

Chapter 5 investigates supercontinuum generation in mid-IR region using single crystal sapphire fibers by pumping at the wavelength of 2μm. Since pumping wavelength longer than 1.3μm (zero dispersion) belongs to anomalous dispersion region, two different nonlinear effects, which are SPM and soliton-related dynamics accompanied by SPM caused by fiber lengths longer and shorter than dispersion length, are also researched. 5cm single crystal sapphire fiber is pumped at 2.5μm to generate a spectra ranged from 2μm to 3.2μm, whose upper range cannot be achieved by silica-based fibers.

Chapter 6 introduces a way to further broaden supercontinuum spectra by employing the scheme of multiple pumping sources. The core diameter of sapphire fibers we used for experiments is quite large that nonlinear coefficient inversely proportional to mode area is quite small. To overcome small nonlinear coefficient due to large mode area, sapphire fibers are pumped by multiple pumping sources to have very wide spectrum ranged from UV to mid-IR region, which can be predicted by the superposition of three different spectra.

Previously, many numerical simulations to investigate supercontinua in various fibers (mostly silica-based fibers) have been performed. However, no numerical investigation of supercontinuum effect in a sapphire fiber has been previously performed since we are the first and only group to research supercontinuum generation in sapphire fibers. In Chapters 5 and 6, we perform numerical simulations to help understanding the various nonlinear effects observed in sapphire fibers. We utilize the generalized nonlinear

schrödinger equation (NLSE) developed for silica fibers to simulate pulse propagation in sapphire fibers, and compare experimental and simulation results to investigate the conformity of theoretical model between silica and sapphire fibers.

Chapter 7 shows several application areas of supercontinuum generated by sapphire fibers. IR chemical spectroscopy and possible remote sensing using the supercontinuum source from sapphire fibers are performed in various IR regions.

Finally, Chapters 8 and 9 provide future works and conclusion.

Chapter 2

Supercontinuum Generation in Optical Fibers : Theory and Analysis

2.1 – Supercontinuum Generation : Derivation of Schrödinger Equation in General Cases

In this chapter, Schrödinger equation depicting pulse propagation in optical fibers can be derived. General procedures are mostly based on Agrawal's Nonlinear Fiber Optics [61].

Optical pulse propagation in optical fibers begins with Maxwell's equations:

$$\nabla \times E = -\frac{\partial B}{\partial t} \quad , \tag{2.1}$$

$$\nabla \times H = J + \frac{\partial D}{\partial t} = \frac{\partial D}{\partial t} \quad , \tag{2.2}$$

$$\nabla \cdot D = \rho_f = 0 \quad , \tag{2.3}$$

and $\nabla \cdot B = 0$, (2.4)

where E is electric field, H is magnetic field, current density J and charge density ρ_f are 0 for optical fibers, and D and B are electric and magnetic flux densities, which can be expressed as:

$$D = \varepsilon_0 E + P \quad , \tag{2.5}$$

and $B = \mu_0 H + M$, (2.6)

where ε_0 and μ_0 are vacuum permittivity and permeability, respectively, and P and M are induced electric and magnetic polarizations. Since optical fibers are nonmagnetic, M can be considered as 0. Therefore, the relationship between B and H can be expressed as:

$$B = \mu_0 H \quad . \tag{2.7}$$

Taking the curl for both sides of (2.1) leads to

$$\nabla \times (\nabla \times E) = -\mu_0 \varepsilon_0 \frac{\partial^2 E}{\partial t^2} - \frac{\partial^2 P}{\partial t^2} \quad . \tag{2.8}$$

The relationship between polarization *P* and Electric field *E* can be expressed as

$$P = \varepsilon_0 \left(\chi^{(1)} \cdot E + \chi^{(2)} \cdot EE + \chi^{(3)} \cdot EEE + \cdots \right) \quad , \tag{2.9}$$

where $\chi^{(i)} (i = 1,2,...)$ is the susceptibility. For simplicity, third order nonlinear effects are considered, the polarization *P* can be written as

$$P(r,t) = P_L(r,t) + P_{NL}(r,t) \quad , \tag{2.10}$$

where $P_L(r,t)$ and $P_{NL}(r,t)$ represent linear and nonlinear parts of *P*, respectively. Both linear and nonlinear parts of *P* can be denoted as:

$$P_L(r,t) = \varepsilon_0 \int_{-\infty}^{\infty} \chi^{(1)}(t-t') \cdot E(r,t') dt' \quad , \tag{2.11}$$

and

$$P_{NL}(r,t) = \varepsilon_0 \int\int\int_{-\infty}^{\infty} \chi^{(3)}(t-t_1, t-t_2, t-t_3) \vdots \times E(r,t_1) E(r,t_2) E(r,t_3) dt_1 dt_2 dt_3 . \tag{2.12}$$

With (2.3) and (2.5), the left side of (2.8) can be simplified as following:

$$\nabla \times (\nabla \times E) = \nabla(\nabla \cdot E) - \nabla^2 E = -\nabla^2 E \quad . \tag{2.13}$$

By applying (2.13) and (2.10) into (2.8), the equation including the linear and nonlinear parts of induced polarization can be expressed as

$$\nabla^2 E - \mu_0 \varepsilon_0 \frac{\partial^2 E}{\partial t^2} = \mu_0 \frac{\partial^2 P_L}{\partial t^2} + \mu_0 \frac{\partial^2 P_{NL}}{\partial t^2} \quad . \tag{2.14}$$

If the pulse is assumed to be a varying envelope, electric field and polarization components can be written as

$$E(r,t)=\frac{1}{2}\hat{x}\left[E(r,t)e^{-i\omega_0 t}+c.c.\right] \quad , \tag{2.15}$$

$$P_L(r,t)=\frac{1}{2}\hat{x}\left[P_L(r,t)e^{-i\omega_0 t}+c.c.\right] \quad , \tag{2.16}$$

and $P_{NL}(r,t)=\frac{1}{2}\hat{x}\left[P_{NL}(r,t)e^{-i\omega_0 t}+c.c.\right]$. (2.17)

The linear part of induced polarization can be modified according to (2.11) as

$$P_L(r,t)=\varepsilon_0\int_{-\infty}^{\infty}\chi_{xx}^{(1)}(t-t')\cdot E(r,t')e^{i\omega_0(t-t')}dt'$$

$$=\frac{\varepsilon_0}{2\pi}\int_{-\infty}^{\infty}\tilde{\chi}_{xx}^{(1)}(\omega)\cdot\tilde{E}(r,\omega-\omega_0)e^{-i(\omega-\omega_0)t}d\omega \quad , \tag{2.18}$$

where $\tilde{E}(r,\omega)$ is the Fourier transform of $E(r,t')$.

Also, the nonlinear part of induced polarization can be modified according to (2.12) as

$$P_{NL}(r,t)=\varepsilon_0\chi^{(3)}\vdots E(r,t)E(r,t)E(r,t)\approx\varepsilon_0\varepsilon_{NL}E(r,t) \quad , \tag{2.19}$$

where $\varepsilon_{NL}\approx\frac{3}{4}\chi_{xxxx}^{(3)}\left|E(r,t)\right|^2$ represents the nonlinear part of the dielectric constant. This assumption is valid when the nonlinear response is considered as instantaneous.

Even though (2.14) is a nonlinear process, ε_{NL} can be considered as a constant since the pulse is assumed to be a varying envelope. With proper substitution of (2.15) - (2.17) and (2.19) into (2.14), the Helmholtz equation as following needs to be satisfied in frequency domain:

$$\nabla^2\tilde{E}+\varepsilon(\omega)k_0^2\tilde{E}=0 \quad , \tag{2.20}$$

where $\varepsilon(\omega)=1+\chi_{xx}^{(1)}(\omega)+\varepsilon_{NL}$ and $k_0=\omega/c$.

The dielectric constant $\varepsilon(\omega)$ can be expressed in the terms of the refractive index $\tilde{n}$ and the absorption coefficient $\tilde{\alpha}$ as

$$\varepsilon(\omega)=\left(\tilde{n}+\frac{i\tilde{\alpha}}{2k_0}\right)^2 \quad , \tag{2.21}$$

where $\tilde{n}=n+n_2|E|^2$ and $\tilde{\alpha}=\alpha+\alpha_2|E|^2$.

The dielectric constant $\varepsilon(\omega)$ can further be approximated to

$$\varepsilon(\omega)=\left(n+n_2|E|^2+\frac{i\tilde{\alpha}}{2k_0}\right)^2\approx n^2+2n\left(n_2|E|^2+\frac{i\tilde{\alpha}}{2k_0}\right)\approx n^2+2n\Delta n \tag{2.22}$$

since $\Delta n=n_2|E|^2+\frac{i\tilde{\alpha}}{2k_0}$ can be considered as very small perturbation. By using the variable separation method, $\tilde{E}(r,\omega)$ can be expressed as

$$\tilde{E}(r,\omega-\omega_0)=F(x,y)\tilde{A}(z,\omega-\omega_0)e^{i\beta_0 z} \quad , \tag{2.23}$$

where $\tilde{A}(z,\omega)$ and β_0 are a slowly varying function of z and wave number, respectively. By substituting (2.23) into (2.14), functions $F(x,y)$ and $\tilde{A}(z,\omega)$ can be separated as follows:

$$\frac{\partial^2 F}{\partial x^2}+\frac{\partial^2 F}{\partial y^2}+\left[\varepsilon(\omega)k_0^2-\tilde{\beta}^2\right]F=0 \quad , \tag{2.24}$$

and $$\frac{\partial^2 \tilde{A}}{\partial z^2}+2i\beta_0\frac{\partial \tilde{A}}{\partial z}+\left(\tilde{\beta}^2-\beta_0^2\right)\tilde{A}=0 \quad , \tag{2.25}$$

where $\frac{\partial^2 \tilde{A}}{\partial z^2}$ in (Eqn. 2.25) can be removed since $\tilde{A}(z,\omega)$ is assumed to be a slowly varying function of z. By using first-order perturbation theory, (Eqn. 2.24) can be solved for $\tilde{\beta}$ as

$$\tilde{\beta}(\omega)=\beta(\omega)+\Delta\beta \quad , \tag{2.26}$$

where

$$\Delta\beta = \frac{k_0 \int\int_{-\infty}^{\infty} \Delta n \left|F(x,y)\right|^2 dxdy}{\int\int_{-\infty}^{\infty} \left|F(x,y)\right|^2 dxdy} \quad . \tag{2.27}$$

Also, by approximating that $\tilde{\beta}^2 - \beta_0^2 \approx 2\beta_0\left(\tilde{\beta} - \beta_0\right)$, (2.25) can be simplified as

$$\frac{\partial \tilde{A}}{\partial z} = i\left[\beta(\omega) + \Delta\beta - \beta_0\right]\tilde{A} \quad . \tag{2.28}$$

The wave number $\beta(\omega)$ can be expanded using Taylor series to be

$$\beta(\omega) = \beta_0 + (\omega - \omega_0)\beta_1 + \frac{1}{2}(\omega - \omega_0)^2\beta_2 + \frac{1}{6}(\omega - \omega_0)^3\beta_3 + \cdots \quad , \tag{2.29}$$

where ω_0 is the carrier frequency and $\beta_m = \left(\frac{d^m\beta}{d\varpi^m}\right)_{\omega=\omega_0}$. Since $\tilde{A}(z,\omega)$ is the Fourier transform of $A(z,t)$, and can be expressed as

$$A(z,t) = \frac{1}{2\pi}\int_{-\infty}^{\infty} \tilde{A}(z,\omega-\omega_0)e^{-i(\omega-\omega_0)t}d\omega, \tag{2.30}$$

(2.28) in time domain can be expressed by including (2.29) as

$$\frac{\partial A}{\partial z} = -\beta_1\frac{\partial A}{\partial t} - \frac{i\beta_2}{2}\frac{\partial^2 A}{\partial t^2} + i\Delta\beta A \quad . \tag{2.31}$$

Also, by using (2.22) and (2.27), (2.31) can be expressed as

$$\frac{\partial A}{\partial z} + \beta_1\frac{\partial A}{\partial t} + \frac{i\beta_2}{2}\frac{\partial^2 A}{\partial t^2} + \frac{\alpha}{2}A = +i\gamma\left|A\right|^2 A \quad , \tag{2.32}$$

where the γ is the nonlinear parameter, and can be denoted as

$$\gamma = \frac{n_2\omega_0}{cA_{eff}} = \frac{2\pi n_2}{\lambda A_{eff}} \quad , \tag{2.33}$$

in which, the effective core area is

$$A_{eff} = \frac{\left(\int\int_{-\infty}^{\infty} |F(x,y)|^2 \, dxdy \right)^2}{\int\int_{-\infty}^{\infty} |F(x,y)|^4 \, dxdy} \quad . \tag{2.34}$$

If a pulse is assumed to be Gaussian distributed, the effective core area is

$$A_{eff} = \pi w^2 \quad , \tag{2.35}$$

where w is the mode-width parameter.

2.2 - Ultra-short Pulse Propagation : Derivation of Schrödinger Equation in Highly Nonlinear Cases

The equation (2.32) for pulse propagation in optical fibers includes the most of nonlinear effects. However, when a pulse width goes beyond ps level (less than 1 ps), (2.32) needs to be modified since it is obtained through the assumption based on larger pulse width (larger than 1ps). When the pulse width of less than 1ps propagates in an optical fiber, nonlinear effects including Raman gain and cross phase modulation (XPM) are observed. Also, the energy of a pulse can be transformed to other pulses due to stimulated inelastic scattering processes such as stimulated Raman scattering (SRS) and stimulated Brillouin scattering (SBS). Since pulses interact for the pulse width less than 1ps, the assumption made for (2.19) can no longer be valid. If we assume that nonlinear effects such as third harmonic generation and four-wave mixing (FWM) are either nonexistent or very small, the relationship of the third order susceptibility can be explained as

$$\chi^{(3)}(t-t_1, t-t_2, t-t_3) = \chi^{(3)} R(t-t_1)\delta(t-t_2)\delta(t-t_3) \quad , \tag{2.36}$$

where $R(t)$ is the normalized nonlinear response function.

By substituting (2.36) into (2.12), the nonlinear polarization is

$$P_{NL}(r,t)=\varepsilon_0\chi^{(3)}E(r,t)\int_{-\infty}^{t}R(t-t_1)\left|E(r,t_1)\right|^2dt_1 \quad . \tag{2.37}$$

(2.14) can be modified according to (2.37) and (2.15)-(2.17) to have

$$\nabla^2\tilde{E}+n^2(\omega)k_0^2\tilde{E}=-ik_0\alpha$$

$$+\chi^{(3)}\frac{\omega^2}{c^2}\int\int_{-\infty}^{\infty}\tilde{R}(\omega-\omega_1)\tilde{E}(\omega_1,z)\tilde{E}(\omega_2,z)\tilde{E}^*(\omega_1+\omega_2-\omega,z)d\omega_1 d\omega_2 \ . \tag{2.38}$$

Therefore, this equation can be expressed in time domain as

$$\frac{\partial A}{\partial z}+\frac{\alpha}{2}A+\beta_1\frac{\partial A}{\partial t}+\frac{i\beta_2}{2}\frac{\partial^2 A}{\partial t^2}-\frac{\beta_3}{6}\frac{\partial^3 A}{\partial t^3}$$

$$=i\gamma\left(1+\frac{i}{\omega_0}\frac{\partial}{\partial t}\right)\left(A(z,t)\int_{-\infty}^{\infty}R(t')\left|A(z,t-t')\right|^2dt'\right) \quad , \tag{2.39}$$

where nonlinear response function $R(t)$ can be expressed as

$$R(t)=(1-f_R)\delta(t)+f_R h_R(t) \quad , \tag{2.40}$$

where f_R is the fractional contribution of the instantaneous Raman response to the nonlinear refractive index, and h_R is the delayed Raman response function. If the h_R has a damped oscillation response, it can be written as

$$h_R(t)=\frac{\tau_1^2+\tau_2^2}{\tau_1\tau_2^2}e^{-\frac{t}{\tau_2}}\sin\left(\frac{t}{\tau_1}\right) \quad . \tag{2.41}$$

Equation (2.39) depicts the complete Schrödinger equation, which covers all the nonlinear effects caused by any pulse propagation in optical fibers. If a pulse width is less than 1ps but larger than 10fs, we can use Taylor expansion as

$$\left|A(z,t-t')\right|^2=\left|A(z,t)\right|^2-t'\frac{\partial}{\partial t}\left|A(z,t)\right|^2 \tag{2.42}$$

to simplify (2.39).

The simplified equation for (2.39) can be written as

$$\frac{\partial A}{\partial z}+\frac{\alpha}{2}A+\frac{i\beta_2}{2}\frac{\partial^2 A}{\partial T^2}-\frac{\beta_3}{6}\frac{\partial^3 A}{\partial T^3}$$

$$=i\gamma\left(|A|^2A+\frac{i}{\omega_0}\frac{\partial}{\partial T}\left(|A|^2A\right)-T_RA\frac{\partial|A|^2}{\partial T}\right) \quad , \tag{2.43}$$

where T_R is defined as

$$T_R=\int_{-\infty}^{\infty}tR(t)dt=f_R\int_{-\infty}^{\infty}th_R(t)dt=f_R\frac{d\left(\mathrm{Im}\,\tilde{h}_R\right)}{d(\Delta\omega)}\bigg|_{\Delta\omega=0} \tag{2.44}$$

and the retarded frame T can be expressed as

$$T=t-\frac{z}{v_g}\equiv t-\beta_1 z \quad , \tag{2.45}$$

which is the frame for a pulse moving at the group velocity v_g.

Each term of the Schrödinger equation in (2.43) is responsible for individual effects as

$$\frac{\partial A}{\partial z}+\underbrace{\frac{\alpha}{2}A}_{①}+\underbrace{\frac{i\beta_2}{2}\frac{\partial^2 A}{\partial T^2}-\frac{\beta_3}{6}\frac{\partial^3 A}{\partial T^3}}_{②}$$

$$=i\gamma\left(\underbrace{|A|^2A}_{③}+\underbrace{\frac{i}{\omega_0}\frac{\partial}{\partial T}\left(|A|^2A\right)}_{④}-\underbrace{T_RA\frac{\partial|A|^2}{\partial T}}_{⑤}\right) \quad , \tag{2.46}$$

where ① is gain/loss, ② is group velocity dispersion, ③ is self-phase modulation, ④ is self-steepening, and ⑤ is delayed Raman response.

The theoretical model derived in this chapter is based on silica fibers. In Chapters 5 and 6, we utilize the theoretical model developed in this chapter to simulate pulse propagation in sapphire fibers, and compare the simulations with experimental results to

investigate the conformity of theoretical model between silica and sapphire fibers.

2.3 - Investigation of Various Effects Caused by Pulse Propagation in Optical Fibers

a. Self-Phase Modulation

When a pulse travels through an optical fiber, many nonlinear effects can be observed. One of the most dominant nonlinear effects is self phase modulation (SPM), which is a phase shift induced by a traveling pulse in an optical fiber.

The refractive index of an optical fiber can be explained as [62]

$$n(I) = n_0 + n_2 I \quad , \tag{2.47}$$

where n_0 is the linear refractive index, n_2 is the second-order nonlinear refractive index, and I is the pulse intensity, which can be written as

$$I(t) = \left(\frac{n_0 c}{2\pi} \right) \left| \tilde{A}(z,t) \right|^2 \quad . \tag{2.48}$$

$\tilde{A}(z,t)$ can be obtained from the electric field distribution, which is [61, 62]:

$$\tilde{E}(z,t) = \tilde{A}(z,t) e^{i(kz - \omega_0 t)} + c.c. \quad . \tag{2.49}$$

By using $n(I) = n_0 + n_2 I$ and $k = n\omega_0 / c$, the total phase of the pulse can be expressed as

$$\phi = kz - \omega_0 t = \frac{\omega_0}{c} (n_0 + n_2 I) z - \omega_0 t \quad . \tag{2.50}$$

Therefore, the instantaneous frequency $\omega(t)$ can be written as

$$\omega(t) = -\frac{d\phi(t)}{dt} = \omega_0 - \frac{\omega_0}{c} n_2 L \frac{\partial I}{\partial t} \quad , \tag{2.51}$$

where L is the distance the pulse has traveled inside the medium. Therefore, the phase

shift induced by SPM can be expressed as $\delta\omega(t) = -\frac{\omega_0}{c} n_2 L \frac{\partial I}{\partial t}$.

The maximum frequency shift induced by SPM is as following [61]:

$$\delta\omega_{\max} = 0.86\Delta\omega_0\phi_{\max} \quad , \tag{2.52}$$

where $\Delta\omega_0$ is initial spectral width that is inversely proportional to width T_0 ($\Delta\omega_0 = 1/T_0$), and $\phi_{\max}$ is maximum phase shift, which is given as:

$$\phi_{\max} = \gamma P_0 L_{eff} \quad . \tag{2.53}$$

Figure 2.1 shows the simulation of SPM-induced spectrum broadening. To isolate the nonlinear effect to SPM (without high-order nonlinear effects), the equation (2.43) is simplified as following:

$$\frac{\partial A}{\partial z} = i\gamma |A|^2 A \quad . \tag{2.54}$$

The number of peaks M generated by SPM satisfies $\phi_{\max} = (M - 0.5)\pi$ [61]. In this simulation, P_0, L_{eff} and γ are adjusted so that $\phi_{\max} = 9.5\pi$. Therefore, the expected number of peaks due to SPM is 10, which coincides with the simulation result shown in Fig. 2.1.

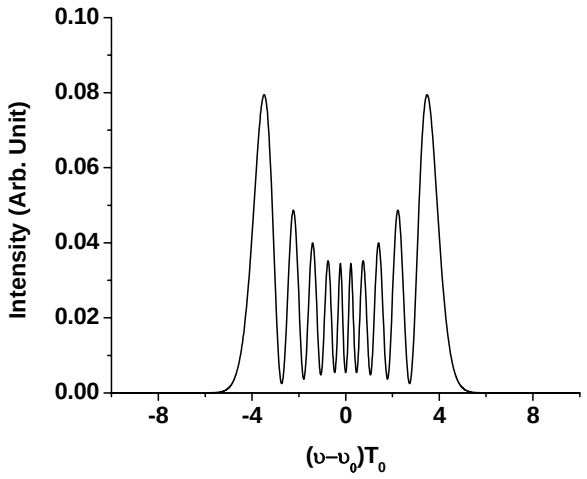

Fig. 2.1. Spectrum broadening induced by SPM effect.

To further investigate the spectrum broadening induced by SPM, simulations using different input power levels of 1 GW/cm^2 and 40 GW/cm^2 in a sapphire fiber are performed. A sapphire fiber with the length of 1cm is pumped at 784nm, in which the dispersion coefficient is $D = -183.71 ps/nm-km$ <0 and it is considered to be in the normal dispersion region. The parameters used for the simulations are pulse width $T_0 = 150 fs$, mode area A_{eff}=2,827μm^2 with the fiber diameter of 60μm, and nonlinear coefficient $\gamma = 8.5x10^{-5}/m.W$. Figure 2.2 shows the simulations of pulses with two different input power levels of 1GW/cm^2 and 40GW/cm^2 traveling into 1cm sapphire fiber. Blue and red solid lines denote to pulses with input power levels of 1GW/cm^2 and 40GW/cm^2, respectively. Figure 2.2 clearly shows that pulses are broadened due to SPM when the input power level is increased from 1GW/cm^2 to 40GW/cm^2. To solidify the simulation evaluations, experimental verification using the same conditions that are the fiber length of 1cm, pulse width of 150fs, and the fiber diameter of 60μm is performed.

Figure 2.3 shows the experimental spectrum when pulses with input power level of 40GW/cm^2 travels into 1cm sapphire fiber. As shown in Fig. 2.3, both simulation and experimental results confirm that the spectrum broadening seems to be caused by SPM, and both results are in good agreement. Detailed theoretical and experimental evaluations on SPM induced in sapphire fibers are performed in Chapter 4. Also, within anomalous dispersion region, two effects of SPM and soliton-dynamics accompanied by SPM according to fiber lengths longer and shorter than dispersion length are explained in Chapter 5.

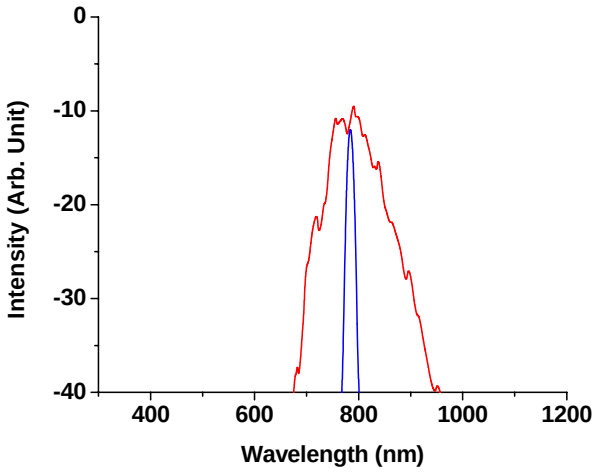

Fig. 2.2. Simulations of pulses with two different input power levels of 1 GW/cm^2 and 40 GW/cm^2 traveling into 1cm sapphire fiber.

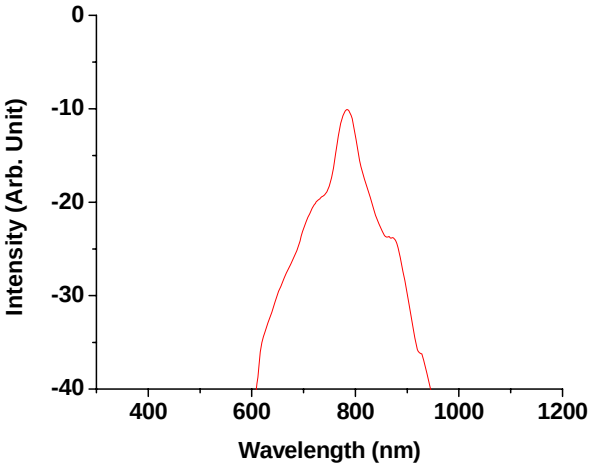

Fig. 2.3. Experimental spectrum of pulses with input power level of 40 GW/cm^2 traveling into 1cm sapphire fiber.

b. Cross Phase Modulation

When two signals with different frequencies co-propagate through an optical fiber, the phase shift of the pulse is induced by another pulse. This effect is called cross phase modulation (XPM). The electric field including two signals with frequencies ω_1 and ω_2 can be denoted as [61]

$$E(r,t)=\frac{1}{2}\hat{x}\left(E_1e^{-i\omega_1 t}+E_2e^{-i\omega_2 t}\right)+c.c. \quad . \tag{2.55}$$

By substituting (2.55) into (2.19), nonlinear polarization P_{NL} can be expressed as [61]

$$P_{NL}=\frac{1}{2}\hat{x}\left[P_{NL}(\omega_1)e^{-i\omega_1 t}+P_{NL}(\omega_2)e^{-i\omega_2 t}\right]+c.c.+FWM \quad , \tag{2.56}$$

where $P_{NL}(\omega_1)=\frac{3\varepsilon_0}{4}\chi^{(3)}_{XXXX}\left(\left|E_1\right|^2+2\left|E_2\right|^2\right)E_1$ (2.57)

and $P_{NL}(\omega_2)=\frac{3\varepsilon_0}{4}\chi^{(3)}_{XXXX}\left(\left|E_2\right|^2+2\left|E_1\right|^2\right)E_2$. (2.58)

The term FWM represents the response due to four-wave mixing (FWM), which can be ignored here since only the effect due to XPM is considered. From (2.57) and (2.58), the refractive index change can be estimated as

$$\Delta n_j \approx \frac{\varepsilon_j^{NL}}{2n_j} \approx n_2\left(\left|E_j\right|^2 + 2\left|E_{3-j}\right|^2\right) \quad , \tag{2.59}$$

where n_2 is the nonlinear refractive index and j=1, 2.

Therefore, the phase shift caused by XPM can be expressed as [61]

$$\phi_j^{NL}(z) = \frac{2n_2\omega_j}{c}\left|E_{j-1}\right|^2 z \quad . \tag{2.60}$$

To investigate XPM effect between pulses with two different wavelengths, simulations using two pulses traveling at wavelengths of 1μm and 1.6μm through a silica fiber are performed. The pulse width used for these pulses is 1ps. Figure 2.4 shows the simulation results when two pulses at wavelengths of 1μm and 1.6μm have input power levels of 10GW/cm^2 and 20GW/cm^2, respectively. To verify that the phase shift of the pulse at 1μm can be induced by another pulse at 1.6μm, the input power level of the pulse at 1.6μm is increased up to 50GW/cm^2 while that of the pulse at 1μm remains as 10GW/cm^2. Figure 2.5 shows the simulation results when two pulses at wavelengths of 1μm and 1.6μm have input power levels of 10GW/cm^2 and 50GW/cm^2, respectively. In Fig. 2.5, the spectrum of the pulse at 1.6μm is broadened due to SPM caused by increased input power level. The spectrum of the pulse at 1μm is also broadened even though the input power level of 1μm remains the same. These results clearly show that XPM can enhance the spectral broadening of each pulse.

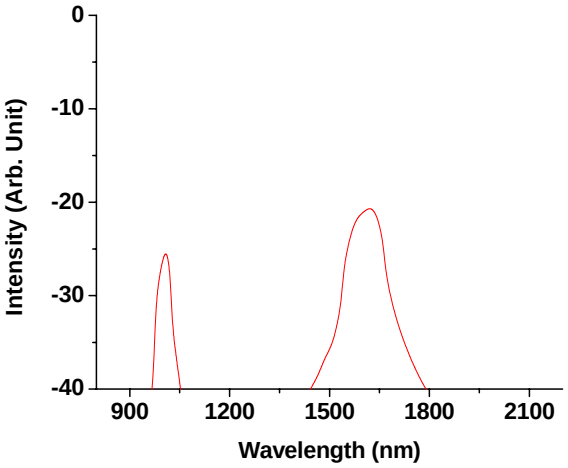

Fig. 2.4. Simulation spectra when two pulses at wavelengths of 1μm and 1.6μm have input power levels of 10GW/cm^2 and 20GW/cm^2, respectively.

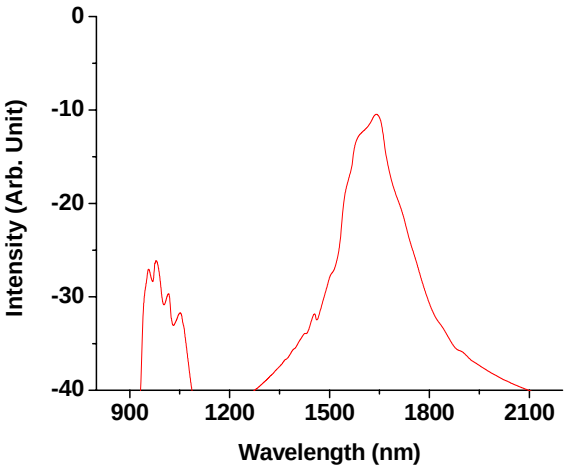

Fig. 2.5. Simulation spectra when two pulses at wavelengths of 1μm and 1.6μm have input power levels of 10GW/cm^2 and 50GW/cm^2, respectively.

c. Four Wave Mixing

When two photons with different frequencies interact with each other in an optical fiber, they are vanished to produce energies at new frequencies. This third order

parametric process is called four wave mixing (FWM).

If it is assumed to include four optical waves at the frequencies of ω_1, ω_2, ω_3, and ω_4, total electric field and nonlinear polarization can be expressed as [61]

$$E = \frac{1}{2}\hat{x}\sum_{j=1}^{4} E_j e^{i(k_j z - \omega_j t)} + c.c. \tag{2.61}$$

and $$P_{NL} = \frac{1}{2}\hat{x}\sum_{j=1}^{4} P_j e^{i(k_j z - \omega_j t)} + c.c. \quad . \tag{2.62}$$

Since the third order polarization can be written as

$$P_{NL} = \varepsilon_0 \chi^{(3)} \vdots EEE \quad , \tag{2.63}$$

P_4 can be expressed as

$$P_4 = \frac{3\varepsilon_0}{4}\chi^{(3)}_{xxxx}\left[|E_4|^2 E_4 + 2\left(|E_1|^2 + |E_2|^2 + |E_3|^2\right)E_4 + 2E_1E_2E_3e^{i\theta_+} + 2E_1E_2E_3^* e^{i\theta_-} + \cdots\right] \quad , \tag{2.64}$$

where $$\theta_+ = (k_1 + k_2 + k_3 - k_4)z - (\omega_1 + \omega_2 + \omega_3 - \omega_4)t \tag{2.65}$$

and $$\theta_- = (k_1 + k_2 - k_3 - k_4)z - (\omega_1 + \omega_2 - \omega_3 - \omega_4)t \quad . \tag{2.66}$$

Upper part of (2.64) is due to SPM and cross phase modulation (XPM) while the bottom part is caused by four wave mixing. For (2.65) and (2.66), two types of FWM are possible. The first possible FWM is obtained when the phase matching condition for θ_+ is obtained. For this case, the energies of photons at ω_1, ω_2, and ω_3 are transferred to ω_4 to have

$$\omega_4 = \omega_1 + \omega_2 + \omega_3 \quad . \tag{2.67}$$

However, the phase matching condition specified above barely occurs for optical fibers [61]. The second possible FWM is obtained when the phase matching condition for θ_-

is obtained. The energies of photons at ω_1 and ω_2 is transferred to ω_3 and ω_4 to have

$$\omega_4 + \omega_3 = \omega_1 + \omega_2 \quad , \tag{2.68}$$

in which the phase matching condition can be expressed as

$$\Delta k = k_3 + k_4 - k_1 - k_2 = \frac{\left(n_3\omega_3 + n_4\omega_4 - n_1\omega_1 - n_2\omega_2\right)}{c} = 0 \quad . \tag{2.69}$$

Detailed explanation of FWM is given in Chapter 6.

d. Stimulated Raman Scattering

Stimulated Raman scattering (SRS) is considered as an inelastic scattering process. For SRS, a light is scattered at the lower frequency of the incident photons due to the molecular vibration in an optical fiber. This newly generated wave at the lower frequency is called Stokes wave. The initial stage of Stokes wave for continuous wave (CW) conditions can be expressed as [61]:

$$\frac{dI_S}{dz} = g_R I_P I_S \quad , \tag{2.70}$$

where g_R has the relationship to the imaginary part of the third order nonlinear susceptibility, I_P is the pump intensity, and I_S is Stokes intensity. When equation $\Omega = \omega_p - \omega_S$, the frequency difference between pump beam at ω_p and Stokes wave at ω_S, stays in the boundary of Raman-gain spectrum, the new frequency Ω is red-shifted due to Raman scattering. g_R measured at pumping wavelength of 1μm for fused silica is shown in Fig. 2.6. As shown in Fig. 2.6, the wave number for maximum Raman gain can be obtained at 440cm^{-1}, whose frequency can be expressed as

$f_{g_R} = \left(3\times10^8 m/s\right)\cdot\left(440cm^{-1}\right) = 13.2THz$. Therefore, new frequency Ω is red-shifted from pump beam ω_p by 13.2THz.

To check the relevance between the theory and the real case when a beam was into an optical medium, q-switched pulses at the wavelength of 523nm were coupled into 300m silica fiber (SMF-28e: single mode fiber for 1550nm) as shown in Fig. 2.7. The q-switched pulse had the pulse width of 11ns (FWHM) and the peak intensity of 16.8kW. An output from the fiber was collimated and was detected by a monochromator (MicroHR, Horiba Jobin Yvon, Inc).

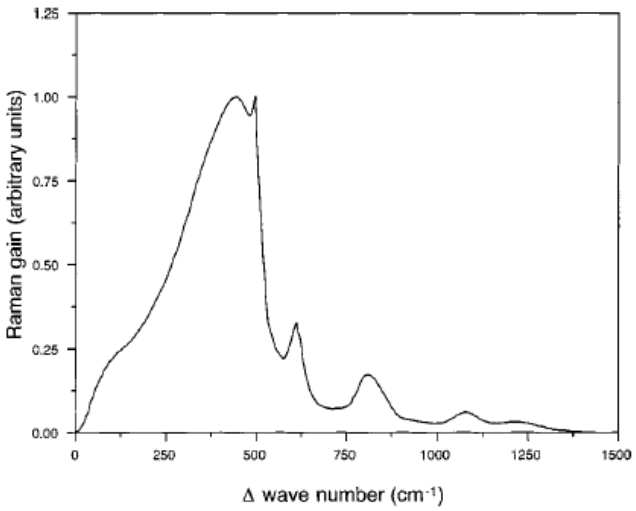

Fig. 2.6. Raman gain spectrum of fused silica: image obtained from [63].

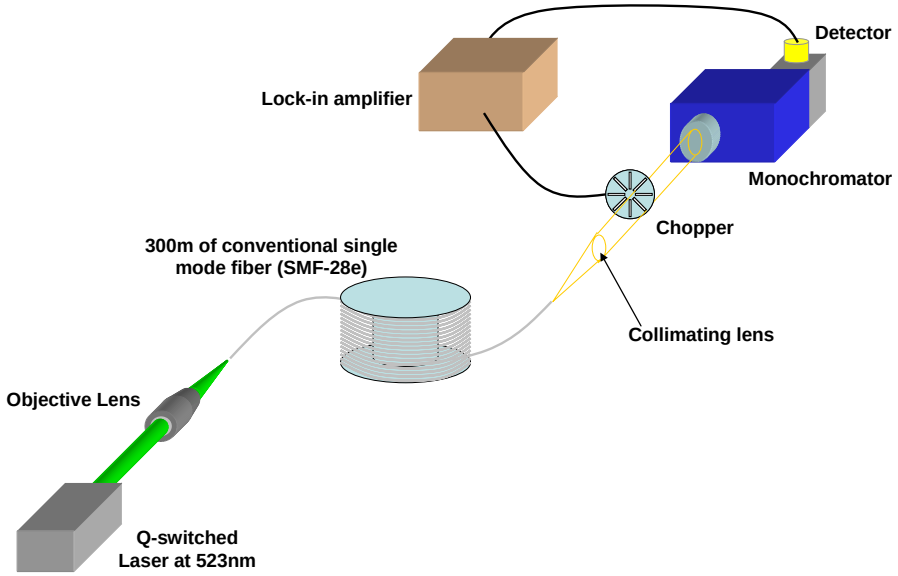

Fig. 2.7. Experimental setup for Raman scattering.

Figure 2.8 shows the spectrum generated from q-switched pulses inside the 300m silica fiber and far-field pattern. The spectrum expansion from 523nm to 1000nm was obtained.

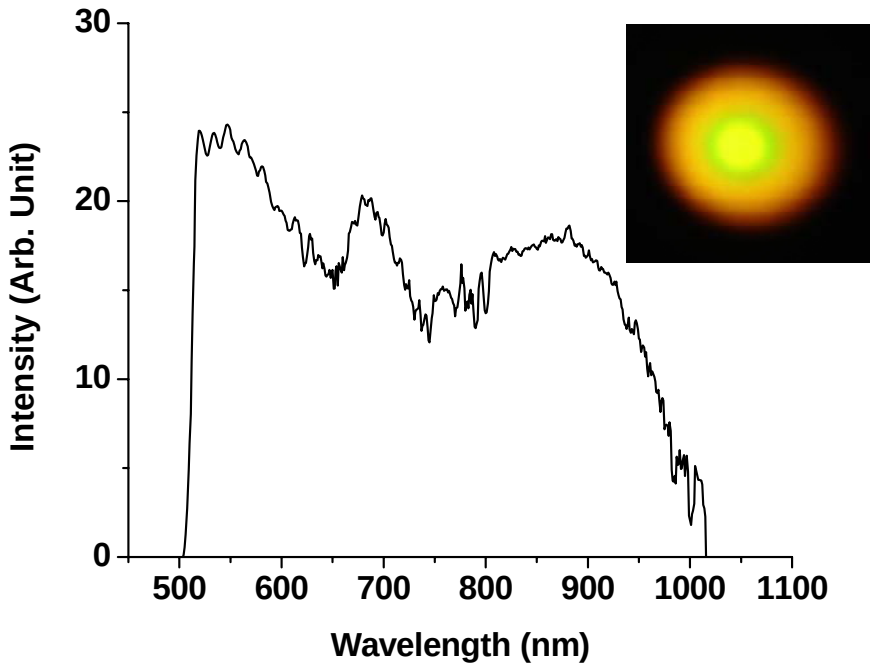

Fig. 2.8. The experimentally measured spectrum generated from q-switched laser (in dB scale).

To investigate the effect of Raman scattering, the spectrum was drawn in linear scale for the intensity and zoomed into narrower wavelength scale as shown in Fig. 2.9. The first shifted peak was observed at 535nm, which coincided with following calculation:

$$\lambda_{Raman} = \frac{3\times10^{8} m/s}{573.6THz - 13.2THz} = 535.33nm ,$$

where 535.33nm peak was red-shifted from 523nm peak by 13.2THz. The second peak was at 548nm, which also matched the following calculation:

$$\lambda_{Raman} = \frac{3\times10^{8} m/s}{560.4THz - 13.2THz} = 548.25nm .$$

All the peaks evaluated up to 5th shift in Fig. 2.9 had good agreements with the calculated

values.

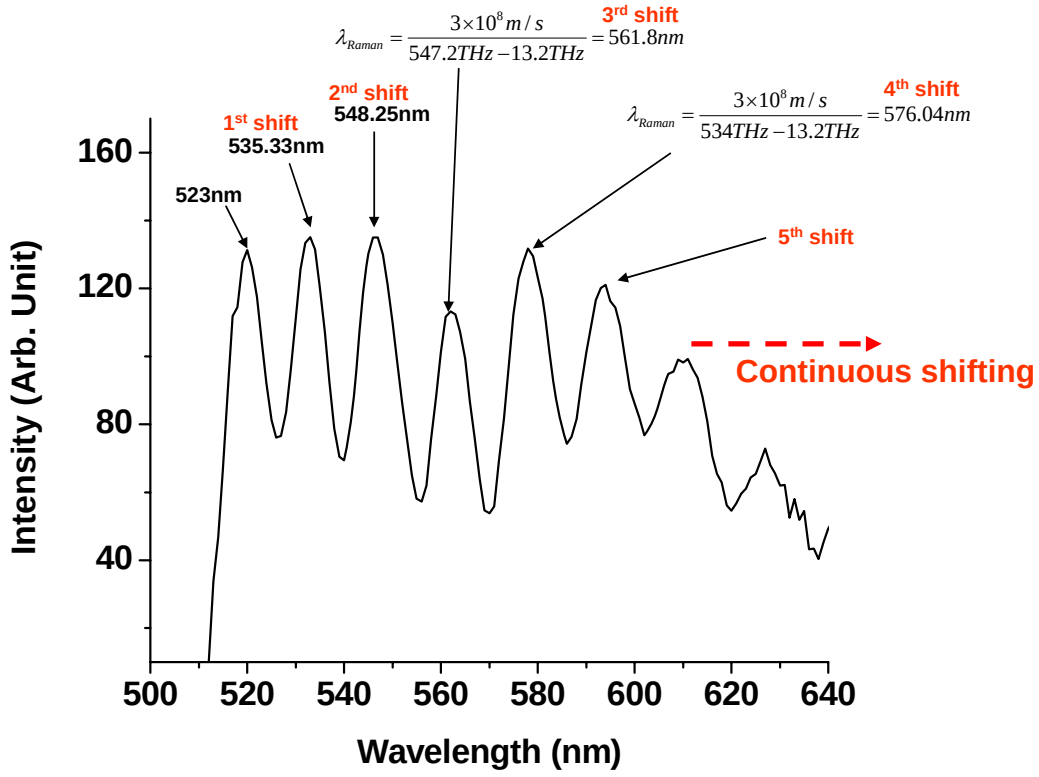

Fig. 2.9. Closer view of the measured spectrum in linear scale: peaks up to 5th shift are evaluated with calculation results.

The threshold peak power for Raman scattering can be defined as [61]:

$$\frac{g_R P_0^{cr} L_{eff}}{A_{eff}} \approx 16,$$

where P_0^{cr}, L_{eff}, and A_{eff} are threshold peak power, effective fiber length, and mode area of an optical medium, respectively. By substituting g_R =1.0×10^{-13}m/W (approximated value from Fig. 1), L_{eff} =300m, and A_{eff} =78.54μm^2 (the diameter of 10μm for SMF-28e) into equation (x), P_0^{cr} is calculated to be 41.89W. Since the peak

power coupled into the 300m fiber (16.8kW) was much above the calculated value, Raman scattering effect was clearly observable in the wide bandwidth range.

However, self-phase modulation (SPM), generally considered as symmetrical broadening, was not observed in Figs. 2.8 and 2.9. Since the value of the nonlinear coefficient can be obtained using (2.33), which is

$$\gamma = \frac{2\pi n_2}{\lambda A_{eff}} = \frac{2\pi\left(2.6\times10^{-20}\, m^2/W\right)}{(523nm)\pi(5\mu m)^2} = 3.977\times10^{-3}/m\cdot W \quad ,$$

$\phi_{\max}$ from (2.53) is calculated to be 20,044. Thus, the value of the maximum frequency shift induced by SPM is given as (2.52):

$$\delta\omega_{\max} = 0.86\Delta\omega_0\phi_{\max} = 0.86\left(\frac{1}{11ns}\right)(20{,}044) = 1.56THz \quad .$$

Since the center wavelength is 523nm (573.6THz), SPM can only broaden the 523nm pulses by 1.41nm to blue and 1.44nm to red. Therefore, the effect of SPM using the nanosecond laser is negligible unless the peak power is extremely high, or high-nonlinearity optical medium is utilized.

Chapter 3

Laser Systems Used for Our Experiments

Ultrafast lasers have gained enormous interests in variety of research areas including laser machining [64-66], chemical reactions [67], frequency mixing [26, 68], supercontinuum generation [69-71], remote sensing [72, 73], Terahertz (THz) generation [24, 25, 74], and many others. In this chapter, laser systems including a femtosecond laser system and an optical parametric amplifier available in our lab are explained since they are key equipments for most experiments performed in this dissertation.

3.1 – Femtosecond Laser System

Many ultrafast lasers are now commercially available in single compact packaging with easily operational on-off switches. However, those single-packaged lasers are unable to provide very high-peak-power pulses, which are required by many applications [54]. To provide high-peak power pulses, many methods to amplify weak-power pulses are suggested. Most common way among various methods is to use chirped-pulse amplification technique [16, 54].

The configuration of femtosecond laser systems employing chirped pulse amplification technique is composed of an oscillator (seed laser), a stretcher, a regenerative amplifier (RGA), a multipass amplifier (MPA), and a compressor. Figure 3.1 depicts the variation of temporal pulse width after each stage [75]. A pulse generated by a seed laser is temporally broadened in a stretcher. If longer wavelength travels faster in time than shorter wavelength inside the stretcher, it is called chirped pulse amplification

(CPA) technique. Reversed mechanism (i.e. shorter wavelength travels faster than longer wavelength in time) is called down-chirped pulse amplification (DPA) technique. The stretched pulse is amplified in two amplifiers (RGA and MPA), and temporally compressed in a compressor. The compressor is considered as the reversed process of the stretcher. Figure 3.2 shows the configuration and pictures of our femtosecond laser system (TITAN Femtosecond Pulse system, Quantronix). The pictures only show zoomed sections.

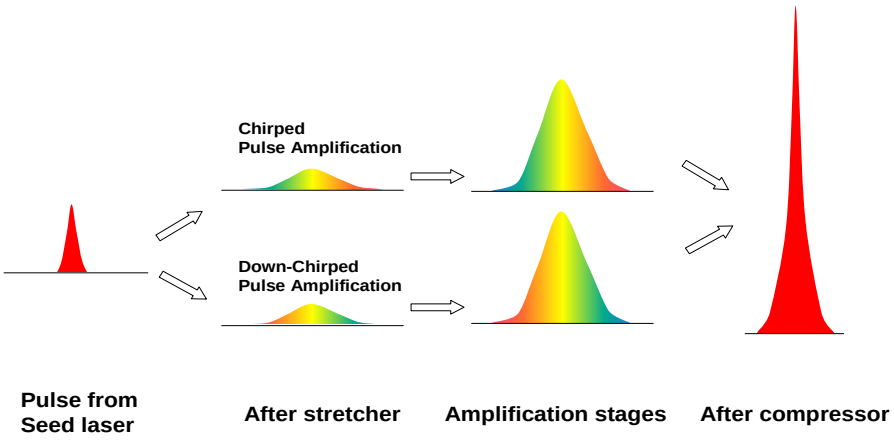

Fig. 3.1. The variation of temporal pulse width through chirped or down-chirped pulse amplification technique (Image reconstructed from [75]).

First, femtosecond pulses with the center wavelength of 780nm are created at the repetition rate of 48.1MHz from a seed laser (IMRA Femtolite A-10). The temporal pulse width at full-width-half-maximum (FWHM) is 99.0fs. The polarization and average output power of pulses are vertical direction and 20.1mW, respectively. Since the pulses out of the seed laser have very short temporal width, which is 99.9fs at full-width-half-maximum (FWHM), they are stretched temporally to picosecond level. The reasons for temporally stretching short pulse in chirped pulse amplification technique are that [54]:

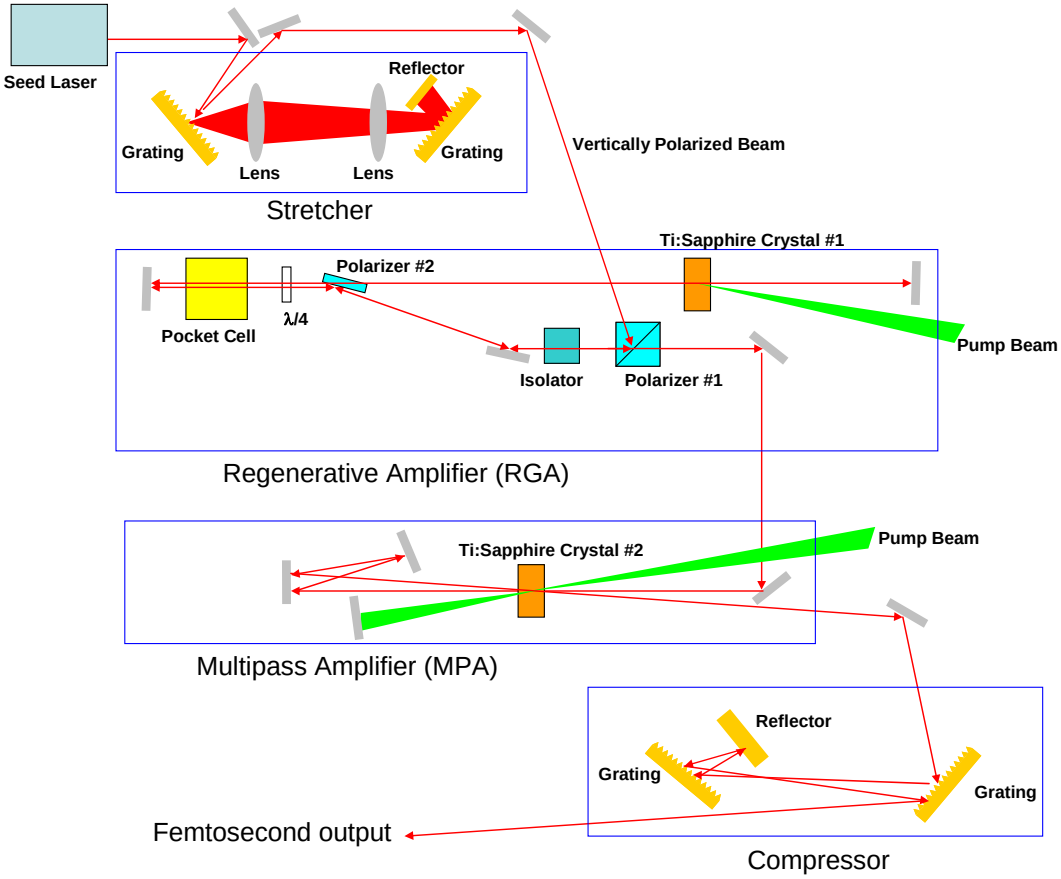

(a)

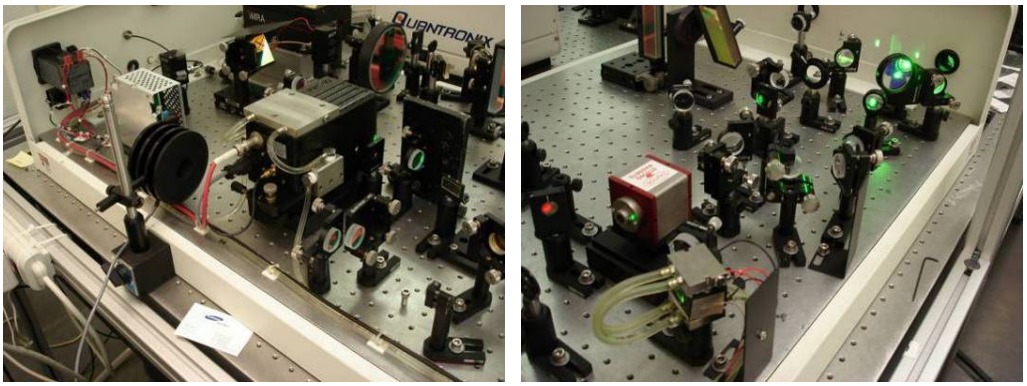

(b)

Fig. 3.2. Our femtosecond laser system: (a) configuration, (b) pictures with selected views.

1) damages to the optics need to be avoided due to extremely high peak power caused in amplification processes, and
2) spatial and temporal beam distortion due to nonlinear interaction can be minimized.

The configuration of a stretcher is shown in Fig. 3.3 [54, 76]. When $f_1>f_2$, longer wavelength travels faster than shorter one that the mechanism is considered to be the CPA as shown in Fig. 3.1. If $f_1<f_2$, it is the DPA as shown in Fig. 3.1, which is also called as negative dispersion stretching. For our case, the reflector is slightly tilted so that the reflected beam can deviate from the incoming beam path and travel into the RGA.

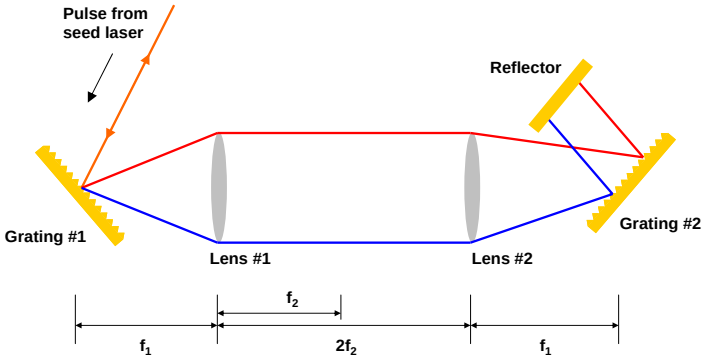

Fig. 3.3. The configuration of a stretcher [54, 76].

Polarizer #1 after the stretcher shown in Fig. 3.2 reflects vertically polarized beam while transmitting horizontally polarized beam. Thus, the incoming beam from the stretcher, which is vertically polarized, is directed into the RGA. Polarizer #2 inside the RGA has the same characteristics as polarizer #1 that it also reflects the vertically polarized incoming beam into a pocket cell driver.

The polarization rotation inside the pocket cell driver is composed of three

operating states, which are zero voltage, λ/4 retardation, and λ/2 retardation [19]. The operation of the pocket cell driver is generally explained based on [19].

In zero-voltage state of the pocket cell driver, a pulse leaving the pocket cell driver is horizontally polarized since the incoming beam reflected by polarizer #2 is λ/4 retarded by a λ/4 wave plate and λ/4 retarded again when it is reflected by a mirror behind the pocket cell driver. Thus, the pulse passes through polarizer #2, and travels inside the cavity of the RGA. After one round trip, the horizontally polarized pulse is rotated back to vertical direction after going through the λ/4 wave plate twice and the pocket cell driver. Therefore, the vertically polarized pulse is reflected by polarizer #2 toward polarizer #1. Since polarizer #1 only transmits the horizontally polarized pulse, an optical isolator, which only rotates the outcoming pulse by 90^{o}, is employed between polarizers #1 and #2 to eject the pulse toward a multipass amplifier (MMA).

In λ/4 retardation state of the pocket cell driver, the pulse can be trapped inside the cavity of the RGA. As soon as the pulse leaves the pocket cell driver, λ/4 retardation is applied to the pocket cell driver. Since total retardation experienced by the pulse inside the cavity is zero (twice of λ/4 retardation by the λ/4 wave plate and twice of λ/4 retardation by the pocket cell driver), the pulse maintains horizontal polarization and is trapped inside the RGA cavity. Also, in the λ/4 retardation state for the pocket cell driver, new pulses coming from the stretcher (vertically polarized) cannot enter the RGA cavity since their polarization is maintained and they are always reflected by polarizer #2. The λ/4 retardation to the pocket cell driver is maintained until the trapped pulse experiences about 15 round-trips inside the cavity.

The trapped pulses are now amplified inside Ti:Sapphire crystal #1 by 15% total

power of a q-switched pump beam generated from a second harmonic ND:YLF laser (Falcon 527 series, Quantronix), which has the wavelength of 532nm, average power of 16.7W, pulse width (FWHM) of 142ns, and the frequency of 1kHz. A Ti:Sapphire crystal is the most commonly utilized for amplification process since it exhibits high damage threshold of 8-10J/cm^2, broad gain bandwidth of 230nm, high thermal conductivity of 46W/mK at 300K, large saturation fluence of 0.9J/cm^2, and good peak gain cross section of 2.7×10^{-19}cm^2 [54]. To maximize the amplification efficiency and avoid the unexpected spectrum modulation due to the induced birefringence, Ti:Sapphire crystal #1 needs to be orientated parallel to the polarization (horizontal direction) of the pulse inside the cavity. The center wavelength measured after the amplification inside Ti:Sapphire crystal #1 is 784nm, which is 4nm deviated from the seed laser (center wavelength ~ 780nm). According to Backus et al [54], the center wavelength can be red-shifted in an amplification medium since the gain saturation tends to shift the spectrum toward the peak gain of the Ti:Sapphire crystal, which is around 840nm as shown in Fig. 3.4.

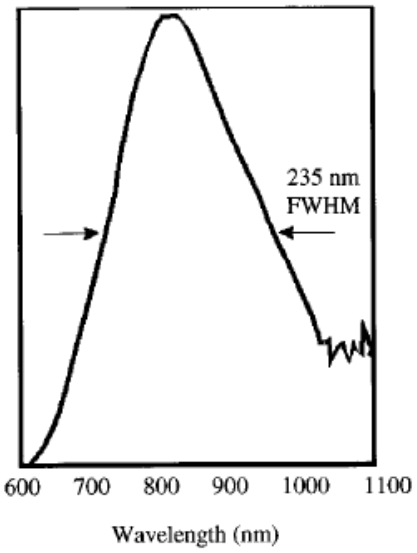

Fig. 3.4. Gain cross section of Ti:Sapphire crystal (Image obtained from [54]).

When the energy of the pulse inside the cavity approaches the maximum gain, λ/2 retardation is applied to the pocket cell driver so that the amplified pulse trapped inside the cavity leaves the cavity. The average power of the seed beam after the RGA is about 400mW. The pulse after the application of λ/2 retardation is vertically polarized since the pulse experiences λ/4 retardation twice by the λ/4 wave plate and 90^{o} twice by the pocket cell driver. The emitted seed beam from the RGA cavity travels through the optical isolator, and its polarization is changed to horizontal direction. The horizontally polarized pulse passes through polarizer #1 and travels into the MMA.

The configuration of the MMA in Fig. 3.2 shows that the seed beam ejected from the RGA cavity is amplified twice inside Ti:Sapphire crystal #2. The seed beam travels into the crystal, and is reflected toward the crystal again by hitting several mirrors. 85% of the total average pumping power from Falcon 527 ND:YLF laser is applied to Ti:Sapphire crystal #2. To maximize the amplification of the pulse, the pump beam passing through Ti:Sapphire crystal #2 is reflected back to the crystal again by an end mirror. The average power of the seed beam after the MMA is about 3W.

The polarization of the seed beam is rotated to vertical direction by entering a λ/2 wave plate, and travels into a compressor. The compressor is very close to the reverse operation of the stretcher explained earlier. Since the CPA technique is employed for the stretcher, the reverse operation that the shorter wavelength travels faster than the longer wavelength is applied to the compressor. The average power of the seed beam is decreased to around 2W due to metallic absorption loss and higher-order diffraction of the grating surfaces.

3.2 - Optical Parametric Amplifier

Even though femtosecond laser systems using Ti:Sapphire crystals provide high stability and intense peak power, the ability of wavelength tuning is limited to small range [17, 54]. Their wavelength tuning ability can be greatly enhanced from UV to even far-IR if they are incorporated together with nonlinear optical crystals such as β-barium borate (BBO) and lithium triborate (LBO) for frequency mixing processes, which can generate different frequencies other than the pumping wavelength [17, 62].

An optical parametric amplifer (OPA), which is based on differential frequency generation (DFG), is the most common way to realize the wavelength shift into mid- and far-IR regions. When high intensity femtosecond pulse (ω_P) propagates into a nonlinear optical crystal, it interacts with quantum noise inside the crystal to generate new wave, which is called signal beam (ω_S) [77]. Those two beams (ω_P and ω_S) are involved in DFG process, and create another new wave, which is called idler beam (ω_I) [17, 62, 77, 78]. These parametric amplification processes can be expressed as [17, 62, 77, 78]:

$$\omega_P = \omega_S + \omega_I \quad . \tag{3.1}$$

To ensure efficient amplification of both signal and idler beams, following phase matching condition needs to be followed:

$$n_P\omega_P = n_S\omega_S + n_I\omega_I \quad , \tag{3.2}$$

where n_p, n_s, and n_I are refractive indices of pump, signal and idler beams, respectively. Therefore, wavelengths of signal and idler beams can be continuously tuned by varying n_p, n_s, and n_I, which can be controlled by varying orientation, temperature, pressure or electric field of a crystal [17]. In our OPA configuration [Traveling-wave Optical Parametric Amplifier of Superfluorescence (TOPAS), Light Conversion], a BBO crystal

with type I, in which the polarization of both signal and idler beams are the same (ordinary direction) while they are perpendicular to the pump beam (extraordinary direction), is utilized. In that case, the phase matching angle (θ_m), which decides the wavelengths of signal and idler beams, can be expressed as [17]:

$$\theta_m = \sin^{-1}\left[\frac{n_{ep}}{n_{ep}(\theta_m)}\sqrt{\frac{n_{op}^2 - n_{ep}^2(\theta_m)}{n_{op}^2 - n_{ep}^2}}\right] \quad , \tag{3.3}$$

where n_{ep} and n_{op} are the refractive indices of the pump beam, which are oriented in extraordinary and ordinary directions, respectively.

The configuration and picture of our OPA is shown in Fig. 3.5. The OPA is composed of 5 stages. The first three stages are to generate stable signal and idler beams as shown in Fig. 3.6 while last two stages are to amplify signal and idler beams inside the crystal by overlapping them with pumping beams as shown in Figs. 3.7 and 3.8.

In the first pass, a seed beam, around 10% of the pump beam after the first and second beam splitters (BS1 and BS2), is reflected by M2, and passes through the crystal to generate weak signal and idler beams due to the interaction with quantum noise and the DFG process of $\omega_I = \omega_P - \omega_S$. In the second and third passes, signal and idler beams are amplified twice and reach diffraction grating (DG), which is utilized to reduce the spectral width and stabilize the shape of signal and idler beams.

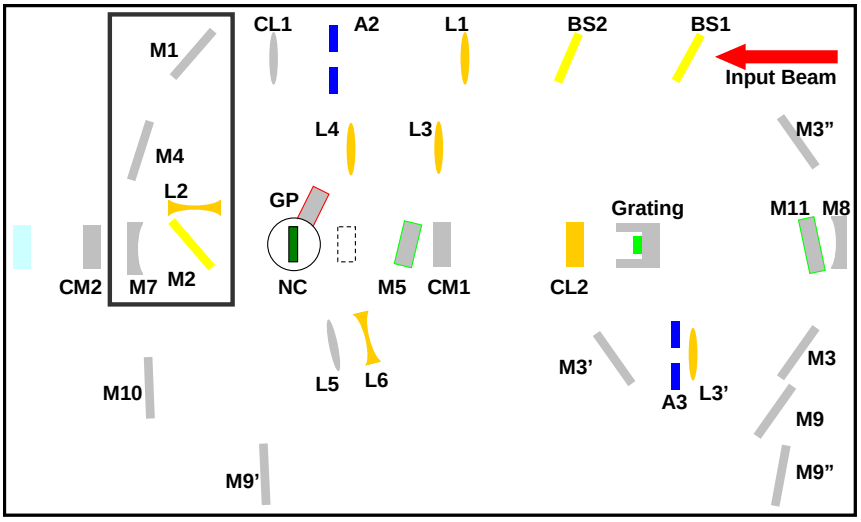

(a)

(b)

Fig. 3.5. The OPA: (a) configuration, (b) picture.

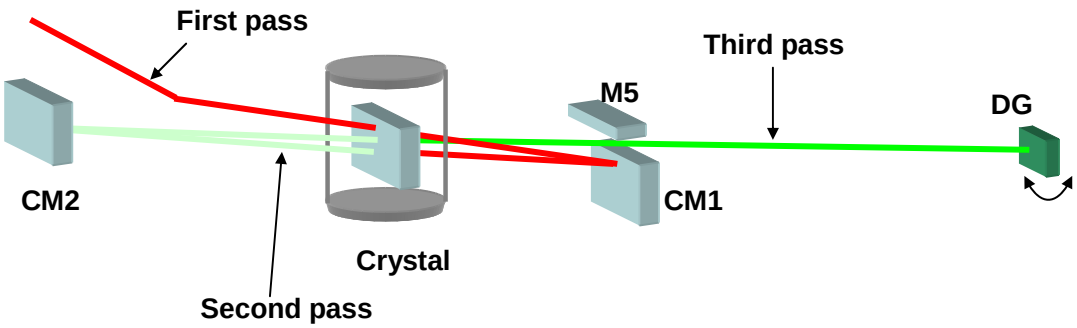

Fig. 3.6. First, second, and third passes to generate and amplify signal and idler beams.

In the fourth pass, the beam reflected by the diffraction grating is amplified inside the crystal by being overlapped with the pump beam reflected by BS2 as shown in Fig. 3.7. In the fifth pass, the beam amplified in the fourth pass is reflected by M7 and M8, and is amplified again by being overlapped with the pump beam reflected by BS1 as shown in Fig. 3.8.

The wavelength range achieved by this configuration is from 1100nm to 2600nm. To further extend the wavelength tuning ability, our OPA employs an external BBO crystal to generate new frequency due to DFG process between signal and idler beams ($\omega_{NEW} = \omega_S - \omega_I$). In this case, wavelength tuning ability can reach up to 11μm, which is suitable to pump fibers at mid-IR region.

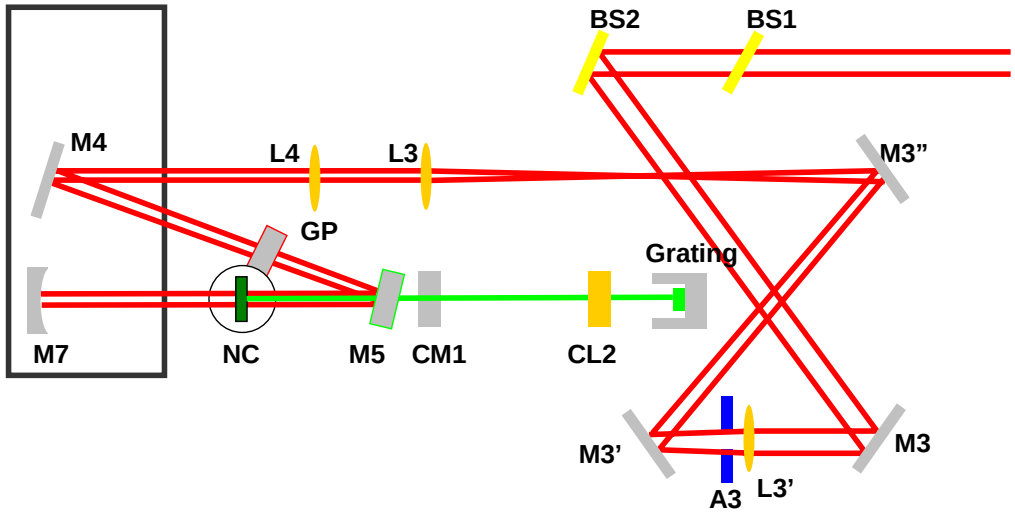

Fig. 3.7. Fourth pass: Pre-amplification stage.

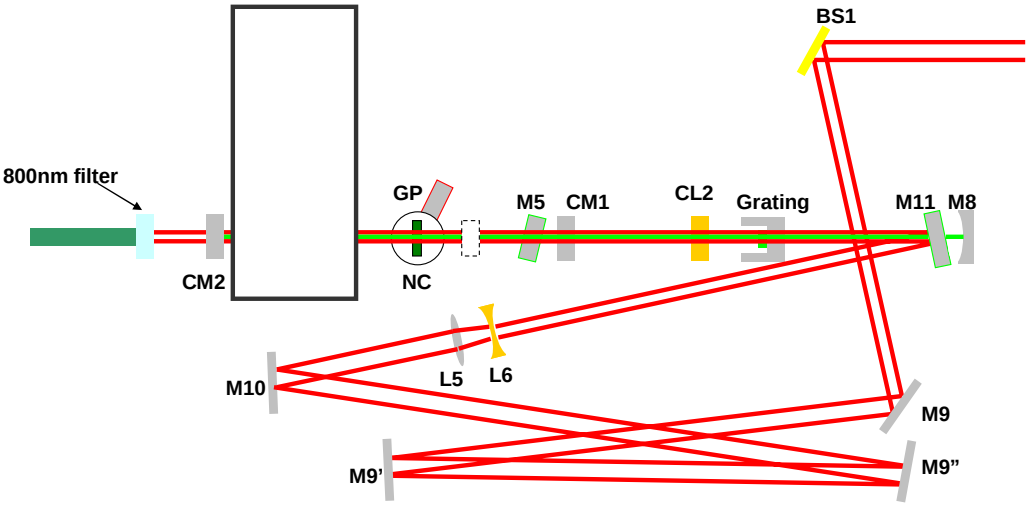

Fig. 3.8. Fifth pass: Power-amplification stage.

Chapter 4

Investigation of Single Crystal Sapphire Fiber as a Medium for Supercontinuum Generation

4.1 – Introduction

To overcome the limitations of conventional silica glass and IR glass fibers that are high absorption beyond 2.5μm and low damage threshold, we mainly utilized single crystal sapphire fibers to realize supercontinuum generation (SCG). As explained in Chapter 1, due to their good transparency in mid-IR [40], high laser damage threshold [41], and high melting temperature [40], sapphire fibers has been attractive optical media for many applications including various sensing in harsh environment and high laser power delivery in medical instruments [41, 43, 45, 47, 79]. However, sapphire fibers have not been used for supercontinuum generation even though they are fully qualified for this application.

In this chapter, we review the material and optical characteristics of single crystal sapphire fibers, and further investigate their possibility as optical media for high-power and broadband supercontinuum sources.

4.2 - Material Characteristics of Sapphire Fibers

Sapphire fibers can be readily grown by laser-heated pedestal growth (LHPG) technique [40, 58, 59, 80]. Figure 4.1 shows the configuration of the LHPG [40]. Sapphire source fed into Molten Zone is melted by high power CO_2 laser beam. Then, sapphire material can be slowly pulled out of Molten Zone in the form of a fiber. The

diameter of a sapphire fiber can be decided by feeding speed and the diameter of the sapphire source and the pulling speeds of the sapphire fiber in following relationship [40]:

$$\frac{d_s}{d_f} = \sqrt{\frac{v_f}{v_s}} \quad , \tag{4.1}$$

where d_s and d_f are the diameters of the sapphire source and sapphire fiber, and v_s and v_f are the feeding speed of the source and pulling speed of the fiber. Figure 4.2 shows the spectrum losses of typical bulk sapphire material and the sapphire fiber grown at Rutgers University [40]. As shown in Fig. 4.2, low mid-IR loss of the sapphire fiber satisfies that the sapphire fiber is a suitable optical medium to generate supercontinuum in mid-IR region.

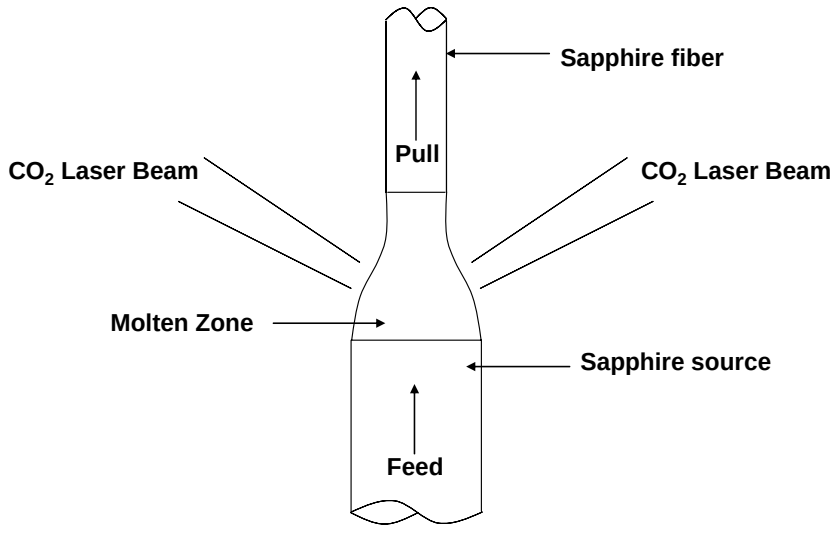

Fig. 4.1. Configuration of laser-heated pedestal growth (LHPG) (Redrawn from [40]).

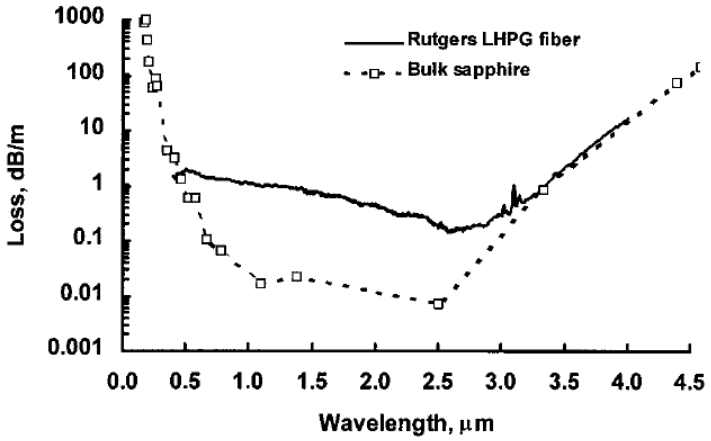

Fig. 4.2. Spectrum losses of typical bulk sapphire crystal and the sapphire fiber grown at Rutgers University (Image obtained from [40]).

4.3 - Optical Characteristics of Sapphire Fibers

In this dissertation, c-axis single crystal sapphire fibers are employed for all the experiments. Therefore, the ordinary refractive index of a sapphire fiber only needs to be considered, and can be expressed as following Sellmeier equation [81]:

$$n(\lambda)=\sqrt{1+\frac{1.4313496\lambda^2}{\lambda^2-(0.0726631)^2}+\frac{0.65054713\lambda^2}{\lambda^2-(0.1193242)^2}+\frac{5.3414021\lambda^2}{\lambda^2-(18.028251)^2}} \quad . \tag{4.2}$$

Also, the group velocity and group index can be expressed as follows [82]:

$$v_g=\frac{c}{n-\lambda(dn/d\lambda)}=\frac{c}{N} \quad \text{, and} \tag{4.3}$$

$$N=n-\lambda\frac{dn}{d\lambda} \quad . \tag{4.4}$$

The refractive index, group velocity, and group index of a sapphire fiber are plotted and shown in Fig. 4.3. The dispersion parameter, which has the relationship between group delay changes according to wavelength variation as following [61, 82]:

$$D(\lambda) = \frac{1}{c}\frac{dN}{d\lambda} = -\frac{\lambda}{c}\frac{d^2 n}{d\lambda^2} \quad . \tag{4.5}$$

Figure 4.4 depicts the calculated material dispersion as a function of wavelength for the sapphire fiber. Zero-dispersion wavelength (λ_D), where D=0, is located around 1314nm. A region with $D < 0$ is called normal dispersion while the other ($D > 0$) is called anomalous dispersion [61]. Fiber dispersion can also be expressed as the mode-propagation constant β in a Taylor series [61]:

$$\beta(\omega) = n(\omega)\frac{\omega}{c} = \beta_0 + \beta_1(\omega - \omega_0) + \frac{1}{2}\beta_2(\omega - \omega_0)^2 + \cdots \quad , \tag{4.6}$$

where ω_0 is the center frequency and $\beta_m = \left(\frac{d^m \beta}{d\omega^m}\right)_{\omega=\omega_0}$. (4.7)

The parameters β_1, β_2, and β_3 … can be expressed with previously given parameters as [61, 82]

$$\beta_1 = \frac{1}{v_g} = \frac{N}{c} \quad , \tag{4.8}$$

$$\beta_2 = -\frac{\lambda^2}{2\pi c} D(\lambda) \quad \text{, and} \tag{4.9}$$

$$\beta_3 = \frac{\lambda^3}{2\pi^2 c^2}\left[D(\lambda) + \frac{\lambda}{2}\frac{dD}{d\lambda}\bigg|_{\lambda} \right] \text{ , and so on.} \tag{4.10}$$

Figure 4.5 shows β_2 as a function of a wavelength for the sapphire fiber.

Another important parameter for nonlinear operation is nonlinear refractive index, which can be denoted as n_2. Figure 4.6 shows the nonlinear refractive index of the sapphire material in a function of wavelength [42]. At 784nm, n_2 is about $3\times10^{-20}\ m^2/W$, which is comparable to that of a silica material ($2.6\times10^{-20}\ m^2/W$) [42,

61].

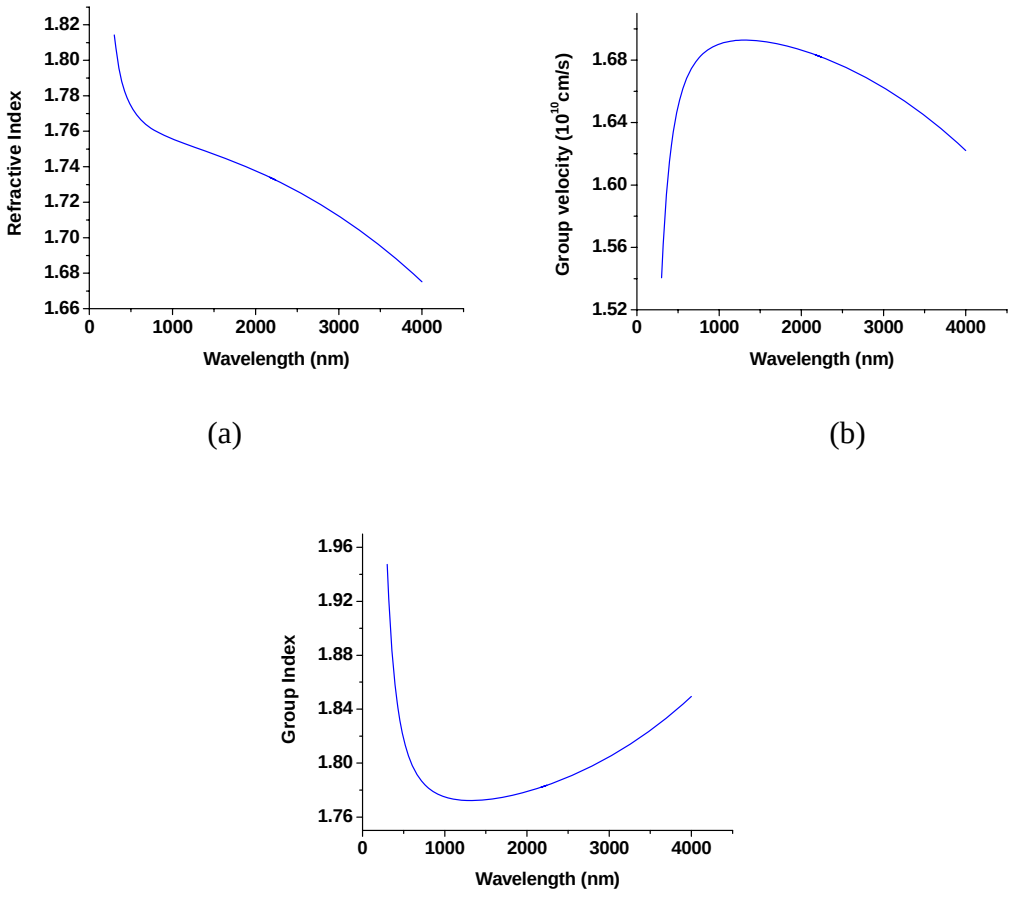

(a) (b)

(c)

Fig. 4.3. Optical properties of a sapphire fiber : (a) refractive index, (b) group velocity, and (c) group index.

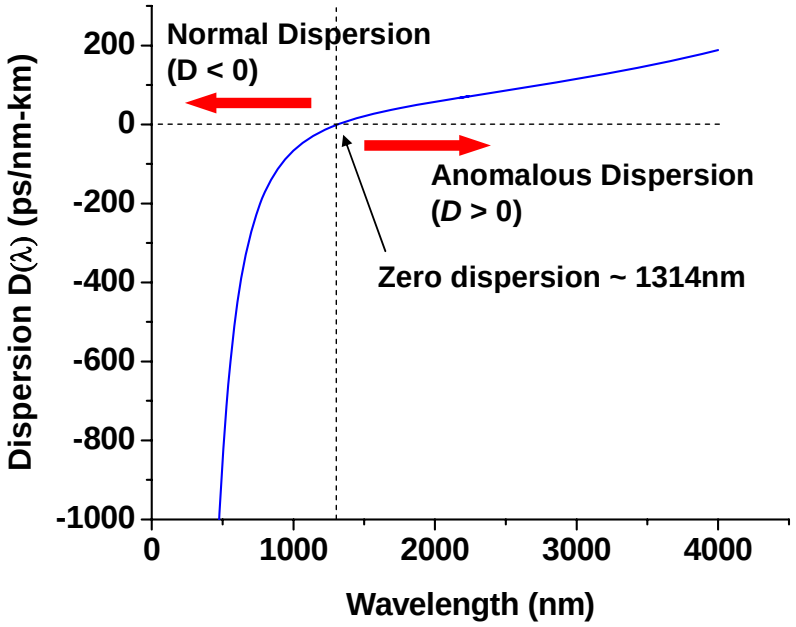

Fig. 4.4. Calculated material dispersion for the sapphire fiber.

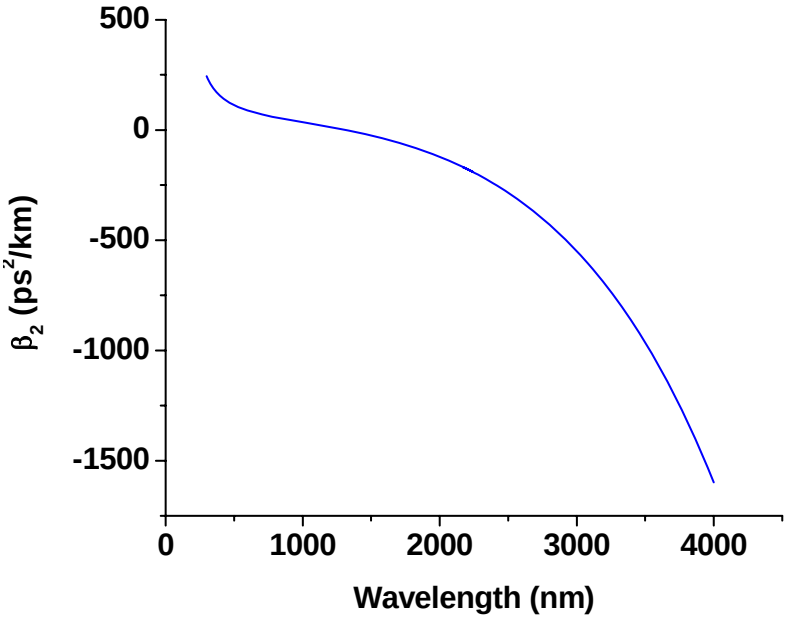

Fig. 4.5. Calculated β_2 for the sapphire fiber.

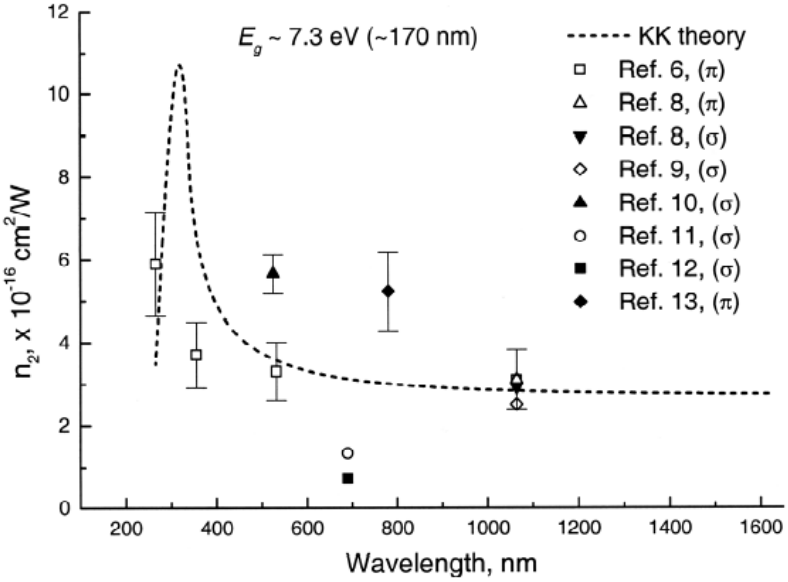

Fig. 4.6. Nonlinear refractive index of the sapphire material (image obtained from [42]).

4.4 - Supercontinuum Generation in Sapphire Fibers

a. Theoretical Approach

Under the slowly varying envelope approximation (SVEA) [61], the generalized nonlinear schrödinger equation (NLSE) describing single pulse propagation in an optical fiber can be mathematically described as [61, 83, 84]:

$$\frac{\partial A}{\partial z}+\frac{\alpha}{2}A-\sum_{n\geq 2}\frac{i^{n+1}}{n!}\beta_n\frac{\partial^n A}{\partial T^n}=i\gamma\left(1+\frac{i}{\omega_0}\frac{\partial}{\partial T}\right)A\cdot\int_{-\infty}^{+\infty}R(T')\left|A(z,T-T')\right|^2dT' \quad , \qquad (4.11)$$

where A represents the slowly varying pulse envelope, α is the fiber loss, β_n is the nth propagation constant, γ denotes the nonlinearity coefficient, and $R(t)$ is the instantaneous and the delayed material response. Raman frequency shift of a sapphire fiber is 419cm^{-1} and Raman gain coefficient is $4.6\times10^{-10}\ cm/W$ [85, 86].

For all the experiments involving sapphire fibers, highly multimode sapphire fibers (core diameter of 60μm for SCG pumped at 784nm, and 115μm for the rest of experiments) are employed (MicroMaterials, Inc). Even though our fibers are highly multimode, the fundamental mode is mainly considered because wave-vector mismatch between the fundamental and higher-order modes is extremely large [87, 88]. The total dispersion is dominated by the material dispersion of the fundamental mode [89].

b. Supercontinuum Generation in Single Crystal Sapphire Fibers by Pumping at 784nm (normal dispersion)

To investigate if a single crystal sapphire fiber is an appropriate medium for SCG, SCG in a c-axis single crystal sapphire fiber is evaluated by pumping at 784nm. According to Fig. 4.4, the value of the dispersion coefficient at 784nm is $D = -183.71 ps/nm-km$ <0, which is normal dispersion region.

To evaluate the effect of the dispersion in SCG, dispersion and nonlinear lengths, given as L_D and L_{NL}, are investigated. Mathematically, L_D and L_{NL} are given by $L_D = T_0^2/|\beta_2|$ and $L_{NL} = 1/\gamma P_0$ [61], respectively, where T_0 is the pulse width, β_2 is the group velocity dispersion, γ is the nonlinear coefficient, and P_0 is the peak power. According to Fig. 4.5, the value of β_2 is around 59 ps^2/km at the pump wavelength of 784nm. Substituting pulse width $T_0 = 150 fs$ into the above expression of L_D, we can obtain $L_D = 39cm$. Since the lengths of sapphire fibers used in this experiment are less than 3cm, the dispersion length is much longer than the length of the fiber used in the experiment. Therefore, the nonzero dispersion at 784 nm will have very little influence on

the spectrum broadening. To find L_{NL}, we need to determine nonlinear coefficient, γ, which is expressed in (2.33) as $\gamma = n_2\omega_0/cA_{eff} = 2\pi n_2/\lambda A_{eff}$, where the nonlinear-index coefficient, n_2, is $n_2 \approx 3x10^{-20}\, m^2/W$ as given in Fig. 4.6 [42] and the effective area is $A_{eff} = 2827\,\mu m^2$ for the multimode sapphire fiber with 60μm diameter. Based on these parameters, one can get $\gamma = 8.5x10^{-5}/m.W$ at $\lambda = 784\,nm$. To calculate the nonlinear length, the peak power coupled into a sapphire fiber is required. The ultra-short pulses has a 5 mm beam size ($D = 5\,mm$) and are focused by a 5× microscope objective with a 25.4 mm focal length, $f = 25.4\,mm$, as illustrated in Fig. 4.7. The spot size, $2\omega_o$ (where ω_o is the waist radius), of the focused Gaussian beam is calculated about 5.071μm near the focal point at $\lambda = 784\,nm$ by using the following Gaussian beam formula $2\omega_o \approx 4\lambda f/\pi D$ [90]. Since this spot size is much smaller than the diameter of the sapphire fiber ($60\,\mu m$), the fiber can be placed 1.5 mm behind the focal plane to cover entire area. Proper spacing is also required to avoid the damage at the end of the fiber. The beam size at the input end of the fiber is estimated by the Gaussian beam propagation formula [90], as given by

$$2\omega(z) = 2\omega_0\sqrt{1+\left(\frac{\lambda z}{\pi\omega_0^2}\right)^2} \quad . \tag{4.12}$$

Substituting $z = 1.5mm$ into the equation above, we obtain $2\omega(1.5mm) = 295\mu m$, which is large enough to cover the entire cross-section of the sapphire fiber. The area proportion between the beam size of $2\omega(1.5mm)$ and the fiber diameter of 60μm is as following:

$$\frac{A_{Beam}}{A_{Fiber}} = \frac{\pi\left(\frac{295.28\mu m}{2}\right)^2}{\pi\left(\frac{60\mu m}{2}\right)^2} = 24.22 \quad . \tag{4.13}$$

If the average power of the input beam is 30mW, the pulse energy coupled into the fiber is

$$E_{pulse-to-fiber} = \frac{30mW}{24.22} \times 0.001s = 1.24\mu J \quad . \tag{4.14}$$

Therefore, the light intensity level coupled into the fiber is:

$$E_{peak} = \frac{Energy_{pulse}}{Width_{pulse} \times A_{beam}} = \frac{1.24\mu J}{150\,fs \times \left(\pi\left(\frac{60\mu m}{2}\right)^2\right)} = 290.64\,GW/cm^2 \quad . \tag{4.15}$$

Also, the lowest light intensity level evaluated is $9.7\,GW/cm^2$.

Then, the corresponding nonlinear lengths are 4.3 cm and 0.14 cm for the peak powers $9.7GW/cm^2 \times A_{eff} = 2.75\times10^5 W$ and $290GW/cm^2 \times A_{eff} = 8.26\times10^6 W$, respectively. Thus, $L_{NL} << L_D$ and the fiber length is compatible or longer than L_{NL}. Therefore, the dispersion term is negligible compared to the nonlinear term and the spectral broadening is dominated by the effect of the self phase modulation [61, 91-93]. Furthermore, since the nonlinear length is in the order of cm, the 3 cm long fiber is more effective for the SCG than the 1 cm long fiber for the SCG.

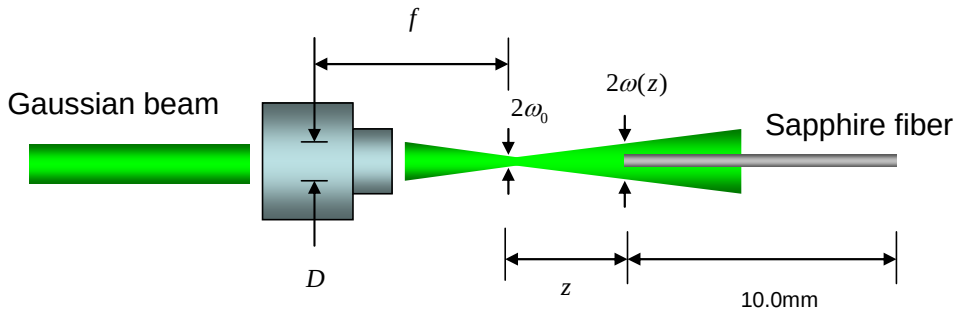

Fig. 4.7. An illustration of power estimation for generating supercontinuum in a sapphire fiber.

To investigate if a single crystal sapphire fiber is an appropriate medium for SCG, a c-axis single crystal sapphire fiber with the core diameter of 60μm was pumped by a Quantronix femtosecond laser, which had a central wavelength, pulse duration, and repetition rate of $\lambda = 784nm$, 150 fs, and 1 kHz, respectively. The experimental setup is shown in Fig. 4.8. Supercontinuum generated inside the sapphire fiber was collimated and focused into an optical spectrum analyzer (OSA). For the purpose of comparison, a bulk sapphire crystal was also placed in the same location of the experimental system, as illustrated in Fig. 4.9. Since the only bulk sapphire crystal available in our lab was 1 mm thick, both the lengths of the sapphire crystal and the length of the fiber were selected to be 1 cm.

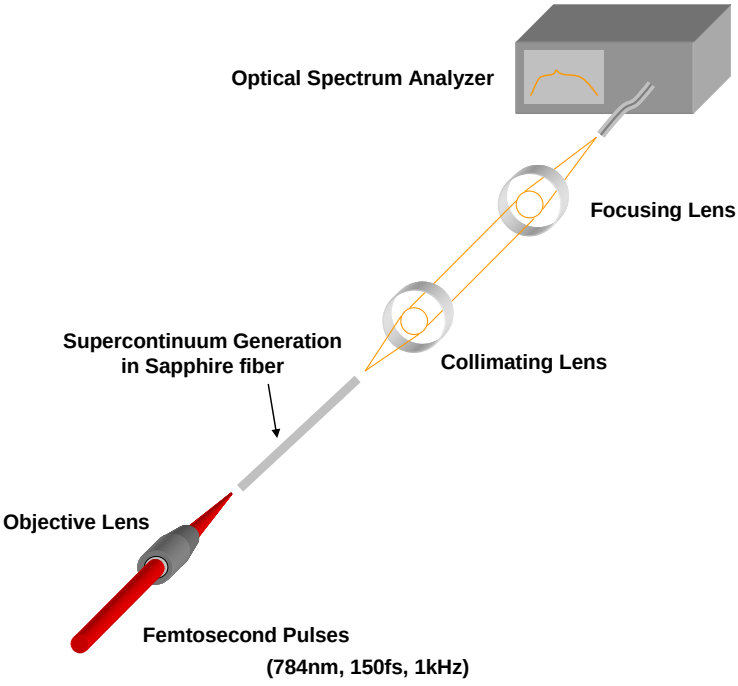

(a)

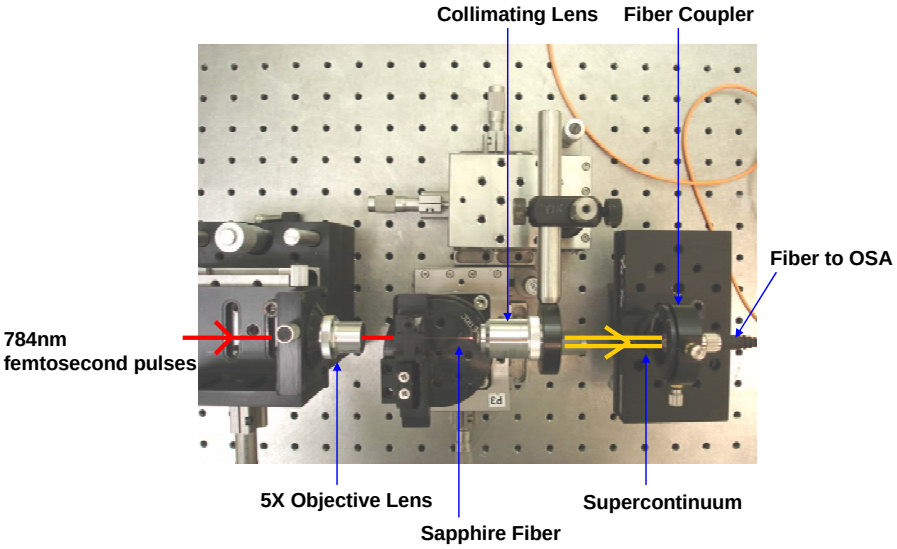

(b)

Fig. 4.8. Experimental setup for SCG in a sapphire fiber by pumping at the wavelength of 784nm: (a) configuration, (b) picture.

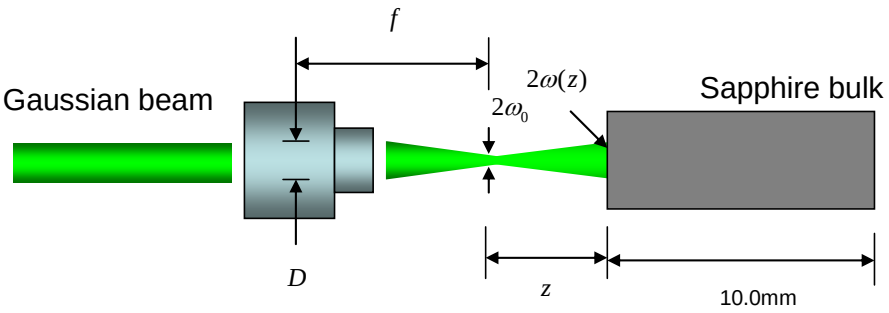

Fig. 4.9. An illustration of the experimental setup for generating supercontinuum in a sapphire bulk.

Figures 4.10(a) - 4.10(d) show the experimentally measured spectra at four different input power levels (i.e., 9.7 GW/cm^2, 48 GW/cm^2, 97 GW/cm^2, and 290 GW/cm^2). The black and red solid lines in each of the figures correspond to the sapphire fiber and sapphire bulk crystal, respectively. Based on these experimental results, we can draw the following conclusions: (1) SCG can be realized in a single crystal sapphire fiber; (2) Using the same exciting light density and interaction length (or material thickness), a wider SCG can be obtained in sapphire fiber than in bulk sapphire because of the fiber's geometry. (3) The threshold light intensity level (9.7 GW/cm^2) for the bulk material was lower than the data reported in [50] (i.e., 20 GW/cm^2). We believed that this difference was because a longer crystal sample (i.e., 1 cm) was used in our experiment (Note that a sample with 2mm length had been used in [50]).

To further investigate the influence of fiber length on SCG, we conducted experiments using different length sapphire fibers. Figures 4.11(a) – 4.11(d) show the experimentally measured spectra from sapphire fibers with different lengths at four different input power levels (i.e., 9.7 GW/cm^2, 48 GW/cm^2, 97 GW/cm^2, and 290

GW/cm^2, respectively). In each of the figures, the red and black solid lines correspond to lengths of 3cm and 1cm, respectively. These experimental results clearly show that the width of the spectrum increases with the length of the fiber.

Note that, as shown in Fig. 4.11(d), the spectral width covered a spectral range from 450nm – 1350nm (almost 900nm). The longer end of the measured spectrum did not extend longer than 1350nm. This was because the pump wavelength is at 784 nm. If a longer pump wavelength is used (will be discussed in next chapters), the longer end of the measured spectrum is expected based on the transmission window of the sapphire material. Figure 4.12 shows the far-field pattern of supercontinuum generated in 3cm sapphire fiber.

Again, the major interests using sapphire fibers for the SCG are the potential wider spectral range (from visible to middle IR up to 5 micron) and higher laser damage threshold. The preliminary experimental results in this chapter serve the purpose of proof-of-concept. In next chapter, SCG in a sapphire fiber by pumping at longer pump wavelengths will be evaluated.

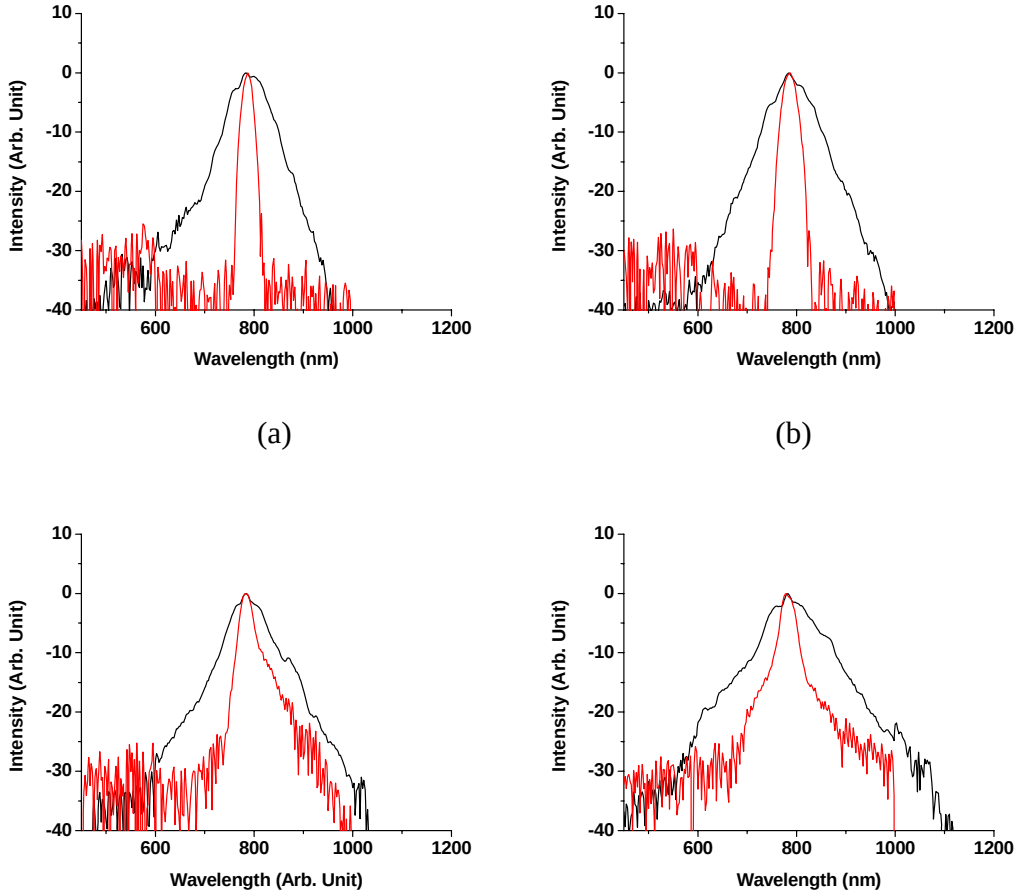

Fig. 4.10. Experimental supercontinuum spectra generated in different forms of sapphire media (i.e., fiber and bulk forms) under different exciting light intensities. Both the lengths of the fiber and the crystal are 1 cm. The black and red solid lines correspond to the fiber and the bulk, respectively: (a) 9.7 GW/cm^2, (b) 48 GW/cm^2, (c) 97 GW/cm^2, and (d) 290 GW/cm^2.

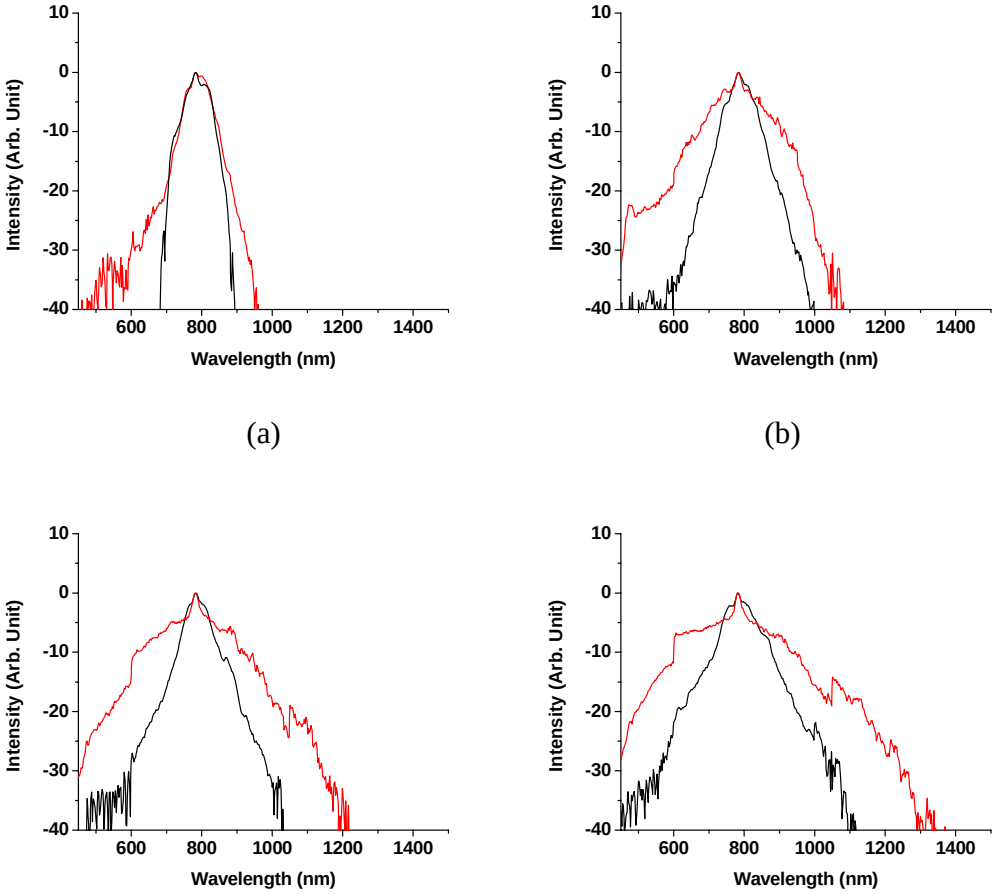

Fig. 4.11. Experimental supercontinuum spectra generated in different length sapphire fibers under different exciting light intensities. The black and red solid lines correspond to 1 cm long and 3 cm long fibers, respectively: (a) 9.7 GW/cm^2, (b) 48 GW/cm^2, (c) 97 GW/cm^2, and (d) 290 GW/cm^2.

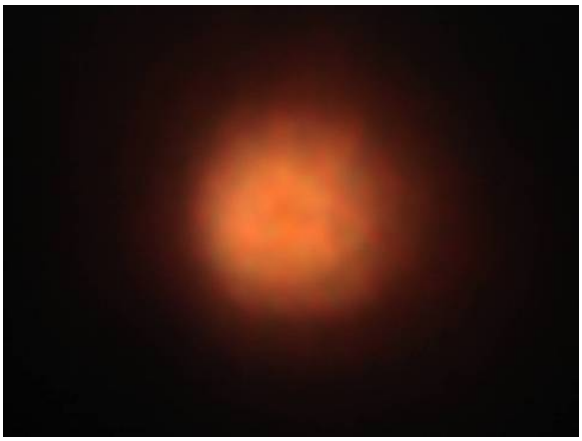

Fig. 4.12. Far-field pattern of supercontinuum generated in 3cm sapphire fiber

Chapter 5

Broadband Supercontinuum Generation in Near- and Mid-IR Using Single Crystal Sapphire Fibers (Pumping in Anomalous Dispersion)

5.1 – Motivation for Pumping at Longer Wavelength Regions

In chapter 1, the disadvantage of time delay due to wavelength tuning using conventional sources such as optical parametric amplifiers (OPOs), tunable solid-state lasers, and quantum cascaded lasers (QCLs) are discussed. Compared to these conventional sources, a supercontinuum source has the advantage of covering a wider range of spectrum without the time delay caused by the wavelength tuning of conventional sources. However, SCG in the mid-IR region using silica materials are limited by heavy material absorption [32]. To realize the SCG in the mid-IR region, IR glass fibers are commonly employed [31, 34-36]. Although mid-IR SCG have been successfully generated in IR glass fibers such as ZBLAN Fluoride fibers, Chalcogenide fibers, and SF-6 fibers, high power supercontinuum sources are not feasible because these IR glass fibers have the low softening temperature as explained in Chapters 1 and 4.

Compared to silica-based fibers and IR fibers, single crystal sapphire fibers (in both the bulk and fiber form) that are transparent up to 5μm, and have a good value of nonlinear refractive index around $n_2=2.8\times10^{-20}m^2/W$ [42], high damage threshold, and a very high melting temperature (> 2,000 ^oC) [40] are good candidates for high power mid-IR SCG.

In this chapter, SCG in near- and mid-IR region using single crystal sapphire fibers is discussed. Also, more detailed study on the mechanism of SCG in single crystal

sapphire fibers is presented by analyzing the relationships between the geometrical fiber length and dispersion length of the sapphire fiber.

5.2 - Technical approach

As given in Chapter 2, the maximum frequency shift induced by the SPM can be expressed as $\delta\omega_{\max} = 0.86\Delta\omega_0\gamma P_0 L_{eff}$ in combination of (2.52) and (2.53). The frequency shift stays within the range of the maximum frequency shift when a fiber is pumped in normal dispersion region (when the wavelength is shorter than 1.3μm) [94]. However, within anomalous region, the formation of higher-order solitons can be observed due to the balance between significant dispersion and SPM [94]. This phenomenon is mainly due to modulation instability [61].

According to the SCG theory in anomalous dispersion region [35, 61], when the fiber length is shorter than the dispersion length, the most dominating effect for supercontinuum generation is thought to be SPM. However, when the fiber length is longer than the dispersion length, the soliton-related dynamics accompanied by SPM dominates the broadening effect. For example, when pump pulses at 2μm travel into single crystal sapphire fiber, SPM is accompanied by anomalous dispersion, creating a dispersive wave at another frequency due to higher-order soliton fission [83, 95-97].

At 2μm, the pumping wavelength, used in our experiments, the dispersion parameter, *D*, is about 57.28ps/nm-km, which falls within the anomalous dispersion region. To investigate the mechanism of SCG in a sapphire fiber, we need to estimate the dispersion length and the nonlinear length of the sapphire fibers at 2μm. To get the value of L_{NL}, first, the nonlinear coefficient γ, is determined by substituting the estimated

nonlinear refractive index coefficient n_2=2.8×10^{-20}m^2/W as shown in Fig. 4.6, the effective area of sapphire fiber A_{eff}=10,386μm^2 (corresponding to 115μm fiber diameter), and λ=2μm into the expression of nonlinear coefficient $\gamma=n_2\omega_0/cA_{eff}=2\pi n_2/\lambda A_{eff}$ as given in (2.33). The calculated nonlinear coefficient is about γ=8.47×10^{-6}/m·W. Then, the nonlinear lengths, L_{NL}, corresponding to different peak powers, can be derived. For example, substituting γ=8.47×10^{-6}/m·W, P_0=30.94GW/cm^2×A_{eff}=3.213×10^{6}W and P_0=154.7GW/cm^2×A_{eff}=1.607×10^{7}W into $L_{NL}=1/\gamma P_0$, the corresponding nonlinear lengths are 3.67cm and 0.735cm, respectively.

To calculate the dispersion length, L_D, we first calculate the value of group velocity dispersion, β_2, which is drawn in Fig. 4.5. The calculated β_2 is about -121.5ps^2/km at λ=2μm. Furthermore, substituting β_2=-121.5ps^2/km and the pulse width T_0=150fs into $L_D=T_0^2/|\beta_2|$, the value of L_D is calculated to be L_D=18.52cm.

Thus, when the fiber length is relatively shorter than 18.52cm, the most dominant effect can be considered as SPM. However, if the fiber length is longer than 18.52cm, interaction of dispersion and SPM can create the dispersive wave due to higher-order soliton fission.

5.3 - Experimental procedures and results

In the experiment, a c-axis single crystal sapphire fiber with a 115μm diameter was used for the SCG. Figure 5.1 shows the experimental set up for SCG in sapphire fiber. The 2μm pumping source was created by using an optical parametric amplifier (OPA) seeded by a femtosecond laser system, which had a 784nm central wavelength, a 1 kHz repetition rate, a 150fs pulse width, and a 5mm diameter beam size. The ultra-short

pulses were focused by a 5× microscope objective with a 25.4mm focal length. The fiber was placed 1.5mm behind the focal plane. The beam size at the input end of the fiber was measured to be 295.3μm, which was larger than the diameter of the sapphire fiber so that the cross section of the fiber end was fully illuminated. According to Fig. 4.4, the material dispersion *D* at 2μm is 57.28ps/nm-km and is considered to be within the anomalous dispersion region. The spectrum obtained from the sapphire fiber was collimated by a Zinc Selenide IR (ZnSe) lens, and measured by a monochromator (MicroHR, Horiba Jobin Yvon Inc.) with a lock-in amplifier. A grating with a blazing wavelength of 1.5μm and a PbS photodetector were used for the 1-2μm range spectral profile measurement and a grating blazed at 4μm and a HgCdTe cryogenic photoreceiver were used for the 2-3μm range spectral profile measurement.

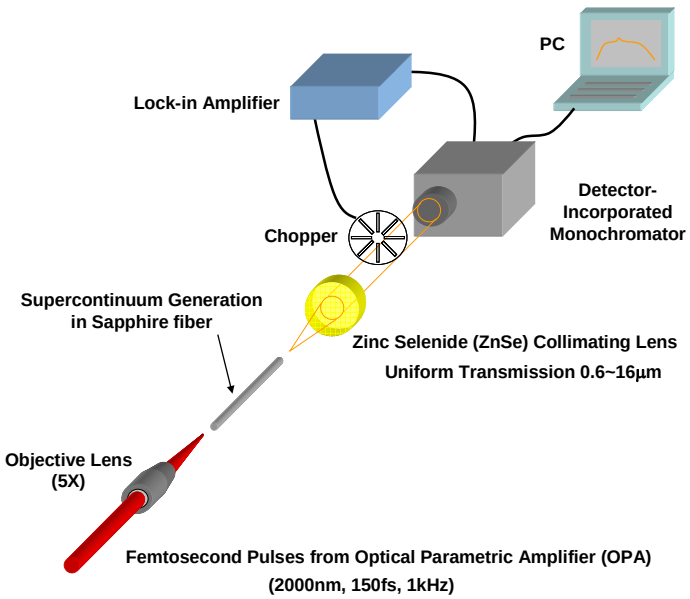

Fig. 5.1. Experimental set up for supercontinuum generation in sapphire fiber

To verify the SCG theory for the case of single crystal sapphire fiber, as discussed in the section of theoretical approach, we first conducted experiments using a sapphire fiber whose length was shorter than the dispersion length (i.e. L_D=18.52cm at 2μm). The fiber chosen for the experiment was 5cm in length. Figures 5.2(a) and 5.2(b) show the experimentally measured spectra from the 5cm sapphire fiber using two different input peak power density levels (i.e. 30.94 GW/cm^2, and 154.7 GW/cm^2, respectively). The corresponding peak power levels within the sapphire fiber are 3.213×10^6W and 1.607×10^7W, respectively. Since the fiber length is shorter than the dispersion length, the most dominating effect that causes spectrum broadening is thought to be SPM [35, 61]. The relatively smooth spectral profiles, shown in Figs. 5.2(a) and 5.2(b) suggested that SPM was indeed the dominant factor for the spectrum broadening. In addition, the experimental results have also shown that a very broad IR spectrum (ranging from 1200 nm to 2800 nm), which covered the near-IR and the lower end of mid-IR spectral range, could be achieved via SCG in single crystal sapphire fibers.

To verify that SCG can also be realized via soliton-related dynamics in single crystal sapphire fibers, we also conducted the experiments with a sapphire fiber whose length was longer than the dispersion length.

Dispersive wave can be created when the following phase matching condition is met [96]:

$$\sum_{n\geq 2}\frac{\beta_n(\omega_0)}{n!}(\omega_R-\omega_0)^n=\frac{\gamma(\omega_0)P_0}{2}, \tag{5.1}$$

where ω_R and ω_0 are the radiation and the dispersive wave frequencies, respectively, and P_0 is the peak power. The soliton order, N, can be determined by $N=\sqrt{L_D/L_{NL}}$ [88].

Substituting L_D=18.52cm and L_{NL}=0.735cm (corresponding to the peak power P_0=1.607×10^{7}W) into the expression of N, we obtain $N = \sqrt{18.52cm/0.735cm} \approx 5$. Table 1 shows calculated dispersion parameter $\beta=(d^m\beta/d\omega^m)$, where m=1, 2….., [61, 82]. By using resonance condition (5.1) and β values given in Table 1, the dispersive wave wavelength is expected at approximately 1.155μm.

Table 1. dispersion parameter β

β_2(ps^2/km)	β_3(ps^2/km)	β_4(ps^2/km)	β_5(ps^2/km)	β_6(ps^2/km)
-121.55	0.529	-2.307×10^{-3}	1.345×10^{-5}	-9.501×10^{-8}

Figures 5.3(a) and 5.3(b) show the experimentally measured spectra for a 35cm long sapphire fiber (longer than the dispersion length) at two different input peak power levels of P_0=3.213×10^{6}W, and P_0=1.607×10^{7}W, respectively. In Fig. 5.3(a), there is a dispersive wave peak appeared around 1.2μm accompanied by SPM. Figure 5.3(b) shows a broader spectrum due to the SPM and higher-order soliton fission. The location of the experimental dispersive wave peak is slightly red-shifted (around 40nm), which may be due to the uncertainty in the dispersion curve of the sapphire fiber and complicated higher-order soliton periodic evolutions [96]. At any rate, the spike shape spectral profiles, shown in Figs. 5.3(a) and 5.3(b), confirmed that SCG could also be generated in single crystal sapphire fibers via soliton-related dynamics when the fiber length was longer than the dispersion length.

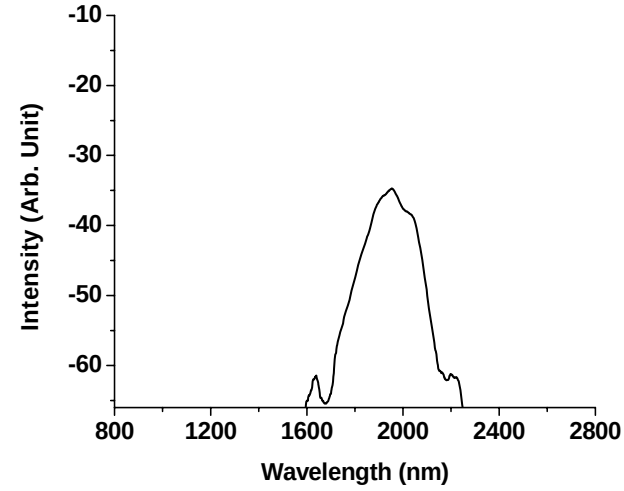

(a)

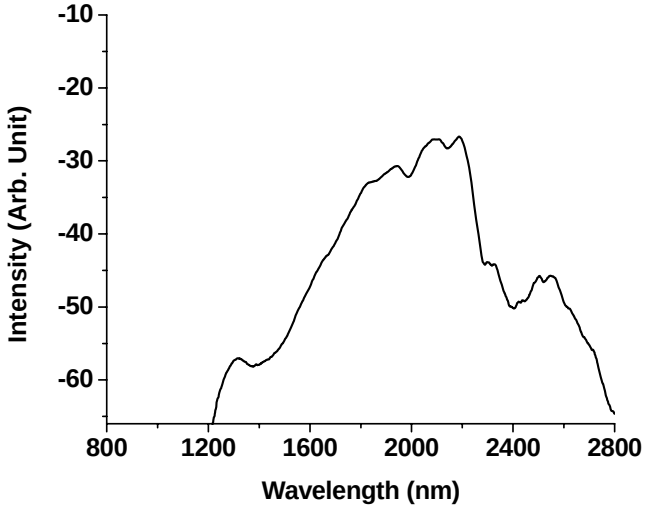

(b)

Fig. 5.2. Experimentally measured spectra for a 5cm sapphire fiber at two different input peak power levels of (a) 3.213×10^{6}W and (b) 1.607×10^{7}W.

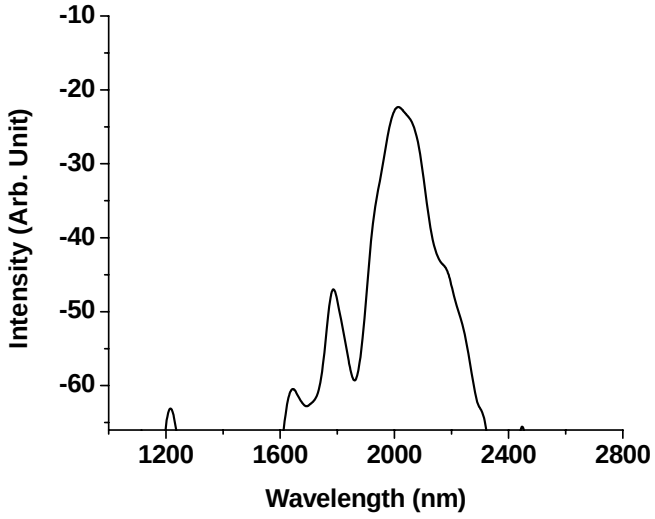

(a)

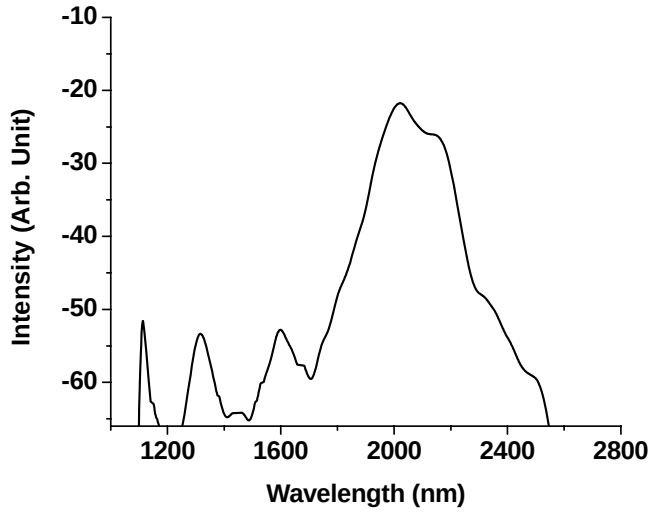

(b)

Fig. 5.3. Experimentally measured spectra for a 35cm sapphire fiber at two different input power levels of (a) 3.213×10^{6}W and (b) 1.607×10^{7}W.

5.4 - Simulations

To investigate the relevance of the experimental results, we performed the NLSE simulations with the parameters given in the previous sections and compared them with the experimental results. Simulations were performed for fiber lengths of 5cm and 35cm, the same lengths used in Figures 5.2 and 5.3, respectively, and an input peak power density level of 154.7 GW/cm^2 was employed. Parameters used for (2.40) and (2.41) are f_R=0.25 derived from equation given in [98] and according to n_2 and n_R given in [49], and τ_1=182fs and τ_2=200fs also given in [49]. Figure 5.4 compares the simulation results (dashed lines) to the experimental results (solid lines). Both the simulation and experimental results in Fig. 5.4(a) clearly show that when the fiber length is shorter than the dispersion length, 5cm in this case, the SCG in the sapphire fiber is mainly due to SPM. In Fig. 5.4(b), when the length of the sapphire fiber (35cm) is longer than the dispersion length, we observe the dispersive wave in both the simulated and experimental results. As shown in Figs. 5.4(a) and 5.4(b), the simulation results are in good agreement with experiments.

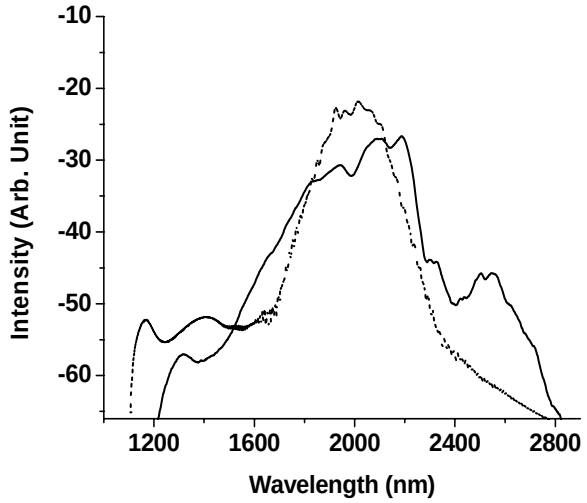

(a)

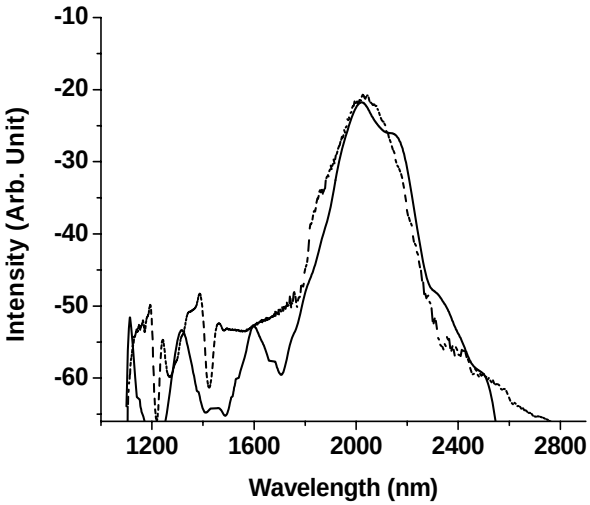

(b)

Figure 5.4. Spectra comparison between simulation and experimental results for (a) 5cm sapphire fiber and (b) 35cm sapphire fiber.

5.5 – Extension of Pumping Wavelength to Mid-IR region

As explained in Chapter 4 and earlier in this chapter, a silica-based fiber is not generally considered a good medium for generating supercontinuum in the mid-IR region (beyond 2.5μm) [32]. However, some papers mention that the SCG using silica-based fibers can indeed extend into mid-IR region. In [99], the authors use germano-silicate fibers to generate a supercontinuum that extends to the lower end of the mid-IR region (up to 2.8μm). UV light is shined onto a 1cm fiber to shift the zero dispersion point by over 100nm. However, a major disadvantage of using a silica-based fiber compared to a sapphire fiber is the heavier absorption in mid-IR region. Figure 5.5 shows transmission characteristics of silica and sapphire materials. As shown in Fig. 5.5, the absorption of silica in mid-IR region is much stronger than in sapphire. Therefore, supercontinuum generation beyond 2.8μm using a silica fiber is quite difficult, and fiber length must remain very short to avoid heavy absorption. To experimentally demonstrate the SCG using a sapphire fiber in mid-IR region, we shifted the wavelength of the OPA to 2.5μm, which is at a boundary between near- and mid-IR regions. We coupled the laser pulses into a 5cm sapphire fiber with input peak power density level of 92.82GW/cm^2. Figure 5.6 shows the experimentally measured spectra from the 5cm sapphire fiber pumped at 2.5μm. A spectrum from 2μm to 3.2μm was observed. This result experimentally proves that a SCG from sapphire fiber can extend further into the mid-IR than a SCG from a silica fiber.

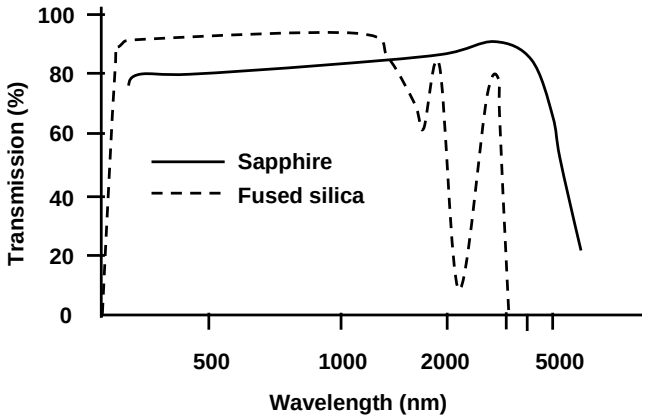

Figure 5.5. Transmission characteristics of silica and sapphire materials [100].

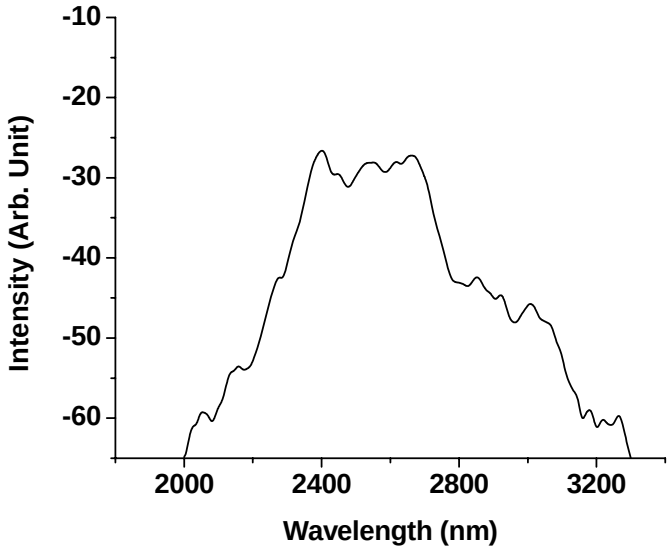

Figure 5.6. Experimentally measured spectra for a 5cm sapphire fiber at the wavelength of 2.5μm and input power level of 9.640×10^{6}W.

Chapter 6

Broadband supercontinuum generation covering UV to mid-IR region by using three pumping sources in single crystal sapphire fiber

6.1 – Motivation for Multiple Pumping Sources

Recently, the importance of a broadband light source covering UV through mid-IR has increased. In spectroscopy, many chemicals have distinct peaks in UV, visible, near-, mid-, and far-IR. However, the spectra of many chemicals can only be differentiated by a small number of peaks in a certain range. Thus, the scanning range needs to be as wide as possible to distinguish these small differences. Remote sensing applications would also benefit from a broadband light source. The system described in Reference [101] utilizes both UV and mid-IR optical sources generated by an optical parametric oscillator (OPO) to perform remote-sensing for environmental conditions such as air pollution and water vapor, and for terrestrial monitoring. As explained in previous chapters, even though conventional sources such as OPOs, tunable solid-state lasers, and quantum cascaded lasers (QCLs) can cover a wide spectral range by continuously tuning the wavelength [33], they cannot cover the entire range simultaneously because of the time delay during wavelength switching. Very wide range SCG from the UV to mid-IR (up to 4.5μm) in air has been previously reported [102]. However, this result was obtained in air by employing input pulses with an extremely high peak power density level on the order of a terawatt. Recently, broadband supercontinua from optical fibers covering more than an octave span have been demonstrated with relatively small intensity input pulses by many researchers [34, 35, 38]. Reference [35] shows that a SF-6 photonic

crystal fiber (PCF) with a very small mode area (2.6μm diameter) and a nonlinear refractive index of $2.2\times10^{-19}m^2/W$ can generate a spectrum that spans from 350nm to 3000nm. Compared to SF-6 fiber used in [35], the nonlinear refractive index of a sapphire fiber is comparable, but the nonlinear coefficient of a sapphire fiber (γ=1.171×10^{-5}/m·W at 1.55μm) is 14,000 times smaller than PCF fiber (γ=0.1680/m·W at 1.55μm) due to its large mode area (core diameter of 115μm). Although the large mode area of the sapphire fiber significantly reduces its nonlinear coefficient, SCG in fibers with a larger mode area has generated a great deal of interest for the following reasons [103-105]: the coupling efficiency is very high, and the chance of surface damage decreases since the input light does not have to be as tightly focused as in the case of PCF fiber [40]. To maintain the advantages of a large mode area sapphire fiber (i.e. high coupling efficiency, high damage threshold, and good IR transparency) while improving the supercontinuum bandwidth, we adopt a multiple pumping source scheme.

Previously, SCG using dual-wavelength pumping has been reported [106-110]. Dual-wavelength pumping broadens the spectrum via cross-phase modulation (XPM) [107, 109, 110], generates peaks at sidebands due to XPM-induced instability [106], and causes nondegenerate four-wave mixing (FWM) [108]. But, the broadened spectrum created by dual-wavelength pumping in many papers has a discontinuity between the supercontinua generated by each pump wavelength [106-109]. Even though these spectra are overlapped in several papers, the total reported span is much less than two octaves [110].

In this chapter, we employ triple pumping sources to generate supercontinuum in a single crystal sapphire fiber. Our supercontinuum covers a very broad spectrum from

the UV to the lower end of the mid-IR without spectra discontinuity. By using triple pumping sources, we can generate a very broad spectrum despite using a large mode area. Also, an even broader spectrum can be generated by increasing the number of pumping sources in the longer IR wavelengths.

6.2 - Technical approach

The generalized NLSE describing single pulse propagation (4.11) as shown in Chapter 4 is [83, 84]

$$\frac{\partial A}{\partial z}+\frac{\alpha}{2}A-\sum_{n\geq 2}\frac{i^{n+1}}{n!}\beta_n\frac{\partial^n A}{\partial T^n}=+i\gamma\left(1+\frac{i}{\omega_0}\frac{\partial}{\partial T}\right)A\cdot\int_{-\infty}^{+\infty}R(T')\left|A(z,T-T')\right|^2dT' \quad . \tag{6.1}$$

The nonlinear part of equation (6.1) can be expressed in terms of new variable V as [83, 84]:

$$\frac{\partial V}{\partial z}=i\gamma V\cdot R(T)*\left(\left|V_0\right|^2+\left|V\right|^2\right)-\gamma\frac{1}{\omega_0}\frac{\partial}{\partial T}\left(V\cdot R(T)*\left|V\right|^2\right) \quad , \tag{6.2}$$

$$\text{where } V(z,T)=A(z,T)\exp\left[i\gamma\left(R(T)*\left|A_0\right|^2\right)(z-z_0)\right] \quad . \tag{6.3}$$

In that case, the multiple pumping sources propagating in an optical fiber at the initial stage can be expressed as [111]:

$$V_0=\sum_{j=1}^{NP}P_j\exp\left[-\left(\frac{T}{T_0}\right)^2\right]\cdot\exp\left[i(\Delta\omega_j)T\right] \quad , \tag{6.4}$$

where NP is the total number of pumping sources, P_j and T_0 are peak power and pulse width of jth pumping source, and $\Delta\omega_j$ is frequency difference between the jth pumping source and the carrier beam (NP=3 for our case). Each beam has high peak intensity on the order of 10^7 W, and three combined intensity carried through the fiber is very high.

Thus, a sapphire fiber, which exhibits a high damage threshold, is a suitable optical medium for the propagation of three high power pulses simultaneously. In our experiments, we used a highly multimode sapphire fiber with a core diameter of 115μm. An optical parametric amplifier (OPA) produces signal and idler beams and an additional pumping source at 784nm according to the equation of $\omega_{784nm}=\omega_{signal}+\omega_{idler}$. We have chosen the pumping sources at 784nm, 1290nm, and 2000nm to minimize intensity fluctuation in the overlapping region of each spectrum. The dispersion parameters in sapphire fiber at 784nm (-187.4ps/nm-km) and 1290nm (-3.374ps/nm-km) are within normal dispersion while the 2000nm pulse (57.28ps/nm-km) lies in anomalous dispersion. To determine the length of a sapphire fiber, the dispersion length, L_D, and the nonlinear interaction length, L_{NL}, need to be calculated. Those lengths are given as $L_D=T_0^2/|\beta_2|$ and $L_{NL}=1/\gamma P_0$, where P_0 is the peak power of the propagating beam, and β_2 is group velocity dispersion [61]. The group velocity dispersion at 784nm, 1290nm, and 2000nm can be calculated from $\beta_2=(\lambda^3/2\pi c^2)\cdot(d^2n_0/d\lambda^2)$, and the calculated values are 59.21ps^2/km, 2.979ps^2/km, and -121.5ps^2/km, respectively. Based on pulse width of 150fs, the dispersion lengths are 38.01cm for 784nm, 755.34cm for 1290nm, and 18.52 cm for 2000nm. The effective mode area A_{eff} (10,386μm^2) and the nonlinear refractive index n_2 (3×10^{-20}m^2/W for 784nm, 2.9×10^{-20}m^2/W for 1290nm, and 2.8×10^{-20}m^2/W for 2000nm [42]) are substituted into $\gamma=n_2\omega_0/cA_{eff}=2\pi n_2/\lambda A_{eff}$ to find the nonlinear coefficients. The calculated values are 2.268×10^{-5}/m·W, 1.359×10^{-5}/m·W, and 8.466×10^{-6}/m·W for 784nm, 1290nm, and 2000nm, respectively. The calculated nonlinear interaction lengths according to the nonlinear coefficient above and the estimated peak power for our

experiment (approximately 1.607×10^{7}W) are 0.274cm for 784nm, 0.457cm for 1290nm, and 0.735cm for 2000nm.

To minimize the dispersion-related interaction, we used a fiber length of 5cm, which is larger than calculated nonlinear interaction lengths, but smaller than dispersion lengths. The shape of the overall spectral broadening due to the propagation of three pumping sources can be predicted by the superposition of the supercontinuum generated by each of the sources individually. Also, a notable effect of the nondegenerate FWM that results from the interaction between two pumping sources can enhance the spectral broadening and increase the intensity level. The equations for the frequency (ω) and phase matching (k) conditions are as follows [112]:

$$\omega_{P1} + \omega_{P2} = \omega_{s1} + \omega_{i1}$$

$$\omega_{P1} + \omega_{P3} = \omega_{s2} + \omega_{i2}$$

$$\omega_{P2} + \omega_{P3} = \omega_{s3} + \omega_{i3} \quad , \tag{6.5a}$$

$$k_{P1} + k_{P2} = k_{s1} + k_{i1} + \gamma_{P1}P_{P1} + \gamma_{P2}P_{P2}$$

$$k_{P1} + k_{P3} = k_{s2} + k_{i2} + \gamma_{P1}P_{P1} + \gamma_{P3}P_{P3}$$

$$k_{P2} + k_{P3} = k_{s3} + k_{i3} + \gamma_{P2}P_{P2} + \gamma_{P3}P_{P3}\,, \tag{6.5b}$$

where p_j is j^{th} pumping source, s_j and i_j are signal and idler beams generated by the FWM processes, and γ_{pj} and P_{pj} are the nonlinear coefficient and the peak power of j^{th} pumping source.

6.3 - Experimental procedures and results

To verify that FWM processes are involved in the SCG from three pumping sources, we calculated the frequency interaction and phase matching conditions of the three pumping sources. The frequency interaction condition between 1290nm and 2000nm is given as:

$$\omega_{1290nm} + \omega_{2000nm} = \omega_{s3} + \omega_{i3}, \tag{6.6}$$

which is only satisfied when the following phase matching condition is matched [112]:

$$k_{1290nm} + k_{2000nm} = k_{s3} + k_{i3} + (\gamma P)_{1290nm} + (\gamma P)_{2000nm}, \tag{6.7}$$

where $k_\lambda = 2\pi n_\lambda / \lambda$. By using the nonlinear coefficients, the peak power of 1.607×10^7W, and the refractive indices derived from the sellmeier equation [51, 53] to solve the phase matching condition, we find that the phase matching condition occurs when the signal and idler beams are at 1164nm and 2400nm. Also, two other interactions (784nm and 1290nm, and 784nm and 2000nm) generate the signal and idler peaks located at 595nm and 2700nm, and 727nm and 2500nm, respectively.

To compare the validity of our theory with the experimental results, three pumping sources were launched into the sapphire fiber. For the experimental setup shown in Fig. 6.1, the three sources were the signal and idler beams (1290nm and 2000nm) from the OPA and an additional source at 784nm. The beams have a 1kHz repetition rate and 150fs pulse width. Three beams were focused by a parabolic mirror and coupled into the 5cm sapphire fiber. The supercontinuum generated through the sapphire fiber was collimated by a silica lens (for UV, visible, and near-IR ranges) and a Zinc Selenide (ZnSe) IR lens (for near- and mid-IR ranges), and was detected by a monochromator (MicroHR, Horiba Jobin Yvon Inc.).

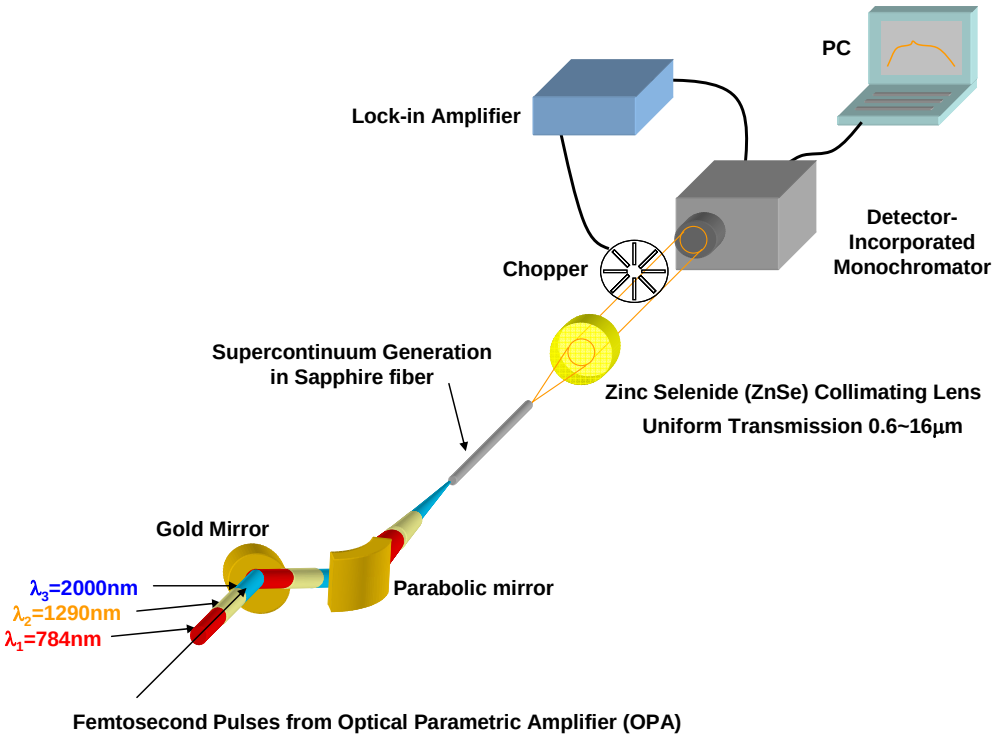

(a)

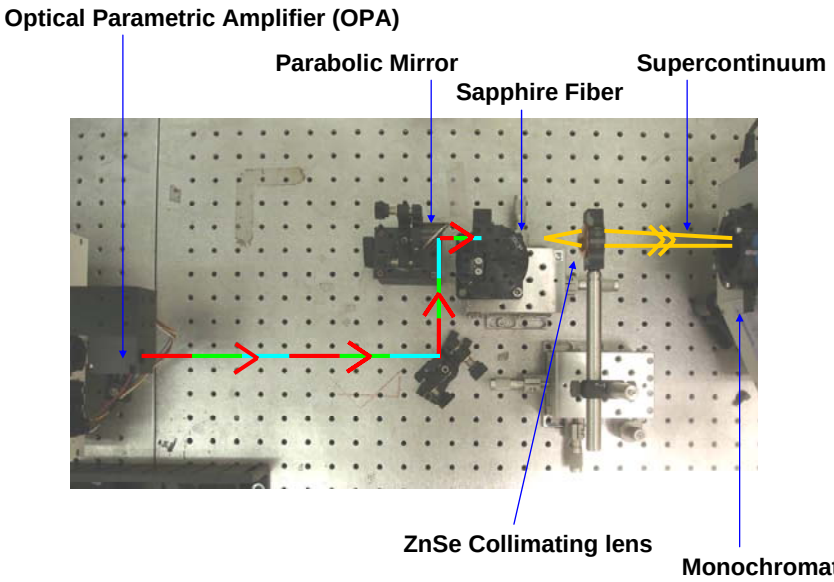

(b)

Fig. 6.1. Experimental set up for supercontinuum generation in sapphire fiber: (a) configuration, (b) picture.

Figure 6.2 shows the experimental results of the supercontinuum spectra generated from the three individual pumping sources (blue dash: 784nm, green dash: 1290nm, and black dash: 2000nm) and the three pumping sources together (red solid). The spectrum produced by each individual pumping source is primarily a result of SPM. The spectra from the 784nm, 1290nm, and 2000nm sources range from 400nm to 1200nm, from 1000nm to 1800nm, and 1300nm to 2800nm, respectively. The supercontinuum generated by the three pumping sources together involves more than SPM. The three main spectra due to SPM are overlapped while the peaks due to nondegenerate FWM processes are created when the pulses from the three sources travel through the sapphire fiber simultaneously. The peaks created by FWM also undergo degenerate FWM processes with other peaks [113] to stack multiple peaks in the UV area, but the later interactions occur over a very short distance due to walk-off. Other effects such as Raman scattering and XPM also contribute to the increase in both ends of spectra. Therefore, idler beams can enhance the intensity level in mid-IR region via nondegenerate FWM processes while signal beams involved in nondegenerate and degenerate FWM processes can increase the intensity level in the UV and visible regions. As a result, an ultra-broadband supercontinuum ranging from the UV to mid-IR regions is generated by employing three pumping sources. The calculated peaks due to nondegenerate FWM processes match well with those of the experimental spectra shown in Fig. 6.2.

To verify the relevance of our experimental results, a simulation of the NLSE was performed with the same parameters as the experiments. We followed similar procedures in [83, 84] to numerically simulate the SCG in a sapphire fiber due to the

propagation of three pumping sources. Figure 6.3 shows the simulated spectra of the supercontinuum emitted from the sapphire fiber due to the interaction of the three pumping sources. The spectra of three pumping sources are broadened by SPM and overlapped while peaks and intensity enhancement in the UV, visible, and mid-IR are observed due to complex FWM processes. The peaks due to nondegenerate FWM processes in the simulation results are in good agreement with the experimental results.

To check whether the peaks shown in Figs. 6.2 and 6.3 are the nondegenerate FWM caused by each interaction between two pumping sources, we evaluated the interaction between 1290nm and 2000nm with simulation and experimental results. Figure 6.4(a) shows the simulation spectrum caused by the interaction between 1290nm and 2000nm pumping sources. The peak powers of 8.035×10^{6}W and 4.821×10^{6}W are utilized for 1290nm and 2000nm peaks, respectively. As shown in Fig. 6.4(a), signal and idler peaks due to the FWM are observed. To verify that the peaks observed in Fig. 6.4(a) are due to the FWM, we increased the peak power of 1290nm pumping source to 1.286×10^{7}W while the peak power for 2000nm source is unchanged. As shown in Fig. 6.4(b), the main spectrum caused by 2000nm source is very similar to that in Fig. 4(a) while the intensities of both peaks due to the FWM are increased. Figure 6.4(c) shows three simulation spectra when 2000nm pumping source is presented alone (dot line), and it is accompanied by 1290nm source with the peak powers of 8.035×10^{6}W (dashed line) and 1.286×10^{7}W (solid line). While the spectra due to 2000nm pumping source remains very similar, the peak at 2400nm intensifies when the intensity of 1290nm source increases. Also, the peak at 2400nm is not ovservable when 1290nm source is not coupled together. This seems to be due to the increased FWM gain [114]. According to

papers that discuss cross-phase modulation (XPM) effect caused by dual-pumping, the spectrum of an interested source dramatically expands in wavelength when it is affected by another pumping source at different wavelength [107, 110, 115]. Therefore, compared to the FWM, the XPM effect does not seem very dominant in this simulation. To verify our simulation results shown in Fig. 4(a)-(c), we experimentally evaluated two pumping sources of 1290nm and 2000nm. The peak power used for this experiment was 8.035×10^{6}W. As shown in Fig. 6.4(d), two peaks due to the FWM are clearly observable. Therefore, many peaks appearing on Figs. 6.3 and 6.4 seem to be caused by the FWM effect.

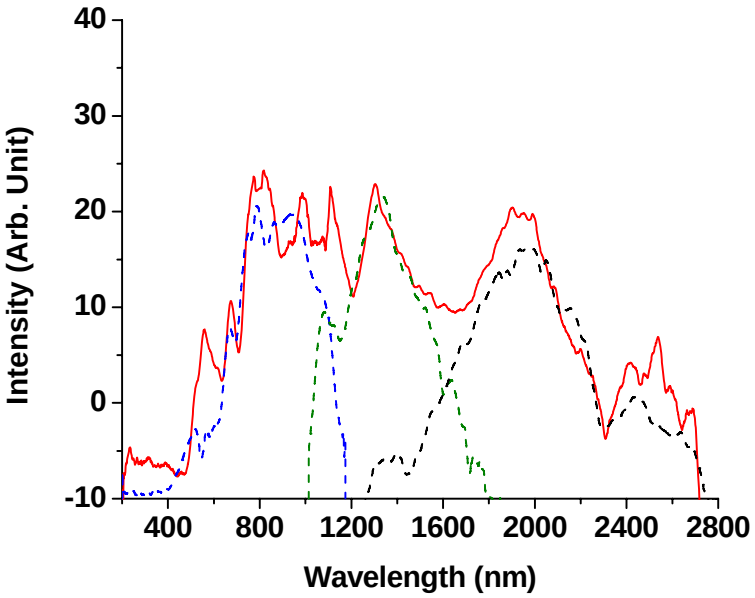

Fig. 6.2. The experimentally measured spectra generated from the three individual pumping sources (blue dash: 784nm, green dash: 1290nm, and black dash: 2000nm) and the three pumping sources together (red solid)

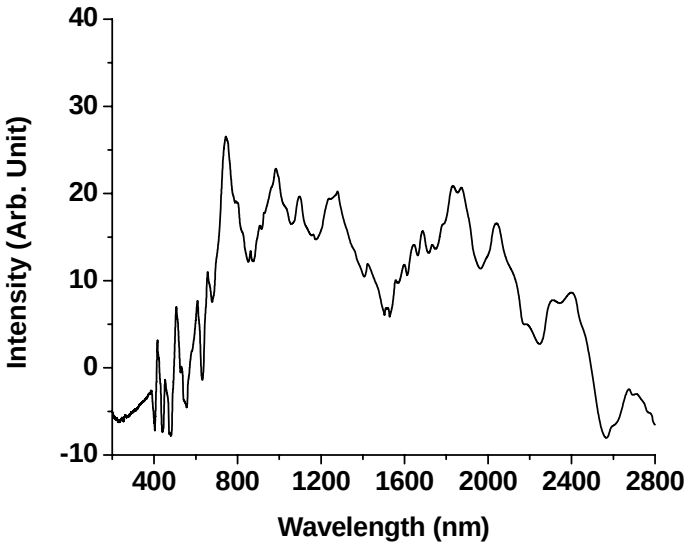

Fig. 6.3. The simulation spectra generated from the three pumping sources

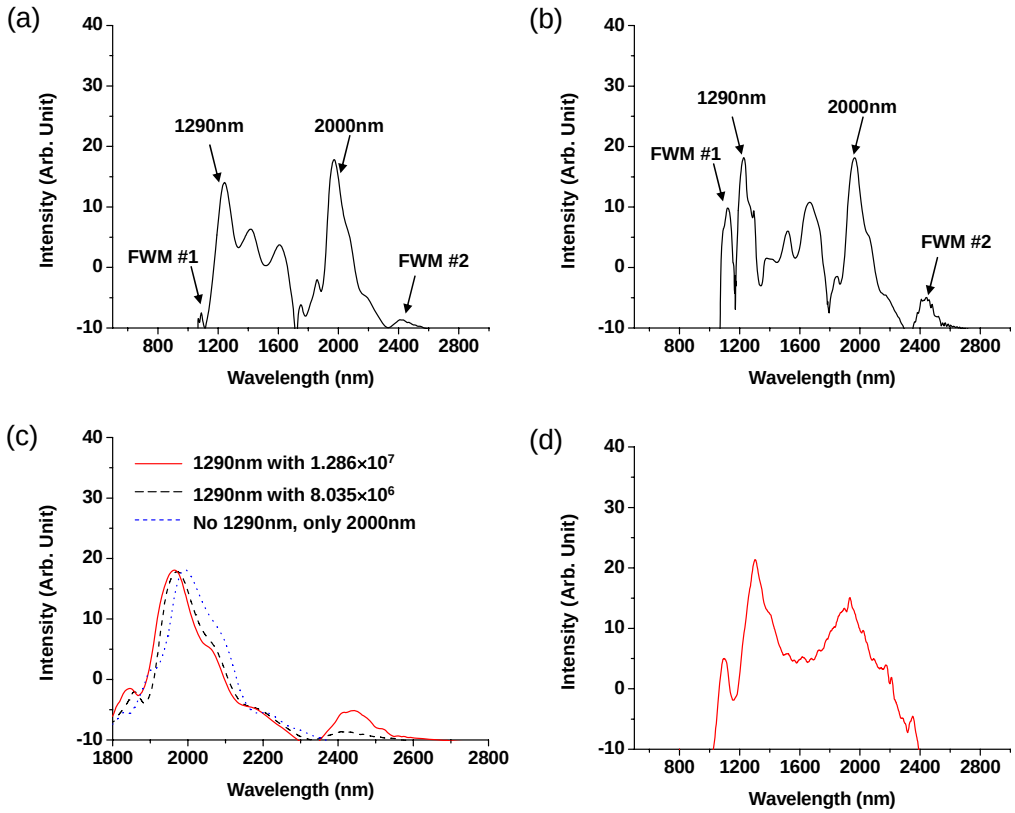

Fig. 6.4. The simulation and experimental spectra of two pumping sources located at 1290nm and 2000nm: (a) simulation spectra of 1290nm source with 8.035×10^{6}W and 2000nm source with 4.821×10^{6}W, (b) simulation spectra of 1290nm source with 1.286×10^{7}W and 2000nm source with 4.821×10^{6}W, (c) three simulation spectra when 2000nm pumping source is presented alone (dot line), and it is accompanied by 1290nm source with the peak powers of 8.035×10^{6}W (dashed line) and 1.286×10^{7}W (solid line), and (d) experimental spectra of 1290nm and 2000nm sources with the peak power of 8.035×10^{6}W.

Chapter 7

Applications

Recently, the importance of a broadband light source has increased for the IR spectroscopy application. Absorption IR spectroscopic method by using tunable diode lasers has been reported for many applications including combustion, pollutant, and process monitoring [116-118]. However, as explained in previous chapters, tunable laser sources, OPOs, and QCLs cannot cover the entire spectrum range simultaneously because of the time delay during wavelength switching. As an example, timescale required for absorption spectroscopic method employed in turbulent combustion processes is from microseconds to milliseconds, which is not easily obtainable by wavelength-tuning devices [119]. Also, as explained in Chapter 6, in spectroscopy, many chemicals have distinct peaks in UV, visible, near-, mid-, and far-IR. However, the spectra of many chemicals can only be differentiated by a small number of peaks in a certain range. Thus, the scanning range needs to be as wide as possible to distinguish these small differences.

Remote sensing applications would also benefit from a broadband light source. The system described in Reference [8] utilizes both UV and mid-IR optical sources generated by an optical parametric oscillator (OPO) to perform remote-sensing for environmental conditions such as air pollution and water vapor, and for terrestrial monitoring.

To satisfy simultaneous measurement and broadband requirements, in this chapter, we use supercontinuum source to perform IR absorption spectroscopy. Also, demonstration of possibility for remote sensing application using our supercontinuum

source is performed.

7.1 IR Absorption Spectroscopy

To observe near-IR spectrum of various chemicals, a conventional fiber (SMF-28e) was pumped by a femtosecond laser, which had repetition rate of 1kHz, center wavelength of 784nm, and pulse width of 150fs. Figure 7.1 shows the experimental setup for IR absorption spectroscopy. Generated supercontinuum from the fiber was collimated and passed into a glass container with the path length of 8mm. The supercontinuum source absorbed by chemical inside the glass container was focused and coupled into a multimode fiber, whose end is connected to an OSA (HP70951B).

Chemicals tested were pseudo-TNT (2,4,6-trinitrotoluene), pseudo-RDX (1,3,5-trinitroperhydro-1,3,5-triazine), pseudo-HMX (1,3,5,7-tetranitroperhydro-1,3,5,7-tetrazocine), and pseudo-PETN (pentaerythritol tetranitrate), which are properly mixed with Methanol and Acetonitrile to produce very similar spectra compared to real composition while safety for storage and handling is ensured. First, spectrum of pseudo-TNT composed of 0.01% TNT, 50.00% Methanol, and 49.99% Acetonitrile was obtained using the supercontinuum source generated by the 784nm femtosecond laser as shown in Fig. 7.2. The spectra range obtained was from 1000nm to 1700nm (from 10000cm^{-1} to 5882cm^{-1} in wavenumber) limited by the range of the OSA. Figure 3 shows the absorption spectra obtained by using a Perkin Elmer 1700 Fourier transform infrared spectroscopy (FTIR) instrument. As shown in Figs. 7.2 and 7.3, spectra in both results are in good agreement.

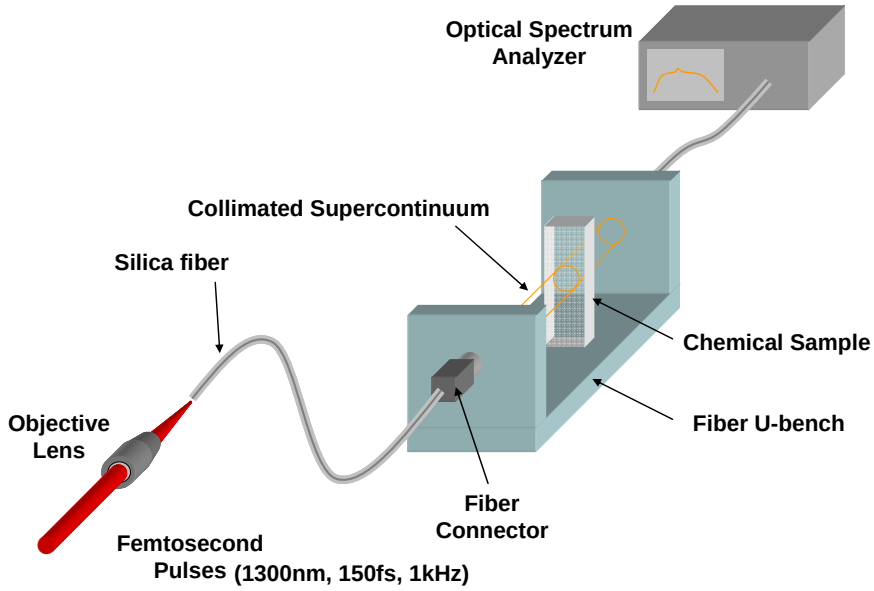

(a)

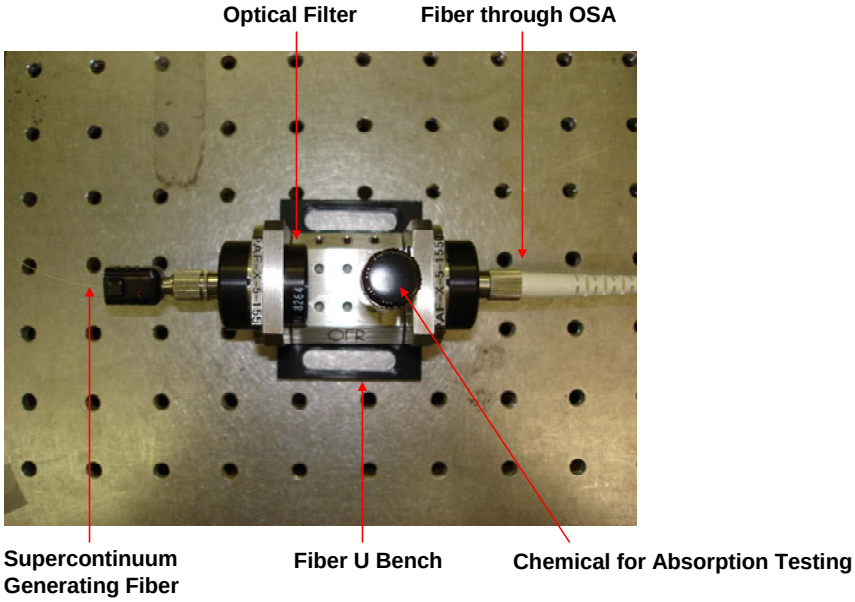

(b)

Fig. 7.1. Experimental setup for near-IR absorption spectroscopy: (a) configuration, (b) picture.

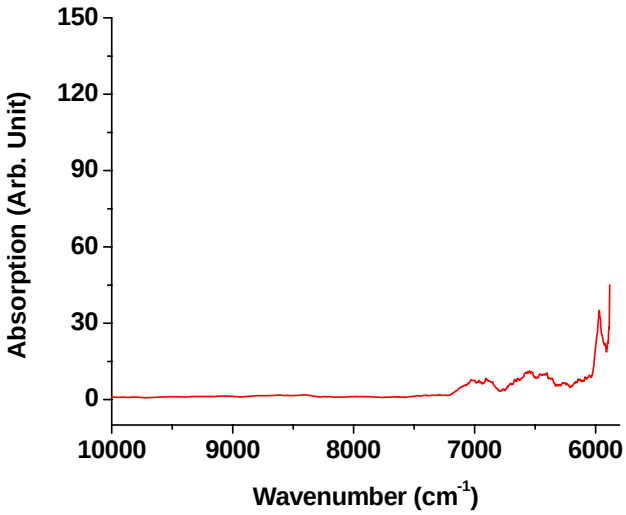

Fig. 7.2. Experimentally measured spectra of pseudo-TNT chemical by performing absorption spectroscopy using our own supercontinuum source.

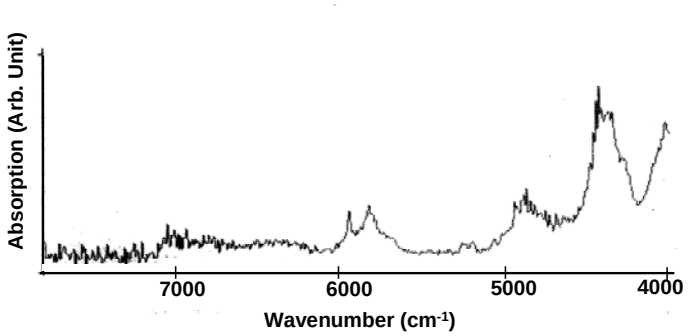

Fig. 7.3. Experimentally measured spectra of pseudo-TNT using FTIR.

Pseudo-RDX (0.01% RDX, 50.00% Acetonitrile, and 49.99% Methanol), pseudo-PETN (0.01% PETN and 99.9% Methanol), and pseudo-HMX (0.01% HMX, 49.99% Methanol, and 49.99% Acetonitrile) were also measured using the same methods

as pseudo-TNT. The spectra measured are shown in from Fig. 7.4 to Fig. 7.9. All the results measured using our own source matched well with the spectra obtained by using the FTIR. FTIR, similar to OPOs and QCLs, is also inherent to time delay due to wavelength switching caused by the movement of interferometric optics. Therefore, a supercontinuum source is promising technology for the applications of spectroscopy without time delay while it produces coinciding results with them obtained by a FTIR.

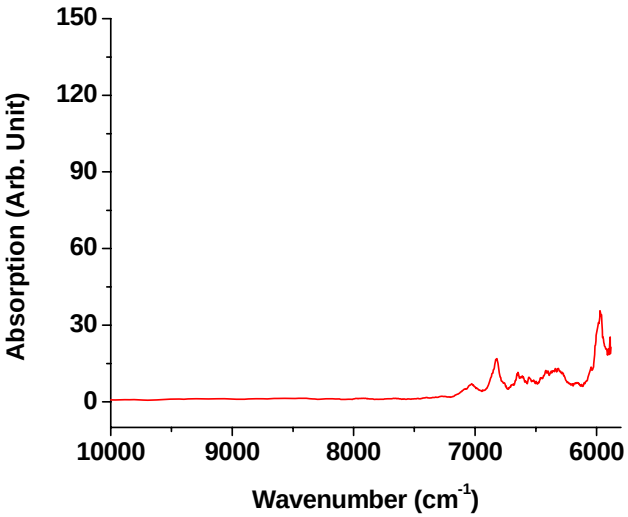

Fig. 7.4. Experimentally measured spectra of pseudo-RDX chemical by performing absorption spectroscopy using our own supercontinuum source.

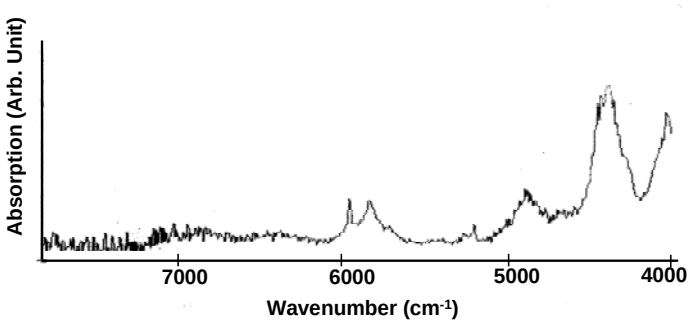

Fig. 7.5. Experimentally measured spectra of pseudo-RDX using FTIR.

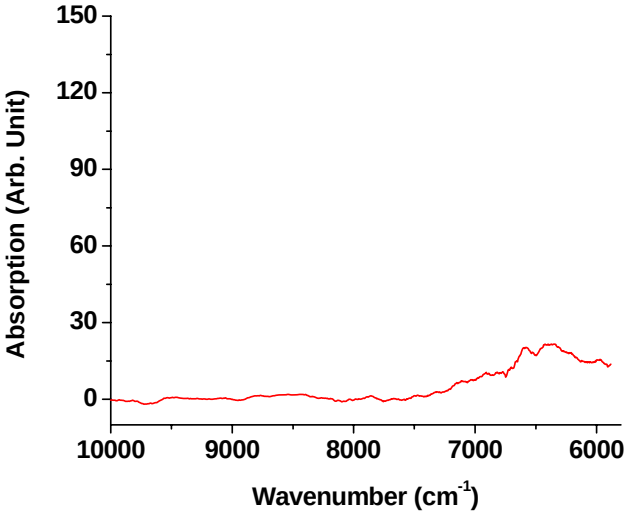

Fig. 7.6. Experimentally measured spectra of pseudo-PETN chemical by performing absorption spectroscopy using our own supercontinuum source.

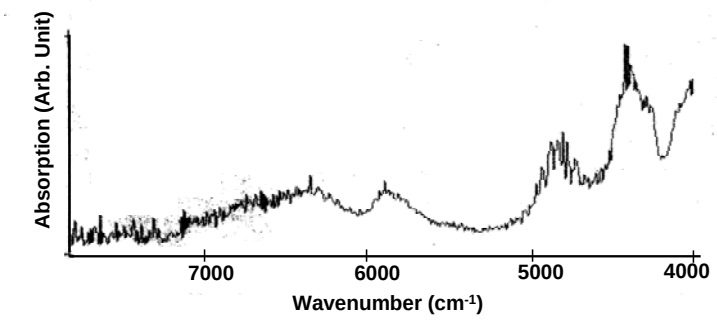

Fig. 7.7. Experimentally measured spectra of pseudo-PETN using FTIR.

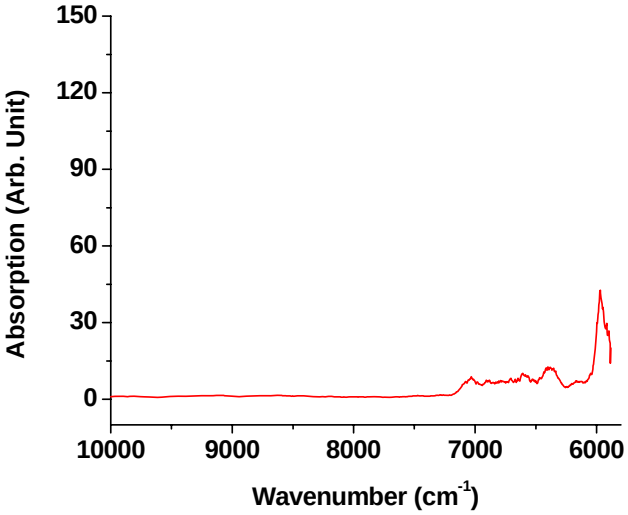

Fig. 7.8. Experimentally measured spectra of pseudo-HMX chemical by performing absorption spectroscopy using our own supercontinuum source.

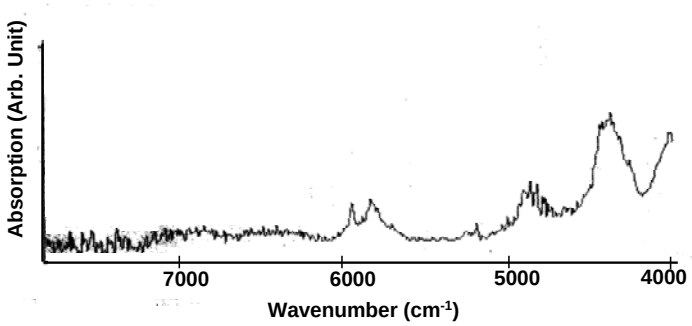

Fig. 7.9. Experimentally measured spectra of pseudo-HMX using FTIR.

As shown in previous results, measurements of absorption spectroscopy were only performed in near-IR region from 1000nm to 1700nm (from 10000cm^{-1} to 5882cm^{-1} in wavenumber) due to the limitation of light sources and measurement instruments. Since the center wavelength of femtosecond pulses is quite deviated from mid-IR region, and the OSA has measurement range only from 600nm to 1700nm, realization of IR

absorption spectroscopy beyond the OSA range is quite difficult. To solve the limitation enforced by femtosecond pulses with the center wavelength of 784nm, an OPA is utilized. By using the OPA, the center wavelength of femtosecond pulses is shifted to 2μm. Since silica-material fibers have high absorption beyond 2.5μm, a single crystal sapphire fiber with good transmission capability up to 5μm is utilized. Also, to overcome the measurement disability of the OSA, a monochromator (Horiba Jobin Yvon, Micro-HR) with measurement ability up to 5μm is employed.

The experimental setup for absorption spectroscopy is shown in Fig. 7.10. First, we generated supercontinuum by pumping a 5cm sapphire fiber using 2μm femtosecond pulses, which were generated from the OPA. The output beam out of the sapphire fiber was collimated into 5mm diameter using a ZnSe lens, passed through an 1mm spectrophotometer cell (transmission range from 300nm to 2500nm), then coupled into a detector-incorporated monochromator. Both optical beams for the first and second scans traveled into the 1mm spectrophotometer cell, but first and second scans were performed without and with chemical in the spectrophotometer cell, respectively. To find the absorption spectrum of the chemical, the second scan was subtracted from the first scan. Figures 7.11(a) and 7.11(b) show the experimentally measured spectra into the glass cuvette with and without the pseudo-TNT chemical, and the absorption spectrum of the pseudo-TNT, which is the difference between two measured spectra, respectively. The spectrum obtained using our supercontinuum source coincides well with the results shown in Fig. 7.3.

The sample of pseudo-TNT was replaced with pseudo-RDX, pseudo-PETN, and pseudo-HMX, and spectra were measured as shown from Fig 7.12 to Fig. 7.14. All the

results measured using our own source matched well with the spectra obtained by using the FTIR.

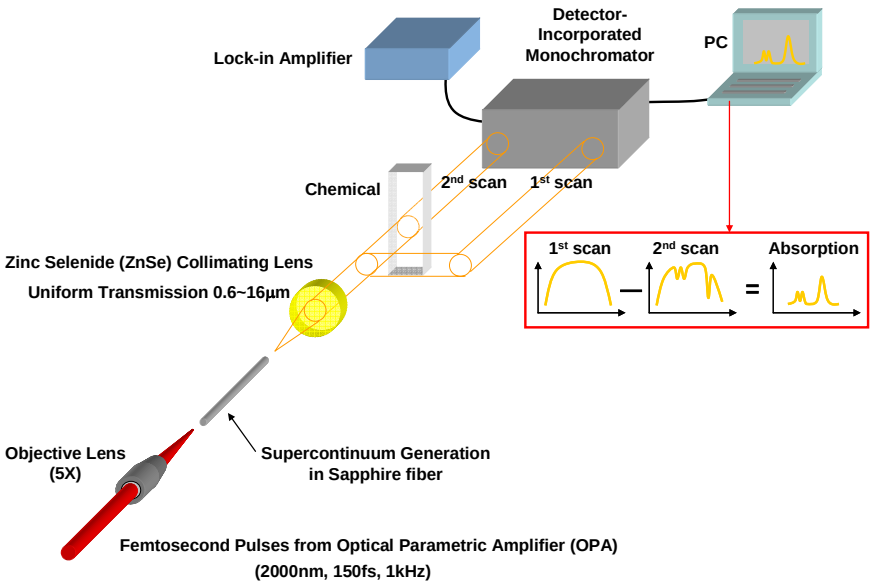

(a)

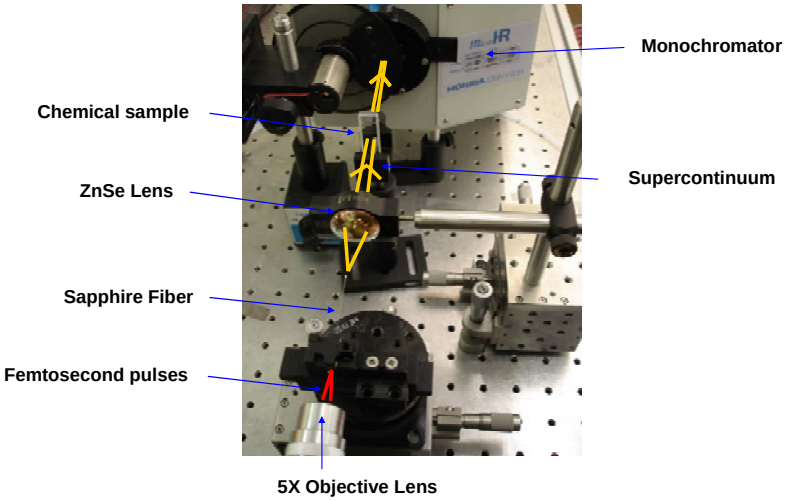

(b)

Fig. 7.10. Experimental set up for absorption spectroscopy beyond OSA range: (a) configuration, (b) picture.

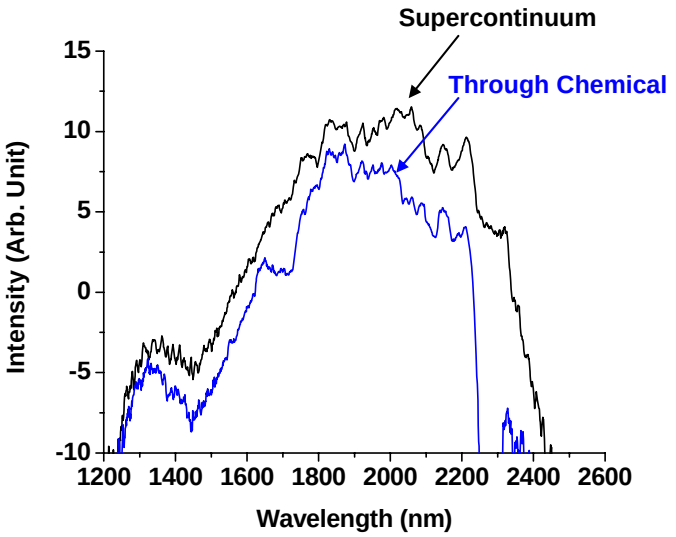

(a)

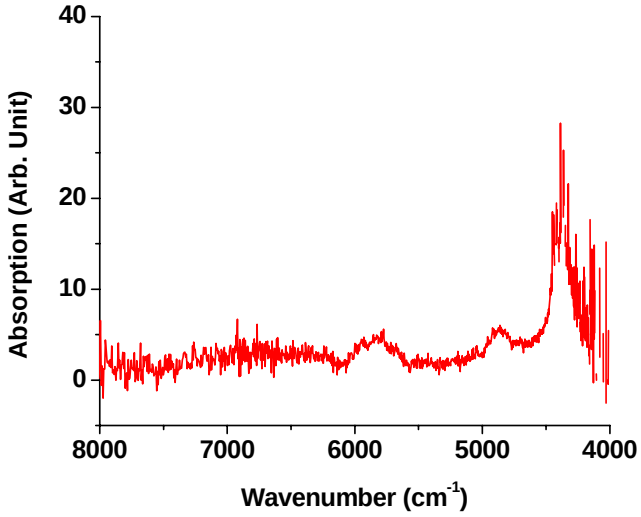

(b)

Fig. 7.11. Experimentally measured spectra of pseudo-TNT chemical by performing absorption spectroscopy using our own supercontinuum source: (a) spectra with and without the chemical and (b) absorption spectrum of pseudo-TNT chemical.

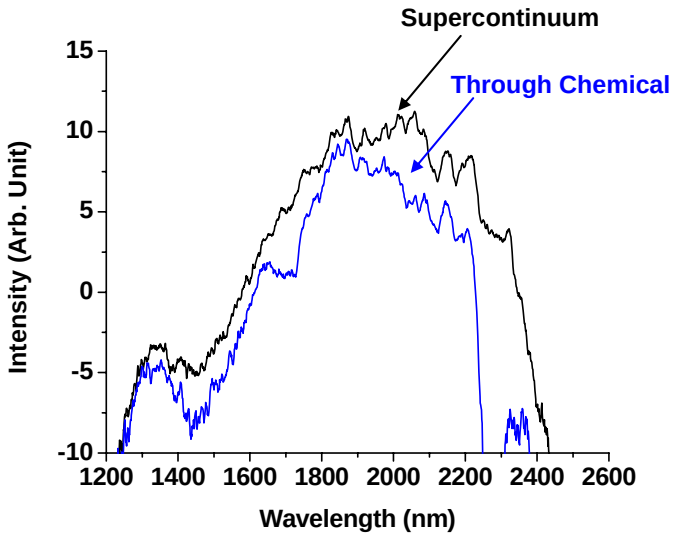

(a)

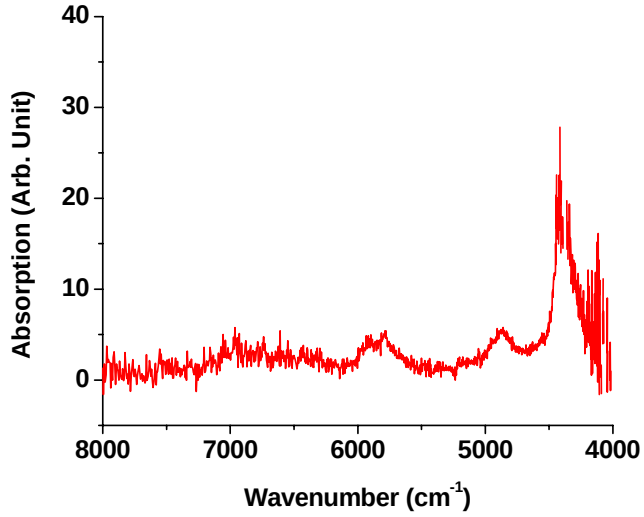

(b)

Fig. 7.12. Experimentally measured spectra of pseudo-RDX chemical by performing absorption spectroscopy using our own supercontinuum source: (a) spectra with and without the chemical and (b) absorption spectrum of pseudo-RDX chemical.

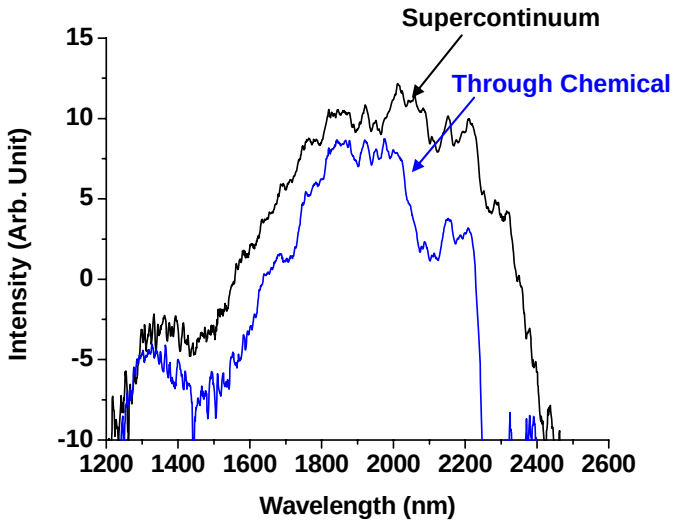

(a)

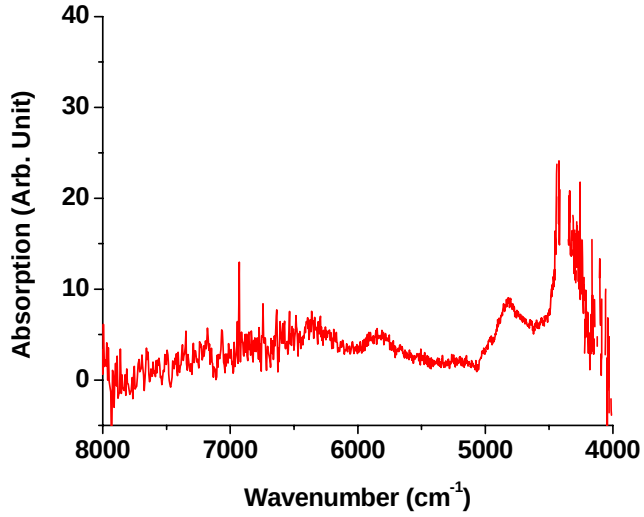

(b)

Fig. 7.13. Experimentally measured spectra of pseudo-PETN chemical by performing absorption spectroscopy using our own supercontinuum source: (a) spectra with and without the chemical and (b) absorption spectrum of pseudo-PETN chemical.

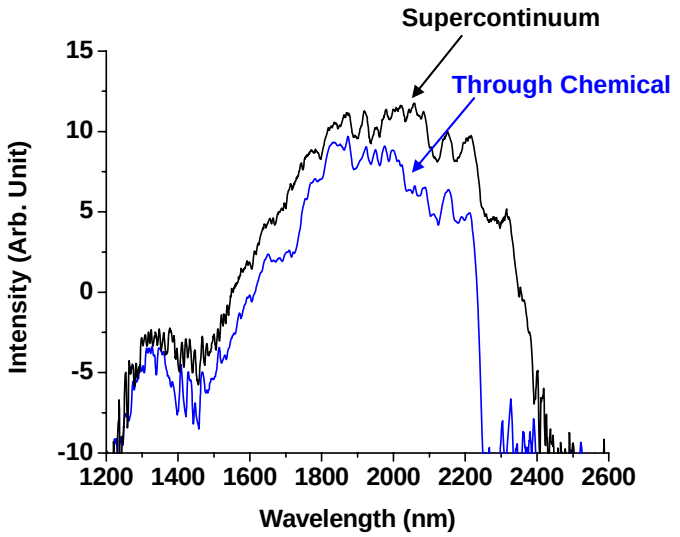

(a)

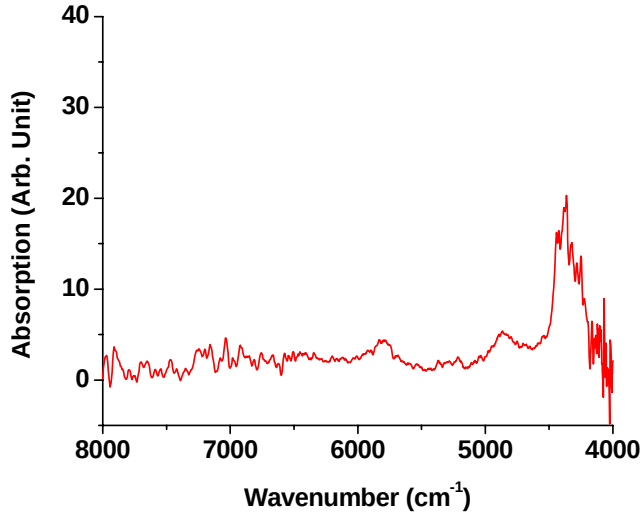

(b)

Fig. 7.14. Experimentally measured spectra of pseudo-HMX chemical by performing absorption spectroscopy using our own supercontinuum source: (a) spectra with and without the chemical and (b) absorption spectrum of pseudo-HMX chemical.

7.2 Supercontinuum for Remote Sensing Application

Supercontinuum source is known as spatially coherent. Therefore, it has possibility to travel long distance without losing its collimation. To verify the remote sensing ability of our supercontinuum generated in sapphire fibers, collimation ability of our supercontinuum source was tested. The generated supercontinuum was collimated using a regular fused-silica lens, and passed into folded mirror system, which had the total traveling distance of 16m in return as shown in Fig. 7.15 (a) and (b). After the collimated beam traveled 16m, the beam quality was tested. The initial beam diameter of 8mm remained the same through 16m. However, color distribution of beam was changed as shown in Fig. 7.16. This seems to be due to chromatic aberrations of the regular silica-fused lens. Thin-lens equation can be expressed as [120]

$$\frac{1}{f} = (n_l - 1)\left(\frac{1}{R_1} - \frac{1}{R_2}\right) \quad , \tag{7.11}$$

where n_l, R_1, and R_2 are wavelengths, front and back radii, respectively. According to (7.11), the focal length is dependent of wavelengths, which is not suitable for the collimation of a broadband source.

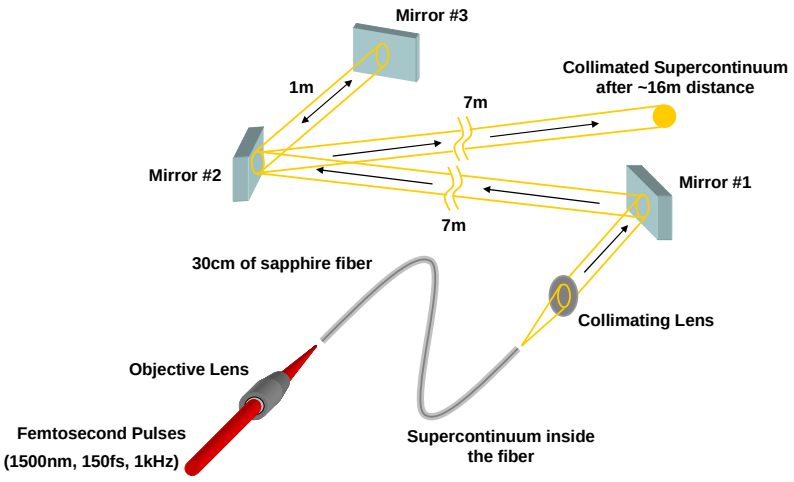

(a)

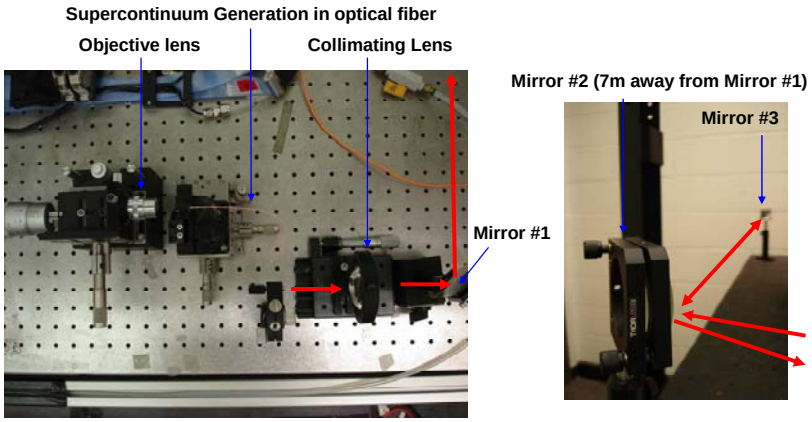

(b)

Fig. 7.15. Experimental setup for long-distance collimation: (a) configuration, (b) pictures

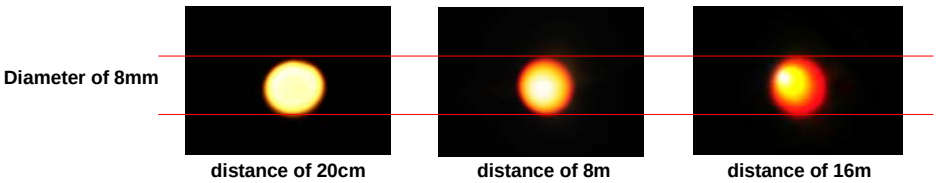

Fig. 7.16. Beam distributions of collimated beam after certain distances.

To overcome the chromatic aberrations caused by the regular lens, a parabolic mirror, which greatly reduces the wavelength dependence of broadband source, is employed. Also, IR absorption spectroscopy after long distance with various chemicals (pseudo-PETN, pseudo-TNT, and pseudo-HMX) was performed. To obtain a beam with broad spectrum, scheme of two pumping sources (1290nm and 2000nm) was employed to generate supercontinuum in a sapphire fiber. As shown in Fig. 7.17, the generated supercontinuum was collimated by a parabolic mirror, and coupled into a folded mirrors system, which had the total traveling length of 16m. The beam after the traveling length of 16m went through a sample, was scatterred by a metallic sufrace, was collected using telescope lens, and measured by a monochromator. The pure supercontinuum spectrum acquired after the traveling length of 16m is shown in Fig. 7.18.

Figures 7.19-7.21 show the absorption spectra of the pseudo-TNT, pseudo-PETN, and pseudo-HMX. The various peaks in the spectra obtained using our supercontinuum sources are identical to the results obtained by the FTIR.

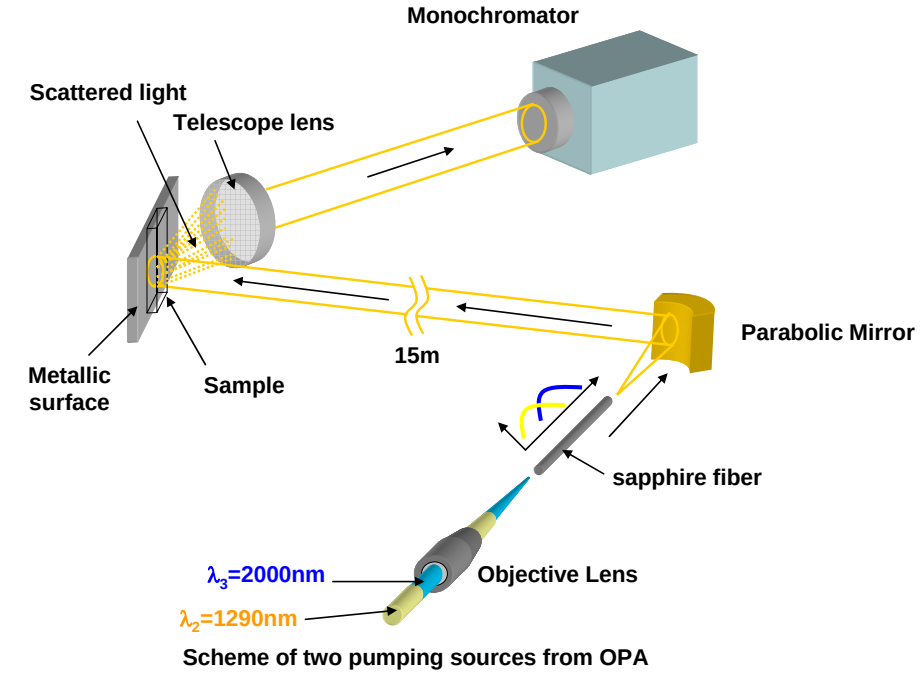

(a)

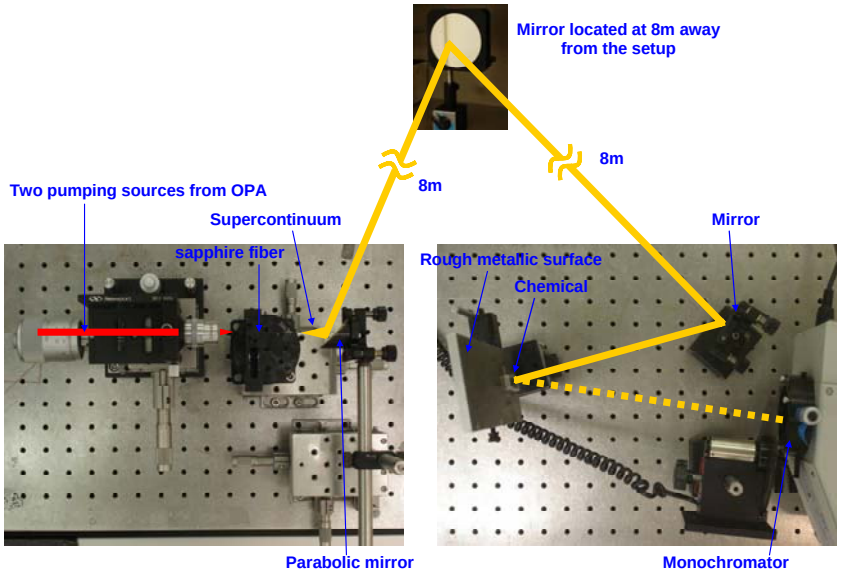

(b)

Fig. 7.17. Experimental setup for long distance spectroscopy: (a) configuration, (b) pictures.

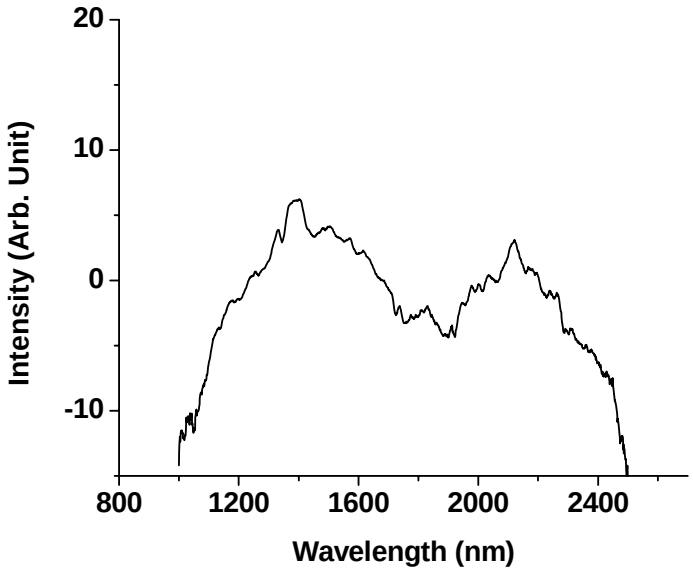

Fig. 7.18. Measured supercontinuum (generated by the scheme of two pumping sources) after the traveling length of 16m and scattered by rough metal surface.

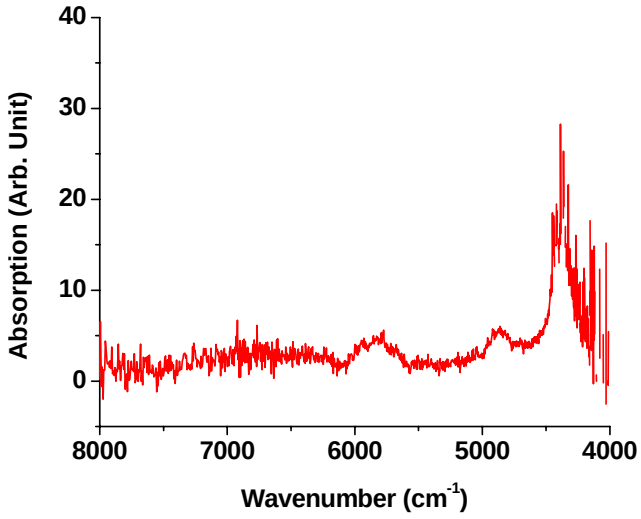

Fig. 7.19. Experimentally measured absorption spectrum of pseudo-TNT chemical by performing absorption spectroscopy using our own supercontinuum source.

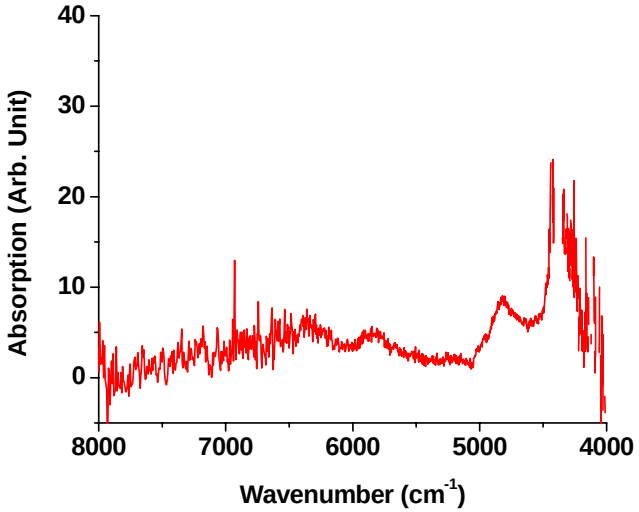

Fig. 7.20. Experimentally measured absorption spectrum of pseudo-PETN chemical by performing absorption spectroscopy using our own supercontinuum source.

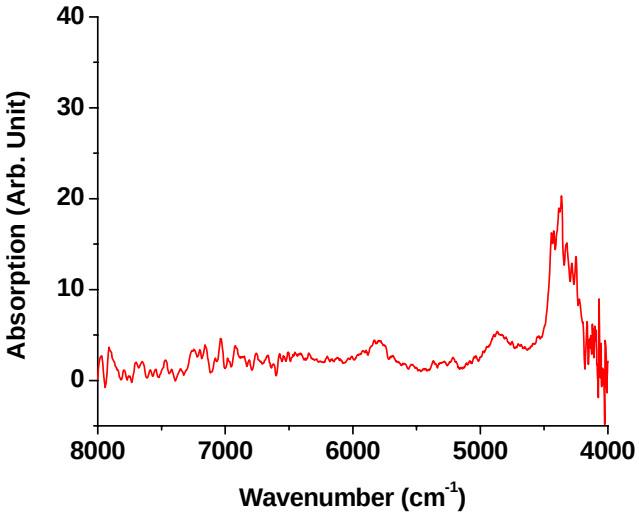

Fig. 7.21. Experimentally measured absorption spectrum of pseudo-PETN chemical by performing absorption spectroscopy using our own supercontinuum source.

Chapter 8

Conclusions and Future Works

In this dissertation, supercontinuum generations in sapphire fibers under various conditions were investigated, and their corresponding effects were analyzed. Main motivation to use sapphire fibers as optical media for supercontinuum generation was that they had the characteristics of good transparency in mid-IR, high laser damage threshold, and high melting temperature compared to conventionally utilized fibers including silica-based fibers and infrared fibers.

Even though single crystal sapphire fiber satisfies many conditions as an optical medium to generate supercontinuum (good transparency in wide wavelength region, similar nonlinearity compared to a silica-based fiber, high damage threshold, and high melting temperature), only several papers report supercontinuum generation in the form of sapphire bulks, not sapphire fibers [49, 50]. Reasons for this late discovery might be that laser sources, which are powerful enough to generate supercontinuum in a large mode area sapphire fiber, were not available, sapphire fibers were not commercialized until late 1990's, and the application areas of sapphire fibers were mostly on medical laser power delivery [43], high-temperature thermometers [44], and harsh environment sensors [45-48]. To the best of our knowledge, we are the first group to demonstrate supercontinuum generation in sapphire fibers [51-53].

As introductory step, general theories of supercontinuum generation were discussed. First, generalized Schrödinger equation including high-order nonlinear effects was derived to fit into our sapphire fibers. Then, various nonlinear effects including self-phase modulation (SPM), cross-phase modulation (XPM), four-wave mixing (FWM), and

scattered Raman scattering (SRS), which were observable in our experiments, were explained using theories, simulation and experimental results. Also, laser systems including a femtosecond laser system and an OPA in our lab were explained since they were key equipments to realize supercontinuum generation in sapphire fibers.

To check the feasibility of sapphire fibers as optical media to generate supercontinuum, their material and optical characteristics were reviewed. Also, we successfully generated supercontinuum in sapphire fibers by pumping at 784nm, which was the wavelength of our femtosecond laser system. Spectra comparison between sapphire fiber and bulk explained that the smaller effective mode area could enhance the spectrum broadening, which was in good agreement with the theory. Also, spectra comparison between 1cm and 3cm sapphire fibers was performed to explain that longer interaction length could generally enhance the spectrum broadening. These experiments were performed by pumping sapphire fibers at normal dispersion region ($D<0$).

To observe the relationship among fiber, dispersion, and nonlinear lengths, sapphire fibers were pumped at 2μm, which was in anomalous dispersion region. When 5cm sapphire fiber was used for supercontinuum generation, which was longer than nonlinear length but shorter than dispersion length, the nonlinear effect mostly observed was SPM. However, when 35cm sapphire fiber, which was longer than both nonlinear and dispersion lengths, we observed soliton-related dynamics accompanied by SPM. Both results were in good agreements with theories. The spectrum broadening was ranged from 1200nm to 2800nm. We also performed longer wavelength pumping by using 2.5μm, and obtained the spectrum ranged from 2μm to 3.2μm. Since the spectrum beyond 2.5μm was not easily achievable by silica-based fibers, this proved that sapphire fibers were indeed good optical media for supercontinuum generation in mid-IR.

To further enhance the spectrum expansion in sapphire fibers, we simultaneously pumped a sapphire fiber at three different wavelengths, which were 784nm, 1290nm, and 2000nm. As the result, we obtained very wide supercontinuum spectrum ranged from UV to mid-IR. We also observed four-wave mixing (FWM) effects caused by interaction between two pumping sources.

We performed numerical simulations to help understanding the various nonlinear effects observed in sapphire fibers. We utilized the generalized nonlinear schrödinger equation (NLSE) developed for silica fibers to simulate pulse propagation in sapphire fibers, and compared experimental and simulation results to investigate the conformity of theoretical model between silica and sapphire fibers.

To show the usability of our generated supercontinuum, IR absorption spectroscopy of various chemicals using our supercontinuum source was performed. Many chemicals were successfully identified in wide range. Also, to see the possibility of remote sensing using our supercontinuum, far-distance IR absorption spectroscopy of various chemicals was performed. The differentiable peaks for various chemicals are clearly observed.

In previous chapters, we have demonstrated broadband supercontinuum generation in mid-IR region by pumping sapphire fibers at wavelengths of 2μm and 2.5μm. However, generated supercontinuum was pumped in near-IR or the boundary of mid-IR, then expanded into mid-IR region. In this case, we have not truly observed supercontinuum characteristics of sapphire fibers pumped in mid-IR region. Thus, we still need to investigate the feasibility of mid-IR pumping of sapphire fibers. As a future work, we plan to pump sapphire fibers at 3~3.5μm, which may enable supercontinuum to expand beyond 4μm. As described in Chapter 3, the wavelength tunability by the OPA

itself is 1.1μm to 2.6μm. However, an externally installed BBO crystal generating DFG process between signal and idler beams ($\omega_{NEW} = \omega_S - \omega_I$) can enhance the wavelength tuning ability up to 11μm, which is suitable to pump sapphire fibers at mid-IR region.

REFERENCES

1. N. Bloembergen, and P. Lallemand, "Complex intensity-dependant index of refraction, frequency broadening of stimulated Raman lines and stimulated Rayleigh scattering," Phys. Rev. Lett. **16**, 81-86 (1966).

2. R. H. Stolin, and C. Lin, "New nanosecond continuum for excited-state spectroscopy," Appl. Phys. Lett. **28**, 216-218 (1976).

3. G. Lenz, J. Zimmermann, T. Katsufuji, M. E. Lines, H. Y. Hwang, S. Spalter, R. E. Slusher, S. W. Cheong, J. S. Sanghera, and I. D. Agrawal, "Large Kerr effect in bulk Se-based chalcogenide glasses," Opt. Lett. **25**, 254-256 (2000).

4. J. Broeng, S. E. Barkou, A. Bjarklev, J. C. Knight, T. A. Birks, and P. S. Russell, "Highly increased photonic band gaps in silica/air structures," Opt. Commun. **156**, 240-244 (1998).

5. J. Broeng, D. Mogilevstev, S. E. Barkou, and A. Bjarklev, "Photonic crystal fibers: A new class of optical waveguides," Opt. Fiber Technol. **5**, 305-330 (1999).

6. J. C. Knight, T. Birks, P. Russell, and D. M. Atkin, "All-silica single-mode optical fiber with photonic crystal cladding," Opt. Lett. **21**, 1547-1549 (1996).

7. J. C. Knight, J. Broeng, T. A. Birks, and P. S. J. Russell, "Photonic band gap guidance in optical fibers," Science **282**, 1476-1478 (1998).

8. M. A. Newhouse, D. L. Weidman, and D. W. Hall, "Enhanced-nonlinearity single-mode lead silicate optical fiber," Opt. Lett. **15**, 1185-1197 (1990).

9. M. Asobe, T. Kanamori, and K. Kubodera, "Applications of highly nonlinear chalcogenide glass fibers in ultrafast all-optical switches," IEEE J. Quantum Electron. **29**, 2325-2333 (1993).

10. M. Asobe, "Nonlinear optical properties of chalcogenide glass fibers and their application to all-optical switching," Opt. Fiber Technol. **3**, 142-148 (1997).

11. P. Rigby, "Optics – A photonic crystal fibre," Nature **396**, 415-416 (1998).

12. S. E. Barkou, J. Broeng, and A. Bjarklev, "Silica-air photonic crystal fiber design that permits waveguiding by a true photonic bandgap effect," Opt. Lett. **24**, 46-48 (1999).

13. S. Smolorz, I. Kang, F. Wise, B. G. Aitken, and N. F. Borrelli, "Studies of optical non-linearities of chalcogenide and heavy-metal oxide glasses," J. Non-Crystal. Solids **256**, 310-317 (1999).

14. T. Cardinal, K. A. Richardson, H. Shim, A. Schulte, R. Beatty, K. Le Foulgoc, C. Meneghini, J. F. Viens, and A. Villeneuve, "Non-linear optical properties of chalcogenide glasses in the system As–S–Se," J. Non-Crystal. Solids **256**, 353-360 (1999).

15. A. A. Ivanov, M. V. Alfimov, A. B. Fedotov, A. A. Podshivalov, D. Chorvat and A. M. Zheltikov, "An all-solid-state sub-40-fs self-starting Cr4+: Forsterite laser with holey-fiber beam delivery and chirp control for coherence-domain and nonlinear-optical biomedical applications," Laser Phys. **11**, 158-163 (2001).

16. D. M. Gaudiosi, E. Gagnon, A. L. Lytle, J. L. Fiore, E. A. Gibson, S. Kane, J. Squier, M. M. Murnane, H. C. Kapteyn, R. Jimenez, and S. Backus, "Multi-kilohertz repetition rate Ti:sapphire amplifier based on down-chirped pulse amplification," Opt. Express **14**, 9277-9283 (2006).

17. G. Cerullo, and S. D. Silvestri, "Ultrafast optical parametric amplifiers," Rev. Scientific instruments **74**, 1-18 (2003).

18. K. Tamura, E. Ippen, H. Haus, and L. Nelson, "77-fs pulse generation from a stretched pulse mode-locked all-fiber ring laser," Opt. Lett. **18**, 1080-1082 (1993).

19. W. Koechner, *Solid-state laser engineering 5th Ed.* (Springer-Verlag, Berlin Heidelberg New York, 1999).

20. B. Povazay, K. Bizheva, A. Unterhuber, B. Hermann, H. Sattmann, A. Fercher, W. Drexler, A. Apolonski, W. Wadsworth, J. Knight, P. Russell, M. Vetterlein, and E. Scherzer, "Submicrometer axial resolution optical coherence tomography," Opt. Lett. **27**, 1800-1802 (2002).

21. I. Hartl, X. Li, C. Chudoba, R. Ghanta, T. Ko, J. Fujimoto, J. Ranka, and R. Windeler, "Ultrahigh-resolution optical coherence tomography using continuum generation in air-silica microstructure optical fiber," Opt. Lett. **26**, 608-610 (2001).

22. D. Jones, S. Diddams, J. Ranka, A. Stentz, R. Windeler, J. Hall, and S. Cundiff, "Carrier-envelope phase control of femtosecond mode-locked lasers and direct optical frequency synthesis," Science **288**, 635-639 (2000).

23. S. Cundiff, and Jun Ye, "Colloquium: Femtosecond optical frequency combs," Rev. Mod. Phys. **75**, 325-342 (2003).

24. D. J. Cook, and R. M. Hochstrasser, "Intense terahertz pulses by four-wave rectification in air," Opt. Lett. **25**, 1210-1212 (2000).

25. G. H. Welsh, N. T. Hunt, and K. Wynne, "Terahertz-Pulse Emission Through Laser Excitation of Surface Plasmons in a Metal Grating," Phys. Rev. Lett. **98**, 026803 (2007).

26. H. C. Kapteyn, M. M. Murnane, and I. P. Christov, "Extreme nonlinear optics: Coherent X-rays from lasers," Physics Today **March**, 39-44 (2005).

27. H. Takara, T. Ohara, K. Mori, K. Sato, E. Yamada, Y. Inoue, T. Shibata, M. Abe, T. Morioka, and K. Sato, "More than 1000 channel optical frequency chain generation from single supercontinuum source with 12.5 GHz channel spacing," Electron. Lett. **26**, 2089-2090 (2000).

28. T. Morioka, K. Mori and M. Saruwatari, "More than 100-wavelength-channel picosecond optical pulse generation from single laser source using supercontinuum in optical fibres," Electron. Lett. **29**, 862-864 (1993).

29. Y. Takushima, and K. Kikuchi, "10-GHz, over 20-channel multiwavelength source by slicing super-continuum spectrum generated by in normal-dispersion fiber," Photon. Tech. Lett. **11**, 322-324 (1999).

30. S. T. Sanders, "Wavelength-agile fiber laser using group-velocity dispersion of pulsed super-continua and application to broadband absorption spectroscopy," Appl. Phys. B-Lasers Opt. **75**, 799-802 (2002).

31. C. Xia, M. Kumar, M.-Y. Cheng, R. S. Hegde, M. N. Islam, A. Galvanauskas, H. G. Winful, and F. L. Terry, Jr, "Power scalable mid-infrared supercontinuum generation in ZBLAN Fluoride fibers with up to 1.3 watts time-averaged power," Opt. Express **15**, 865-871 (2007).

32. J. H. V. Price, T. M. Monro, H. Ebendorff-Heidepriem, F. Poletti, P. Horak, V. Finazzi, J. Y. Y. Leong, P. Petropoulos, J. C. Flanagan, G. Brambilla, X. Feng, and D. J. Richardson, "Mid-IR supercontinuum generation from nonsilica microstructured optical fibers," IEEE J. Quantum Electron. **13**, 738-749 (2007).

33. I. T. Sorokina, and K. L. Vodopyanov, *Solid-state mid-infrared laser sources* (Springer-Verlag, Berlin Heidelberg, 2003).

34. C. Xia, M. Kumar, O. P. Kulkarni, M. N. Islam, and F. J. Terry, Jr, "Mid-infrared supercontinuum generation to 4.5μm in ZBLAN fluoride fibers by nanosecond diode pumping," Opt. Lett. **31**, 2553-2555 (2006).

35. F. G. Omenetto, N. A. Wolchover, M. R. Wehner, M. Ross, A. Efimov, A. J. Taylor, V. V. R. K. Kumar, A. K. George, J. C. Knight, N. Y. Joly, and P. St. J. Russel, "Spectrally smooth supercontinuum from 530nm to 3μm in sub-centimeter lengths of soft-glass photonic crystal fibers," Opt. Express **14**, 4928-4934 (2006).

36. J. S. Sanghera, I. D. Aggarwal, L. E. Busse, P. C. Pureza, V. Q. Nguyen, and L. B. Shaw, "Chalcogenide optical fibers target mid-IR applications," Laser Focus World **41**, 83 (2005).

37. J.-L. Adam, "Non-oxide glasses and their applications in optics," J. Non-Crystalline Solids **287**, 401-404 (2001).

38. V. V. R. K. Kumar, A. K. George, W. H. Reeves, J. C. Knight, P. St. J. Russel, F. G. Omenetto, and A. J. Taylor, "Extruded soft glass photonic crystal fiber for ultrabroad supercontinuum generation," Opt. Express **10**, 1520-1525 (2002).

39. T. J. Polletto, A. K. Ngo, A. Tchapyjnikov, K. Levin, D. Tran, and N. M. Fried, "Comparison of germanium oxide fibers with silica and sapphire fiber tips for transmission of Erbium: YAG laser radiation," Lasers Surgery Medicine **38**, 787-791 (2006).

40. R. Nubling, and J. Harrington, "Optical properties of single-crystal sapphire fibers," Appl. Opt. **36** (1997).

41. R. K. Nubling, and J. A. Harrington, "Single-crystal laser-heated pedestral-growth sapphire fibers for Er:YAG laser power delivery," Appl. Opt. **37**, 4777-4781 (1998).

42. A. Major, F. Yoshino, I. Nikolakakos, J. S. Aitchison, and P. W. E. Smith, "Dispersion of the nonlinear refractive index in sapphire," Opt. Lett. **29**, 602-604 (2004).

43. R. W. Waynant, S. Oshry, and M. Fink, "Infrared measurements of sapphire fibers for medical applications," Appl. Opt. **32**, 390-392 (1993).

44. Y. Shen, L. Tong, T. Wang, and L. Ye, "Sapphire-fiber thermometer ranging from 20 to 1800 °C," Appl. Opt. **38**, 1139-1143 (1999).

45. Y. Zhu, Z. Huang, F. Shen, and A. Wang, "Sapphire-fiber-based white-light interferometric sensor for high-temperature measurements," Opt. Lett. **30**, 711-713 (2005).

46. Y.-C. Kim, J.-F. Masson, and K. S. Booksh, "Single-crystal sapphire-fiber optic sensors based on surface plasmon resonance spectroscopy for in situ monitoring," Talanta **67**, 908-917 (2005).

47. Z. Huang, G. Pickrell, and A. Wang, "Penetration rate of water in sapphire and silica optical fibers at elevated temperature and pressure," Opt. Eng. **43**, 1272-1273 (2004).

48. C. Zhan, J. H. Kim, S. Yin, P. Ruffin, C. Luo, "High Temperature Sensing Using Higher-Order-Mode Rejected Sapphire Fiber Gratings," Optical Memory and Neural Networks (Information Optics) **16**, 204-210 (2007).

49. J. L. Tate, "Intense laser propagation in sapphire, Ph. D. Thesis," (The Ohio State University, 2004).

50. Wang, L. Qian, H. Luo, P. Yuan, and H. Zhu, "Ultrabroad supercontinuum generation by femtosecond dual-wavelength pumping in sapphire," Optics Express **14**, 6366-6371 (2006).

51. J. H. Kim, M.-K. Chen, C.-E. Yang, J. Lee, S. Yin, P. Ruffin, E. Edwards, C. Brantley and C. Luo, "Broadband IR supercontinuum generation using single crystal sapphire fibers," Opt. Express **16**, 4085-4093 (2008).

52. J. H. Kim, M.-K. Chen, C.-E. Yang, J. Lee, K. Shi, Z. Liu, S. Yin, K. Reichard, P. Ruffin, E. Edwards, C. Brantley, and C. Luo, "Broadband supercontinuum generation covering UV to mid-IR region by using three pumping sources in single crystal sapphire fiber," Opt. Express **16**, 14792-14800 (2008).

53. S. Yin, J. H. Kim, C. Zhan, J. W. An, J. Lee, P. Ruffin, E. Edwards, C. Brantley, and C. Luo, "Supercontinuum generation in single crystal sapphire fibers," Opt. Comm. **281**, 1113-1117 (2008).

54. S. Backus, C. G. Durfee III, M. M. Murnane, and H. C. Kapteyn, "High power ultrafast lasers," Rev. Scientific instruments **69**, 1207-1223 (1998).

55. D. H. Jundt, M. M. Fejer, and R. L. Byer, "Characterization of single-crystal sapphire fibers for optical power delivery systems," Appl. Phys. Lett. **55**, 2170-2172 (1989).

56. G. N. Merberg, and J. A. Harrington, "Optical and mechanical properties of single-crystal sapphire optical fibers," Appl. Opt. **32**, 3201-3209 (1993).

57. R. S. F. Chang, S. Sengupta, G. J. Dixon, L. B. Shaw, and N. Djeu, "Growth of small laser crystals for study of energy kinetics and spectroscopy," SPIE **1104**, 244-240 (1989).

58. R. S. F. Chang, V. Phomsakha, and N. Djeu, "Recent advances in sapphire fibers in Biomedical Optoelectronic Instrumentation," SPIE **2396**, 48-53 (1995).

59. R. S. Feigelson, "Pulling optical fibers," J. Cryst. Growth **79**, 669-680 (1986).

60. http://www.photran.com/photran_pages/main_pages/about.html.

61. G. Agrawal, *Nonlinear Fiber Optics, 2nd Ed.* (Academic Press, New York, 1995).

62. R. W. Boyd, *Nonlinear Optics, 2nd Ed.* (Academic Press, San Diego, 2003).

63. D. Hollenbeck, and C. D. Cantrell, "Multiple-vibrational-mode model for fiber-optic Raman gain spectrum and response function," J. Opt. Soc. Am. B **19**, 2886-2892 (2002).

64. J. Sun, J. P. Longtin, and P. M. Norris, "Ultrafast laser micromachining of silica aerogels," J. Non-Crystalline Solids **281**, 39-47 (2001).

65. L. Ding, R. I. Blackwell, J. F. Künzler, and W. H. Knox, "Femtosecond laser micromachining of waveguides in silicone-based hydrogel polymers," Appl. Opt. **47**, 3100-3108 (2008).

66. S. Nolte, C. Momma, H. Jacobs, A. Tunnermann, B. N. Chichkov, B. Wellegehausen, and H. Welling, "Ablation of metals by ultrafast laser pulses," J. Opt. Soc. Am. B **14**, 2716-2722 (1997).

67. C. Lei, M. Bauer, K. Read, R. Tobey, Y. Liu, T. Popmintchev, M. M. Murnane, and H. C. Kapteyn, "Hot-electron-driven charge transfer processes on O2/Pt(111) surface probed by ultrafast extreme-ultraviolet pulses," Phys. Rev. B **66**, 245420 (2002).

68. Y. D. Jho, K. J. Yee, D. S. Kim, and K.-S. Kim, "Femtosecond frequency mixing in thick bulk GaAs," Phys. Rev. B **63**, 085206 (2001).

69. C. Wang, Y. Fu, Z. Zhou, Y. Cheng, and Z. Xu, "Femtosecond filamentation and supercontinuum generation in silver-nanoparticle-doped water," Appl. Phys. Lett. **90**, 181119 (2007).

70. N. D. Psaila, R. R. Thomson, H. T. Bookey, S. Shen, N. Chiodo, R. Osellame, G. Cerullo, A. Jha, and A. K. Kar, "Supercontinuum generation in an ultrafast laser inscribed chalcogenide glass waveguide," Opt. Express **15**, 15776-15781 (2007).

71. T. Tori, N. Nishizawa, T. Goto, and M. Yoshida, "Experimental and numerical analysis of widely broadened supercontinuum generation in highly nonlinear dispersion-shifted fiber with a femtosecond pulse," J. Opt. Soc. Am. B **21**, 1969-1980 (2004).

72. T. Fujii, N. Goto, M. Miki, T. Nayuki, and K. Nemoto, "Lidar measurement of constituents of microparticles in air by laser-induced breakdown spectroscopy using femtosecond terawatt laser pulses," Opt. Lett. **31**, 3456-3458 (2006).

73. W. C. Swann, and N. R. Newbury, "Frequency-resolved coherent lidar using a femtosecond fiber laser," Opt. Lett. **31**, 826-828 (2006).

74. X. Xie, J. Dai, and X.-C. Zhang, "Coherent Control of THz Wave Generation in Ambient Air," Phys. Rev. Lett. **96**, 075005 (2006).

75. K.-H. Hong, S. Kostritsa, T. J. Yu, J. H. Sung, I. W.. Choi, Y.-C. Noh, D.-K. Ko, and J. Lee, "Development and characterization of 100-kHz high-peak-power femtosecond laser based on downchirped regenerative amplification," J. Korean Phys. Soc. **49**, 424-429 (2006).

76. O. E. Martinez, "3000 times grating compressor with positive group velocity dispersion: Application to fiber compensation in 1.3-1.6μm region " IEEE J. Quantum Electron. **QE-23**, 59-64 (1987).

77. B. Schroder, "Optical parametric amplification from quantum noise," Opt. Quantum Electron. **15**, 57-63 (1983).

78. R. A. Baumgartner, and R. L. Byer, "Optical parametric amplification," IEEE J. Quantum. Electron. **QE-15**, 432-444 (1979).

79. H. Aizawa, N. Ohishi, S. Ogawa, A. Endo, A. Hakamada, T. Katsumata, S. Komuro, T. Morikawa, and E. Toba, "Characteristics of sapphire fiber connected with ruby sensor head for the fiber-optic thermometer applications," Sensors and Actuators A **101**, 42-48 (2002).

80. G. Merberg, and J. Harrington, "Optical and mechanical properties of single-crystal sapphire optical fibers," Appl. Opt. **32**, 3201-3209 (1993).

81. M. Bass, *Handbook of Optics, Vol. II* (McGraw-Hill, Inc., New York, 1995).

82. J. A. Buck, *Fundamentals of Optical Fibers, 2nd ed.* (John Wiley and Sons, Inc., New Jersey, 2004).

83. I. Cristiani, R. Tediosi, L. Tartara, and V. Degiorgio, "Dispersive wave generation by solitons in microstructured optical fibers," Opt. Express **12**, 124-135 (2003).

84. K. J. Blow, and D. Wood, "Theoretical description of transient stimulated Raman scattering in optical fibers," IEEE J. Quantum Electron. **25**, 2665-2673 (1989).

85. A. Z. Grasyuk, S. V. Kurbasov, L. L. Losev, A. P. Lutsenko, A. A. Kaminskii, and V. B. Semenov, "Determination of the Raman gain coefficient in leucosapphire," Quantum Electron. **28**, 162-166 (1998).

86. W. Jia, and W. M. Yen, "Raman scattering from sapphire fibers," J. Raman Spectroscopy **20**, 785-788 (1989).

87. J. K. Ranka, R. S. Windeler, and A. J. Stentz, "Visible continuum generation in air-silica microstructure optical fibers with anomalous dispersion at 800nm," Opt. Lett. **25**, 25-27 (2000).

88. J. M. Dudley, G. Genty, and S. Coen, "Supercontinuum generation in photonic crystal fibers," Rev. Mod. Phys. **78**, 1135-1184 (2006).

89. R. Zhang, J. Teipei, and H. Giessen, "Theoretical design of a liquid-core photonic crystal fiber for supercontinuum generation," Opt. Express **14**, 6800-6812 (2006).

90. B. Saleh, and M. Teich, *Fundamentals of Photonics, 2nd ed.* (Wiley-Interscience, New Jersey, 2007).

91. J. Gopinath, H. Shen, H. Sotobayashi, E. Ippen, T. Hasegawa, T. Nagashima, and N. Sugimoto, "Highly nonlinear bismuth-oxide fiber for smooth supercontinuum generation at 1.5 μm," Opt. Express **12**, 5697-5702 (2004).

92. R. R. Gattass, G. T. Svacha, L. Tong and E. Mazur, "Supercontinuum generation in submicrometer diameter silica fibers," Opt. Express **14**, 9408-9414 (2006).

93. S. Coen, A. Chau, R. Leonhardt, J. Harvey, J. Night, W. Wadsworth, and P. Russell, "White-light supercontinuum generation with 60-ps pump pulses in a photonic crystal fiber," Opt. Lett. **26**, 1356-1358 (2001).

94. J. Herrmann, U. Griebner, N. Zhavoronkov, A. Husakou, D. Nickel, J. C. Knight, W. J. Wadsworth, P. St. J. Russell, and G. Korn, "Experimental evidence for supercontinuum generation by fission of higher-order solitons in photonic fibers," Phys. Rev. Lett. **88**, 173901 (2002).

95. A. V. Husakou, and J. Herrmann, "Supercontinuum generation of higher-order solitons by fission in photonic crystal fibers," Phys. Rev. Lett. **87**, 203901 (2001).

96. D. R. Austin, C. M. de Sterke, B. J. Eggleton, and T. G. Brown, "Dispersive wave blue-shift in supercontinuum generation," Opt. Express **14**, 11997-12007 (2006).

97. G. Genty, M. Lehtonen, and H. Ludvigsen, "Effect of cross-phase modulation on supercontinuum generated in microstructured fibers with sub-30 fs pulses," Opt. Express **12**, 4614-4624 (2004).

98. R. H. Stolen, J. P. Gordon, W. J. Tomlinson, and H. A. Haus, "Raman response function of silica-core fibers," J. Opt. Soc. Am. B **6**, 1159-1166 (1989).

99. P. S. Westbrook, J. W. Nicholson, K. S. Feder, and A. D. Yablon, "Improved supercontinuum generation through UV processing of highly nonlinear fibers," J. Light. Tech. **23**, 13-18 (2005).

100. Redrawn from http://optical-material.optical-components.com/.

101. P. Weibring, H. Edner and S. Svanberg, "Versatile mobile lidar system for environmental monitoring," Appl. Opt. **42**, 3583-3594 (2003).

102. J. Kasparian, R. Sauerbrey, D. Mondelain, S. Niedermeier, J. Yu, J.-P. Wolf, Y.-B. André, M. Franco, B. Prade, S. Tzortzakis, A. Mysyrowicz, M. Rodriguez, H. Wille and L. Wöste,, "Infrared extension of the supercontinuum generated by femtosecond terawatt laser pulses propagating in the atmosphere," Opt. Lett. **25**, 1397-1399 (2000).

103. A. Shirakawa, J. Ota, M. Musha, K. Nakagawa and K. Ueda, "Large-mode-area erbium-ytterbium-doped photonic-crystal fiber amplifier for high-energy femtosecond pulses at 1.55μm," Opt. Express **13**, 1221-1227 (2005).

104. G. Genty, T. Ritari and H. Ludvigsen, "Supercontinuum generation in large mode-area microstructured fibers," Opt. Express **13**, 8625-8633 (2005).

105. T. A. Birks, W. J. Wadsworth and P. St. J. Russell, "Supercontinuum generation in tapered fibers," Opt. Lett. **25**, 1415-1417 (2000).

106. E. E. Serebryannikov, S. O. Konorov, A. A. Ivanov, M. V. Alfimov, M. Scalora and A. M. Zheltikov, "Cross-phase-modulation-induced instability in photonic-crystal fibers," Phys. Rev. E **72**, 027601 (2005).

107. E. Räikkönen, G. Genty, O. Kimmelma, M. Kaivola, K. P. Hansen and S. C. Buchter, "Supercontinuum generation by nanosecond dual-wavelength pumping in microstructured optical fibers," Opt. Express **14**, 7914-7923 (2006).

108. E. Räikkönen, S. C. Buchter and M. Kaivola, "Generation of monochromatic visible light in microstructured optical fiber by nondegenerate four-wave mixing," Appl. Phys. B **91**, 461-465 (2008).

109. G. Genty, M. Lehtonen and H. Ludvigsen, "Route to broadband blue-light generation in microstructured optical fibers," Opt. Lett. **30**, 756-758 (2005).

110. T. Schreiber, T. V. Andersen, D. Schimpf, J. Limbert, and A. Tünnermann, "Supercontinuum generation by femtosecond single and dual wavelength pumping in photonic crystal fibers with two zero dispersion wavelengths," Opt. Express **13**, 9556-9569 (2005).

111. N. K. Das, Y. Yamayoshi and H. Kawaguchi, "Analysis of basic four-wave mixing characteristics in a semiconductor optical amplifier by the finite-difference beam propagation method," IEEE J. Quantum Electron. **36**, 1184-1192 (2000).

112. W. J. Wadsworth, N. Joly, J. C. Knight, T. A. Birks, F. Biancalana and P. St. J. Russell, "Supercontinuum and four-wave mixing with Q-switched pulses in endlessly single-mode photonic crystal fibres," Opt. Express **12**, 299-309 (2004).

113. J. R. Thompson, and R. Roy, "Nonlinear dynamics of multiple four-wave mixing processes in a single-mode fiber," Phys. Rev. A **43**, 4987-4996 (1991).

114. J. Fan, A. Migdall, and L. J. Wang, "Increased cross-correlation in cascaded four-wave mixing processes," Opt. Express **15**, 7146-7151 (2007).

115. V. Tombelaine, P. Leproux, V. Couderc, and A. Barthélémy, "Visible supercontinuum generation in holey fibers by dual-wavelength subnanosecond pumping," IEEE Photon. Technol. Lett. **18**, 2466-2468 (2006).

116. M. G. Allen, "Diode laser absorption sensors for gas-dynamic and combustion flows," Meas. Sci. Technol. **9**, 545-562 (1998).

117. M. G. Allen, E. R. Furlong, and R. K. Hanson, *Tunable diode laser sensing and combustion control* (Taylor & Francis, New York, 2002).

118. P. A. Martin, "Near-infrared diode laser spectroscopy in chemical process and environmental air monitoring," Chem. Soc. Rev. **31**, 201-210 (2002).

119. J. Hult, R. S. Watt, and C. F. Kaminski, "High bandwidth absorption spectroscopy with a dispersed supercontinuum source," Opt. Express **15**, 11385-11395 (2007).

120. E. Hecht, *Optics, 2nd Ed.* (Addison-Wesley Publishing Company, 1990).

APPENDIX

PUBLICATIONS

The Published Journals:

[1] J. H. Kim, M.-K. Chen, C.-E. Yang, J. Lee, K. Shi, Z. Liu, S. Yin, K. Reichard, P. Ruffin, E. Edwards, C. Brantley, and C. Luo, "Broadband supercontinuum generation covering UV to mid-IR region by using three pumping sources in single crystal sapphire fiber," Opt. Express **16**, 14792-14800 (2008).

[2] J. H. Kim, M.-K. Chen, C.-E. Yang, J. Lee, S. Yin, P. Ruffin, E. Edwards, C. Brantley, and C. Luo, "Broadband IR supercontinuum generation using single crystal sapphire fibers," Opt. Express **16**, 4085-4093 (2008).

[3] S. Yin, J. H. Kim, C. Zhan, J. W. An, J. Lee, P. Ruffin, E. Edwards, C. Brantley, and C. Luo, "Supercontinuum generation in single crystal sapphire fibers," Opt. Comm. **281**, 1113-1117 (2008).

[4] C. Zhan, J. H. Kim, S. Yin, P. Ruffin, C. Luo, "High Temperature Sensing Using Higher-Order-Mode Rejected Sapphire Fiber Gratings," Optical Memory and Neural Networks (Information Optics) **16**, 204-210 (2007).

[5] S. Yin, J. H. Kim, F. Wu, P. B. Ruffin, C. Luo, "Ultra-fast speed, low grating lobe optical beam steering using unequally spaced phased array technique," Opt. Comm. **270**, 41-46 (2007).

Conference Proceedings:

[1] J. H. Kim, M.-K. Chen, C.-E. Yang, J. Lee, S. Yin, K. Reichard, P. Ruffin, E. Edwards, C. Brantley, and C. Luo, "Mid-IR supercontinuum generations and applications," Proc. SPIE **7056**, 70560V (2008).

[2] M.-K. Chen, J. H. Kim, C.-E. Yang, S. Yin, Z. Liu, and R. Hui, "THz generation in multiple air plasmas," Proc. SPIE **7056**, 70561A (2008).

[3] S. Yin, J. H. Kim, J. Yao, P. Ruffin, E. Edwards, C. Brantley, and C. Luo, “Recent advances on multiple channel unequally spaced optical phased array for ultrafast LADAR,” Proc. SPIE **7056**, 705619 (2008).

[4] S. Yin, J. H. Kim, C. Zhan, J. W. An, J. Lee, P. Ruffin, E. Edwards, C. Brantley, and C. Luo, “Supercontinuum generation in single crystal sapphire fibers,” Proc. SPIE **6698**, 66980Z (2007).

[5] J. H. Kim, C. Zhan, and S. Yin, “Broadband supercontinuum generation by bridging two separate supercontinua pumped at two different IR wavelengths,” Proc. SPIE **6698**, 66981J (2007).

[6] C. Zhan, J. H. Kim, J. Lee, S. Yin, P. Ruffin, and C. luo, “High temperature sensing using higher-order-mode rejected sapphire-crystal fiber gratings,” Proc. SPIE **6698**, 66980F (2007).

[7] F. Wu, J. H. Kim, P. Li, Z. Liu, K. Reichard, J. Mazurowski, and S. Yin, “Infrared and Terahertz generation by ultrafast laser pulses,” Proc. SPIE **6314**, 63141S (2006).

[8] J. H. Kim, S. Yin, P. B. Ruffin, and C. Luo, “Improvement in beam scanning using optical phase array and fiber multiplexing techniques,” Proc. SPIE **6314**, 63141I (2006).

[9] S. Yin, J. H. Kim, P. B. Ruffin, and C. Luo, “An investigation on fiber optic gyroscopes using microstructured fibers,” Proc. SPIE **6314**, 63141H (2006).

[10] S. Yin, J. H. Kim, F. Wu, P. Ruffin, and C. Luo, “Ultra-fast speed, low grating lobe optical beam steering using unequally spaced phased array technique,” Proc. SPIE **5911**, 591104 (2005).

VITA

Jae Hun Kim

Jae Hun Kim was born in Pusan, Republic of Korea. He received both B. S. and M. S. degrees from Purdue University, West Lafayette, IN. His study area was on VLSI and Circuit Design. After obtaining his M. S. degree, he had worked in Korea Institute of Science and Technology, Seoul, Republic of Korea for 5 years. His main research was 'Optical Logic Gates and Applications.' He was admitted to the Ph. D. program of Electrical Engineering, The Pennsylvania State University, University Park, PA, on Fall 2004. He joined Dr. Yin's research lab, and has been a research assistant for 4 years.